National Library of Canada
Bibliothèque nationale du Canada

Acquisitions and Bibliographic Services Branch
Direction des acquisitions et des services bibliographiques

395 Wellington Street
Ottawa, Ontario
K1A 0N4

395, rue Wellington
Ottawa (Ontario)
K1A 0N4

Your file Votre référence

Our file Notre référence

NOTICE

The quality of this microform is heavily dependent upon the quality of the original thesis submitted for microfilming. Every effort has been made to ensure the highest quality of reproduction possible.

If pages are missing, contact the university which granted the degree.

Some pages may have indistinct print especially if the original pages were typed with a poor typewriter ribbon or if the university sent us an inferior photocopy.

Reproduction in full or in part of this microform is governed by the Canadian Copyright Act, R.S.C. 1970, c. C-30, and subsequent amendments.

AVIS

La qualité de cette microforme dépend grandement de la qualité de la thèse soumise au microfilmage. Nous avons tout fait pour assurer une qualité supérieure de reproduction.

S'il manque des pages, veuillez communiquer avec l'université qui a conféré le grade.

La qualité d'impression de certaines pages peut laisser à désirer, surtout si les pages originales ont été dactylographiées à l'aide d'un ruban usé ou si l'université nous a fait parvenir une photocopie de qualité inférieure.

La reproduction, même partielle, de cette microforme est soumise à la Loi canadienne sur le droit d'auteur, SRC 1970, c. C-30, et ses amendements subséquents.

Canada

University of Alberta

Relaxation of persistent current and the energy barrier $U_{eff}(j)$ close to T_c in granular $Y_1Ba_2Cu_3O_{7-\delta}$ rings

by

©

Isaac Yakoub Isaac

A thesis submitted to the Faculty of Graduate Studies and Research in partial fulfillment of the requirements for the degree of Doctor of Philosophy

Department of Physics

Edmonton, Alberta

Spring 1996

National Library
of Canada

Acquisitions and
Bibliographic Services Branch

395 Wellington Street
Ottawa, Ontario
K1A 0N4

Bibliothèque nationale
du Canada

Direction des acquisitions et
des services bibliographiques

395, rue Wellington
Ottawa (Ontario)
K1A 0N4

Your file - Votre référence

Our file - Notre référence

The author has granted an irrevocable non-exclusive licence allowing the National Library of Canada to reproduce, loan, distribute or sell copies of his/her thesis by any means and in any form or format, making this thesis available to interested persons.

L'auteur a accordé une licence irrévocable et non exclusive permettant à la Bibliothèque nationale du Canada de reproduire, prêter, distribuer ou vendre des copies de sa thèse de quelque manière et sous quelque forme que ce soit pour mettre des exemplaires de cette thèse à la disposition des personnes intéressées.

The author retains ownership of the copyright in his/her thesis. Neither the thesis nor substantial extracts from it may be printed or otherwise reproduced without his/her permission.

L'auteur conserve la propriété du droit d'auteur qui protège sa thèse. Ni la thèse ni des extraits substantiels de celle-ci ne doivent être imprimés ou autrement reproduits sans son autorisation.

ISBN 0-612-10597-0

Canada

University of Alberta

Library Release Form

Name of Author: Isaac Yakoub Isaac

Title of Thesis: Relaxation of persistent current and the energy barrier $U_{eff}(j)$ close to T_c in granular $Y_1Ba_2Cu_3O_{7-\delta}$ rings

Degree: Doctor of Philosophy

Year this Degree Granted: 1996

Permission is hereby granted to the University of Alberta Library to reproduce single copies of this thesis and to lend or sell such copies for private, scholarly, or scientific research purposes only.

The author reserves all other publication and other rights in association with the copyright in the thesis, and except as hereinbefore provided, neither the thesis nor any substantial portion thereof may be printed or otherwise reproduced in any material whatever without the author's prior written permission.

Isaac Yakoub Isaac
604 E Michener Park
Edmonton, Alberta
T6H 5A1
Canada

April 18, 1996

University of Alberta

Faculty of Graduate Studies and Research

The undersigned certify that they have read, and recommended to the Faculty of Graduate Studies and Research for acceptance, a thesis entitled **Relaxation of persistent current and the energy barrier $U_{eff}(j)$ close to T_c in granular $Y_1Ba_2Cu_3O_{7-\delta}$ rings** submitted by **Isaac Yakoub Isaac** in partial fulfillment of the requirements for the degree of Doctor of Philosophy

Dr J Jung (Supervisor)

Dr SB Woods

Dr JP Franck

Dr JR Beamish

Dr J Stephenson

Dr J McMullin

Dr G Crabtree (External Examiner)

Date APRIL 2/96

Of old hast thou laid the foundation of the earth: and the heavens are the work of thy hands. They shall perish, but thou shalt endure: Yea, all of them shall wax old like a garment; as a vesture shalt thou change them, and they shall be changed: But thou art the same, and thy years shall have no end.

Psalm 102: 25-27

KJV

To my parents

who got me started;

to my wife, Lois

who keeps me going;

and two my two sons, Abraam and Andre,

who shall carry the torch one day.

Abstract

Studies of the relaxation of persistent currents and the dependence of the critical current on temperature and magnetic field were performed for granular $Y_1Ba_2Cu_3O_{7-\delta}$. The measurements were done using superconducting rings in a persistent mode and a scanning Hall probe. Abrikosov flux-creep-induced relaxation of the persistent current was investigated close to T_c in ring-shaped grain-aligned c-axis oriented $Y_1Ba_2Cu_3O_{7-\delta}$. The measurements were performed for a wide range of current ($j<j_c$) using zero-field-cooling procedure over a temperature range 78-90 K and a time scale between 30 and 20,000 sec. The results revealed two distinct relaxation regimes: (1) a steady-state logarithmic relaxation of the persistent current from an initial value j_0 and (2) a slow nonsteady nonlogarithmic initial relaxation at low values of j_0 which eventually converges to a long-time steady-state logarithmic relaxation. The logarithmic decay of the persistent current is consistent with the Anderson flux-creep model. The slow nonlogarithmic initial relaxation of the persistent current is due to a transient redistribution of magnetic flux over the sample volume, consistent with a theoretical analysis of nonlinear flux diffusion. The results of the measurements of I_c on temperature (60-90 K) in ceramic rings of $Y_1Ba_2Cu_3O_{7-\delta}$ with randomly oriented grains confirmed the presence of the intergrain superconductor-insulator-superconductor (SIS) tunnel junctions in YBCO and the superconductor-normal-metal-superconductor proximity junctions in YBCO/Ag. Small magnetic

fields (up to 60 G) induced a crossover from Ambegaokar-Baratoff form of $I_c(T)$ to Ginzburg-Landau one close to T_c. Studies of the decay rates of the depinning critical current in ceramic rings revealed that the transport current is controlled by the Josephson flux creep with an energy barrier proportional to the variation of the Josephson coupling energy of the intergrain junctions. It was shown that an increase of the normalized logarithmic decay rates S close to T_c is a characteristic feature of the Josephson flux motion.

Acknowledgement

I would like to express my gratitude to my supervisor, Dr J Jung, for his kindness and insight in guiding me through the jungle of high-T_c superconductivity.

I am indebted to all the members of the examining committee: Dr SB Woods, Dr JP Franck, Dr JR Beamish, Dr J Stephenson, Dr J McMullin and Dr G Crabtree for their invaluable discussion and positive comments.

Finally I would like to extend my thanks to all the individuals who make up the Department of Physics at the University of Alberta. They are a unique group who have made my experience as a graduate student much more than an education in physics; they made graduate work a lot of enjoyment.

Table of Contents

Chapter I

Introduction 1

1.1. General 1

1.2. Flux motion 2

1.2.1. Anderson-Kim model 4

1.2.2. Distribution of the Activation Energies 6

1.2.3. Logarithmic Activation Energy 8

1.2.4. Vortex Glass Model 9

1.2.5. The energy barrier $U_{eff}(j)$ and relaxation processes in high-T_c superconductors 12

1.3. Granularity 17

1.3.1. Ambegaokar-Baratoff model 20

1.3.2. Proximity model 21

1.3.3. The granular discrete model 21

1.3.4. Vortex energy in the discrete model . 23

1.3.5. Vortex pinning in the discrete model . 26

1.3.6. Clem's model 27

1.3.7. Granularity in high-T_c ceramic superconductors 28

1.4. Experimental Requirements 30

Chapter II

Experimental Procedure 34

2.1. Induction of persistent currents 34
2.2. Magnetic measurements of the magnitude of the persistent current 39
2.3. Measurements of the decay of persistent currents 43
2.4. Samples preparations 45

Chapter III

Experimental Results 53
3.1. Experimental results for the grain-aligned YBCO 53
3.2. Experimental results for ceramic YBCO rings . 76
3.2.1. Dependence of I_c on temperature . . . 76
3.2.2. Dependence of I_c on the magnetic field 95
3.2.3. Dissipation of the persistent current 98

Chapter IV

Discussion 109
4.1. Grain-aligned YBCO rings 109
4.1.1. Equations governing flux motion and time decay of the persistent current . . 115
4.1.2. Current dependence of the effective energy barrier 121
4.1.3. Time dependence of the energy barrier 125
4.1.4. Temperature dependence of the persistent current 129

4.1.5. Temperature dependence of the normalized decay rates 133
4.1.6. Non-logarithmic initial decays 136
4.2. Ceramic YBCO rings 139
4.2.1. Classification of the intergrain junctions 140
4.2.2. Dissipation of the persistent current in high-T_c ceramics 155
4.2.3. Origin of pinning in high-T_c ceramics 167

Chapter V

Conclusions 181

Bibliography 188

Appendix A 192

Appendix B 197

List of Tables

Table 1: Dimensions and description of grain aligned YBCO samples. 46

Table 2: Calcining conditions of polycrystalline ceramic rings. 50

Table 3: Sintering conditions of polycrystalline ceramic rings. 51

Table 4: Dimensions and geometry of polycrystalline ceramic rings. 52

Table 5: Zero resistance temperature and its field dependence for group A of YBCO rings. 78

Table 6: Zero resistance temperature and its field dependence for group B YBCO/Ag rings. 79

Table 7: Zero resistance temperature and its field dependence for group C (YBCO/Ag + interfaces) rings. 79

Table 8: Zero resistance temperature and its field dependence for group D rings. 80

Table 9: Classification of the ceramic rings in different groups according to the dissipation phenomena. 98

Table 10: Characteristic parameters for an Abrikosov vortex and for an isolated Josephson vortex. . . . 111

Table 11: Exponent α values and their field dependence for group A of ceramic YBCO rings. 145

Table 12: Exponent α values and their field dependence for group B of ceramic YBCO/Ag rings. 146

Table 13: Exponent α values and their field dependence for group C of ceramic YBCO/Ag rings containing interfaces. 147

Table 14: Exponent α values and their field dependence for group D of ceramic rings. 148

Table 15. Comparison between grain aligned and ceramic YBCO. 187

List of Figures

Fig. 1. Schematic representation of the 2-D discrete model. 25

Fig. 2. Three positions for a vortex center in an array. 28

Fig. 3. Schematic of the ring's geometry used in the studies of the critical currents. 36

Fig. 4. The profiles of the magnetic field measured at 78.5K 37

Fig. 5. Dependence of the magnetic field trapped in the ring's center on the applied field measured at 70.5 and 78.5 K. 38

Fig. 6. The profiles of the magnetic field measured at 78.5 K by a Hall probe above a YBCO/Ag ring cooled below T_c in a field of 20 G. 40

Fig. 7. The profile of the trapped magnetic field measured at 74 K by a Hall probe above the zero field cooled ring of $Pr_{.15}Y_{.85}Ba_2Cu_3O_{7-\delta}$ 43

Fig. 8. The profiles of the axial component of the trapped magnetic field generated at 81 K by the persistent current 55

Fig. 9. The profiles of the axial component of the trapped magnetic field generated at 85 K by the persistent current 56

Fig. 10. The profiles of the shielding field H_s, normalized to the applied magnetic field H_a, which was

generated at 81 K by the diamagnetic shielding currents 57

Fig. 11. The profiles of the shielding field H_s, normalized to the applied magnetic field H_a, which was generated at 85 K by the diamagnetic shielding currents 58

Fig. 12. Dependence of the axial component of the persistent current's self-field on the applied field 59

Fig. 13. Dependence of the shielding field measured above the center, the bulk and the edge of a zero field cooled grain-aligned YBCO ring (No. GAR1), on the applied field 60

Fig. 14. Dependence of the persistent current flowing in the zero field cooled grain-aligned YBCO rings: (a) GAR1 and (b) GAR3 on time over a range between 30 and 20,000 sec at 81 K. 64

Fig. 15. Dependence of the persistent current flowing in the zero field cooled grain-aligned YBCO rings: (a) GAR1 and (b) GAR3 on time over a range between 30 and 20,000 sec at 85 K. 65

Fig. 16. Dependence of the persistent current normalized to an initial value I_0 in the zero field cooled grain-aligned YBCO rings: (a) GAR1 and (b) GAR3 on time over a range of 30 to 20,000 sec at 81 K. . . 66

Fig. 17. Dependence of the persistent current normalized to an initial value I_0 in the zero field cooled

grain-aligned YBCO rings: (a) GAR1 and (b) GAR3 on time over a range of 30 to 20,000 sec at 85 K. . . 67

Fig. 18. The Profiles of the max. trapped field due to the persistent current $I_0 \approx I_c$ in the zero field cooled grain-aligned YBCO ring GAR1 at 81 K measured after 30 sec (open circles) and after 20,000 sec (solid circles). 68

Fig. 19. Relaxation of the persistent current after a flux creep annealing procedure was applied to zero field cooled YBCO grain-aligned rings 69

Fig. 20. Dependence of the persistent current normalized to an initial value I_0 on time over a range of 30 to 20,000 sec measured for various values of I_0 at T=88.5 K in the zero field cooled grain-aligned rings 70

Fig. 21. Dependence of the persistent current on time over a range 30 to 20,000 sec measured from a maximum current I_0^{max} close to I_c for various temperatures close to T_c 71

Fig. 22. Dependence of the same persistent currents as in Fig. 21, normalized to the initial values I_0^{max}. 72

Fig. 23. Dependence of the maximum magnitude of the persistent current I_0^{max} close to I_c on temperature. 73

Fig. 24. Dependence of I_0^{max} close to I_c, in the grain-aligned YBCO ring No. GAR1, on temperature 74

Fig. 25. Dependence of the maximum persistent current on the applied magnetic field 75

Fig. 26. Dependence of the intergrain critical current I_c in the YBCO ceramic ring PCR-A1 on temperature . . 81

Fig. 27. Dependence of the intergrain critical current I_c in the YBCO ceramic ring PCR-A2 on temperature . . 82

Fig. 28. Dependence of the intergrain critical current I_c in the YBCO ceramic ring PCR-A3 on temperature . . 83

Fig. 29. Dependence of the intergrain critical current I_c in the YBCO/Ag(2%wt.) ceramic ring PCR-B1 on temperature 84

Fig. 30. Dependence of the intergrain critical current I_c in the YBCO/Ag(2%wt.) ceramic ring PCR-B2 on temperature 85

Fig. 31. Dependence of the intergrain critical current I_c in the YBCO/Ag(2%wt.) ceramic ring PCR-B3 on temperature 86

Fig. 32. Dependence of the intergrain critical current I_c in the YBCO/Ag(4%wt.) ceramic ring PCR-B4 on temperature 87

Fig. 33. Dependence of the intergrain critical current I_c in the YBCO/Ag(4%wt.) ceramic ring PCR-B5 on temperature 88

Fig. 34. Dependence of the intergrain critical current I_c in the YBCO/Ag(2%wt. with interfaces) ceramic ring PCR-C1 on temperature 89

Fig. 35. Dependence of the intergrain critical current I_c in the YBCO/Ag(2%wt. with interfaces) ceramic ring PCR-C2 on temperature 90

Fig. 36. Dependence of the intergrain critical current I_c in the GBCO ceramic ring PCR-D1 on temperature . . 91

Fig. 37. Dependence of the intergrain critical current I_c in the EBCO ceramic ring PCR-D2 on temperature . . 92

Fig. 38. Dependence of the intergrain critical current I_c in the $(Pr_{0.15}Y_{0.85})Ba_2Cu_3O_{7-\delta}$ ceramic ring PCR-D3 on temperature 93

Fig. 39. Dependence of the intergrain critical current I_c in the $(Pr_{0.20}Y_{0.80})Ba_2Cu_3O_{7-\delta}$ ceramic ring PCR-D4 on temperature 94

Fig. 40. Dependence of the intergrain critical current I_c on magnetic field up to 60 G for the YBCO ceramic ring PCR-A3 96

Fig. 41. Dependence of the intergrain critical current I_c on magnetic field up to 80 G for the YBCO/Ag(2%wt.) ceramic ring PCR-B1 97

Fig. 42. Dependence of the persistent current normalized to an initial value $I_0 \sim I_c$ on time measured in ceramic YBCO/Ag (2%wt.) ring PCR-B2 100

Fig. 43. Dependence of the persistent current decay rates on temperature measured in YBCO ceramic ring PCR-A1 101

Fig. 44. Dependence of the persistent current decay rates on temperature measured in YBCO ceramic ring PCR-A2 102

Fig. 45. Dependence of the persistent current decay rates on temperature measured in YBCO/Ag (2%wt.) ceramic ring PCR-B1 103

Fig. 46. Dependence of the persistent current decay rates on temperature measured in YBCO/Ag (2%wt.) ceramic ring PCR-B2 104

Fig. 47. Dependence of the persistent current decay rates on temperature measured in YBCO/Ag (2%wt.) ceramic ring PCR-B3 105

Fig. 48. Dependence of the persistent current decay rates on temperature measured in GBCO ceramic ring PCR-D1 106

Fig. 49. Dependence of the persistent current decay rates on temperature measured in $(Pr_{.15}Y_{.85})Ba_2Cu_3O_{7-\delta}$ ceramic ring PCR-D3 107

Fig. 50. Dependence of the persistent current decay rates on temperature measured in $(Pr_{.2}Y_{.8})Ba_2Cu_3O_{7-\delta}$ ceramic ring PCR-D4 108

Fig. 51. An isolated Josephson vortex compared schematically in one dimension with an Abrikosov vortex in conventional type-II superconductor 113

Fig. 52. Schematic diagram of the ring geometry showing a magnetic vortex trapped in the ring's bulk . . . 117

Fig. 53. The effective energy barrier U_{eff} calculated as a function of the magnitude of the persistent current 122

Fig. 54. The data of Fig. 53 plotted using an extended scale 123

Fig. 55. Dependence of U_{eff} on the current (a) at 81 K in ring GAR1 and (b) at 85 K in ring GAR3 126

Fig. 56. Dependence of U_{eff} on time at (a) 81 K in ring GAR1 and (b) 85 K in ring GAR3 128

Fig. 57. Dependence of the magnitude of the persistent current on temperature over a range (a) 78-88 K in ring GAR1 and (b) 81-88 K in ring GAR3 130

Fig. 58. The dependence of the factor $(j_c-j)/j_c$ on temperature 132

Fig. 59. Dependence of the normalized logarithmic decay rates on temperature 134

Fig. 60. Dependence of U_0 on temperature 135

Fig. 61. Time constant t_p at T=85 K plotted for various values of the initial current I_0 138

Fig. 62. The dependence of I_c in YBCO ring PCR-A1 on the reduced temperature $1-T/T_c^*$ 141

Fig. 63. The dependence of I_c in YBCO/Ag(4%wt) ring PCR-B5 on the reduced temperature $1-T/T_c^*$ 142

Fig. 64. The dependence of I_c in the YBCO/Ag(2%wt) ring PCR-C1 (containing interfaces) on the reduced temperature $1-T/T_c^*$ 143

Fig. 65. The dependence of I_c in $Pr_{0.2}Y_{0.8}Ba_2Cu_3O_{7-\delta}$ ring PCR-D4 on the reduced temperature $1-T/T_c^*$ 144
Fig. 66. The values of α acquired by all samples in the ZFC case 150
Fig. 67. The values of α acquired by all samples for different fields 151
Fig. 68. Dependence of the intergrain flux creep pinning potential U_0 in YBCO ring PCR-A1 on temperature . 159
Fig. 69. Dependence of the intergrain flux creep pinning potential U_0 in YBCO ring PCR-A2 on temperature . 160
Fig. 70. Dependence of the intergrain flux creep pinning potential U_0 in YBCO/Ag (2%wt) ring PCR-B1 on temperature 161
Fig. 71. Dependence of the intergrain flux creep pinning potential U_0 in YBCO/Ag (2%wt) ring PCR-B2 on temperature 162
Fig. 72. Dependence of the intergrain flux creep pinning potential U_0 in YBCO/Ag (2%wt) ring PCR-B3 on temperature 163
Fig. 73. Dependence of the intergrain flux creep pinning potential U_0 in GBCO ring PCR-D1 on temperature . 164
Fig. 74. Dependence of the intergrain flux creep pinning potential U_0 in $Pr_{0.15}Y_{0.85}Ba_2Cu_3O_{7-\delta}$ ring PCR-D3 on temperature 165
Fig. 75. Dependence of the intergrain flux creep pinning potential U_0 in $Pr_{0.20}Y_{0.80}Ba_2Cu_3O_{7-\delta}$ ring PCR-D4 on temperature 166

Fig. 76. Potential energy along a one dimensional array of Josephson junctions with different coupling strength 169

Fig. 77. Dependence of the normalized pinning potential U_n in YBCO ring PCR-A1 on temperature 171

Fig. 78. Dependence of the normalized pinning potential U_n in YBCO ring PCR-A2 on temperature 172

Fig. 79. Dependence of the normalized pinning potential U_n in YBCO/Ag (2%wt) ring PCR-B1 on temperature . 173

Fig. 80. Dependence of the normalized pinning potential U_n in YBCO/Ag (2%wt) ring PCR-B2 on temperature . 174

Fig. 81. Dependence of the normalized pinning potential U_n in YBCO/Ag (2%wt) ring PCR-B3 on temperature . 175

Fig. 82. Dependence of the normalized pinning potential U_n in GBCO ring PCR-D1 on temperature 176

Fig. 83. Dependence of the normalized pinning potential U_n in $Pr_{0.15}Y_{0.85}Ba_2Cu_3O_{7-\delta}$ ring PCR-D3 on temperature 177

Fig. 84. Dependence of the normalized pinning potential U_n in $Pr_{0.20}Y_{0.80}Ba_2Cu_3O_{7-\delta}$ ring PCR-D4 on temperature 178

Fig. 85. Dependence of the normalized decay rate S on temperature obtained from the measurements on YBCO compounds 180

Fig. 86. A schematic model of the pinning potential in the presence (upper) and absence (lower) of field gradient (or current) 193

Fig. 87. Schematic representation of the different components of the experimental set-up 198

Chapter I

Introduction

1.1 General:

The utilization of high temperature superconductors in scientific, medical and commercial applications has been challenged by phenomena of rapid decay of the transport current and the magnetization in these materials. High operating temperatures (large thermal fluctuations) combined with the small flux-pinning energy-barrier in these materials are believed to be responsible for the rapid flux motion. Flux motion induces dissipation of the transport current and reduces the effective critical current density in the presence of magnetic field. Another fact which adds to the complexity of the problem is granularity of high temperature superconductors. Granularity creates a situation in which weak links are formed at the grain boundaries and at other interfaces within the grains themselves (such as twin boundaries), which limits the maximum current density carried by the sample. Single crystals and epitaxial thin films were used to reduce the effects of grain boundaries and weak links but bulk samples are still required for applications which need high currents. Solid state reaction methods produce polycrystalline, randomly oriented high T_c materials with inhomogeneous grain boundaries. Major progress has been achieved using the Melt Powder Melt Growth (MPMG) technique which produces grain aligned bulk samples with c-axis oriented grains and low angle grain

boundaries in which grain boundaries do not act as weak links. From this perspective, one could say that the performance of high temperature superconductors is affected by two major issues: 1) flux pinning and motion and 2) granularity and weak links.

1.2 Flux motion:

When a superconductor is subjected to an external magnetic field $H<H_{c1}$ at temperatures below T_c, flux lines are prevented from entering the sample. However, the field is allowed to penetrate up to a distance determined by the London penetration depth λ. The first flux penetration may occur at fields less than H_{c1} due to non-zero demagnetization factors. Geometry dependent demagnetization effects cause the magnetic field at the surface of the superconductor to acquire values higher than H_a , where H_a is the applied magnetic field measured far away from the sample. Consequently, penetration of vortices occurs close to the surface at applied fields less than H_{c1}. A vortex line near the surface of a superconductor was considered by deGennes[1] who showed that such a vortex interacts with its mirror image in free space, resulting in an attractive force which tends to push the vortex line outside the sample. Bean and Livingston[2] revealed that this interaction produces an energy barrier impeding penetration of the vortex into the volume of the superconductor. This barrier arises from the competition between the Lorentz force produced by shielding currents, which repel the vortex line from the

surface pushing it into the sample, and the attractive image force. The Lorentz force increases with an increasing applied magnetic field and eventually it overcomes the attractive force. Consequently, flux lines then penetrate further into the bulk of the sample.

Once the vortices are inside the sample, in the absence of pinning, the interaction between fluxons carried by each vortex results in a triangular rigid flux lattice. The transport current exerts a transverse Lorentz force on the lattice which responds by establishing a magnetic flux gradient, equivalent to a current flowing in the opposite direction, which exerts the counter-balance Lorentz force. However, there is a maximum critical flux gradient above which flux flow occurs. This flux gradient defines the critical current density of the superconductor. According to Ampere's law, curl$\mathbf{B}=\mu_0\mathbf{j_c}$. In the case of cylindrical geometry $j_c = (1/\mu_0)(\partial B_r/\partial z - \partial B_z/\partial r)$, where B_z and B_r are the axial and radial magnetic inductions respectively. The ratio of the terms $\partial B_r/\partial z$ and $\partial B_z/\partial r$ is approximately equal to the ratio of the radius r_0 of the cylinder to its length d. For a long cylinder, $d>>r_0$ and $j_c\approx-(1/\mu_0)\partial B_z/\partial r$. For a thin disk $r_0>>d$ and $j_c\approx(1/\mu_0)\partial B_r/\partial z$. In the presence of pinning, a pinning force acts on the flux lattice and reduces the effect of the Lorentz force. As long as the pinning force is larger than the Lorentz force, the flux lines are held in place but still have vibrational degree of freedom activated by the thermal energy

with a finite probability for the flux lines to hop forward and backward between adjacent pinning potential wells. This means that the critical current density will be enhanced by the ability of crystal defects to pin down the magnetic flux lines. Many models have been developed to explain flux pinning and creep processes and consequently dissipation of the current when the flux lines start to move out of their pinning positions. Some of these models are reviewed below including their basic assumptions and equations.

1.2.1 Anderson-Kim model:

The concept of flux creep was introduced by Anderson and Kim[3] in order to describe the change of the magnetic moment with time in tubular superconducting samples. This simple model assumes that:

(a) Flux creep is described as the motion of bundles of flux lines jumping between adjacent pinning sites.

(b) Flux lines within each bundle don't interact and the bundles don't interact with each other.

(c) A single pinning energy of potential depth U_0 is available throughout the superconductor. This potential is proportional to the current density j according to the equation

$$U(j) = U_0\left(1 - \frac{j}{j_c}\right) \qquad (1)$$

where j_c is the critical current density.

(d) $U_0/kT > 1$, where kT is the thermal energy.

The Anderson-Kim model gives a logarithmic dependence of the current density j on time, due to flux creep according to the equation

$$j(t)=j(0)\left(1-\frac{kT}{U_0}\ln\left(1+\frac{t}{\tau}\right)\right) \qquad (2)$$

where τ is a characteristic time related to the hopping frequency of flux lines between pinning sites. A brief derivation of Equation 2 is given in Appendix A.

Two arguments were suggested against application of this model to high temperature superconductors:

1) The logarithmic dependence of the magnetic moment on time was derived explicitly for an energy barrier $U_0 \gg kT$ where $U_0=U_0(T,H,j=0)$ is the temperature and magnetic field dependent energy barrier at zero current. Due to high operating temperatures this approximation may not be valid in the case of high temperature superconductors where small U_0/kT ratios result in rapid relaxation of supercurrent[4].

2) The linear dependence of the effective energy on the current $U(j)=U_0(1-j/j_c)$, where j_c is the temperature and magnetic field dependent critical current density, may not be valid since the Lorentz force tends to distort the flux line potential well, which results in a current dependent pinning potential range[5,6].

The above arguments were partially based on the experimental results obtained for the relaxation of the magnetization and for the current dependence of the resistive transition in high

temperature superconductors. This includes a nonlogarithmic decay of magnetic moment observed in $Y_1Ba_2Cu_3O_{7-\delta}$ (YBCO) single crystals[7] and grain aligned samples[8,9] and a nonlinear dependence of the energy barrier for flux creep on current density j, derived from the resistive transition data for YBCO thin films[6].

In the Anderson-Kim model, the spatial dependence of the pinning energy, U(x), has a triangular shape. As a further development of the same model, more realistic shapes of U(x) have been considered[5,10,11], whose dependence on the current density j can be written as

$$U(j) = U_0\left(1-\frac{j}{j_c}\right)^n \qquad (3)$$

where n = 1.5 - 2 is related to the curvature of the pinning potential. For example, a sinusoidal potential

$$U(x) \propto \left(1+\cos\frac{\pi x}{x_0}\right) \qquad (4)$$

where the minimum of the potential well is at $x=x_0$, has a dependence on the current in the form $U(j)=U_0(1-j/j_c)^{3/2}$.

1.2.2 Distribution of the Activation Energies:

In real materials, the defect characteristics have a random nature and thus a realistic extension of the Anderson-Kim model is to introduce a distribution of activation energies, p(U(j))[12,13]. However ,it should be noted here that the flux creep is actually governed by the distribution of occupied energy wells. Since the flux creep rate is higher

for low energies, the steady state distribution q(U(j)) of occupied wells will be shifted towards higher energies with respect to the distribution of available wells. The following assumptions have been made:

(a) All the pinning energies in the distribution have identical current dependence given by Equation 3.

(b) The number of occupied wells is much smaller than the number of available wells. Hence, almost the full pinning energy spectrum p(U(j)) is available for each thermally activated flux jump.

(c) The current density is uniform.

Many choices have been available for the distribution $p(U_0)$ which satisfies the three assumption mentioned above. For example, if the distribution $p(U_0)$ is given by

$$p(U_0) = \delta(U_0 - U_{A\text{-}K}) \qquad (5)$$

the result is the Anderson-Kim model with $U_{A\text{-}K}$ playing the role of U_0 in Equation 1. Another possibility is the existence of both weak and strong pinning sites with energies U_w and U_s. This is described by the distribution

$$p_2(U_0) = 0.5\delta(U_0 - U_w) + 0.5\delta(U_0 - U_s) \qquad (6)$$

Hagen *et al*[14] used an inversion scheme to obtain a log-normal distribution of pinning energies. They used this distribution to explain the relaxation data obtained by others for polycrystalline and single crystals of YBCO at low temperatures. In their model the distribution is given by

$$p(U) = p_m \exp\left[-\gamma \left(\ln \frac{U}{U_m}\right)^2\right] \qquad (7)$$

where U_m is the energy corresponding to the maximum value of $p(U)$ and $p_m = p(U_m)$ and γ is a constant.

Neil *et al*[13] assumed a Gaussian-like distribution of pinning energies with a mean U_m and a standard deviation σ in order to fit relaxation data obtained for the grain aligned YBCO. In this model the effective pinning energy U(j) is given by

$$U(j) = U_m\left(1 - \frac{j}{j_c}\right)^n + \frac{1}{2kT}\left(\sigma^2\left(1 - \frac{j}{j_c}\right)^{2n}\right) \qquad (8)$$

1.2.3 Logarithmic Activation Energy:

A phenomonological form of the activation energy U(j) has been suggested by Zeldov *et al*[6] in order to explain the j-E data close to the irreversibility line in YBCO thin films. U(j) is given by

$$U(j) = U_0 \ln\left(\frac{j_c}{j}\right) \qquad (9)$$

The decay rate of the current, dj/dt, in this model depends on the current density, j, as a power law

$$\frac{dj}{dt} \propto \rho_0 j_c^{\frac{-U_0}{kT}} (j)^{\frac{U_0}{kT}+1} \qquad (10)$$

where ρ_0 is the normal state resistivity.

Zeldov *et al*[6] argued that the physical origin of such a model might be a single defect which destroys the order

parameter in a small volume with a radius which is comparable to the coherence length ξ. In this case a single vortex will be in its lowest energy state at the defect location (or in other words the vortex will be isolated). The magnetic field of an isolated vortex decreases logarithmically with distance, so the energy of the vortex is expected to increase logarithmically with the distance from the defect. A logarithmic U(x) leads to a logarithmic U(j) as described by Equation 9. For the logarithmic activation energy model, the current density decays with time according to a power law

$$j(t) = j_c \left(\frac{\tau_i + t}{\tau}\right)^{\frac{-kT}{U_0}} \qquad (11)$$

where τ is a characteristic time related to the attempt hop frequency and τ_i is the time at which steady state relaxation starts[4] (possibly the duration of the initial non-steady-state relaxation).

1.2.4 Vortex Glass Model:

The theory of vortex glass[15,16] and the theory of collective flux creep[17] give a different model which takes into account the interaction between flux lines during their collective motion.

Larkin[18] argued that material imperfections destroy the crystalline long-range order of the Abrikosov vortex lattice. This process involves two competing effects:

(1) the interaction between the vortex lines which favors a lattice structure, and

(2) randomly located material defects tend to pin the lines at random positions, disrupting the lattice structure.

Beyond a characteristic correlation length scale, l_L, the random vortex pinning dominates and destroys the vortex lattice phase. Although the size of l_L of the micro-crystalline regions can be very long for weak pinning, the long range lattice positional correlations are destroyed for distance in excess of l_L. The Anderson-Kim model maintains that finite bundles of vortex line segments of length and diameter of the order of l_L can move by thermal activation across the free energy barriers caused by the defects. In this approach the interactions between the vortex bundles are ignored. However, according to the vortex glass theory, during cooling, the fluid of the vortex lines interacting with the random pinning sites undergoes a sharp thermodynamic phase transition into the superconduntingphase with no mobile vortices and thus strictly zero resistivity. In this superconducting phase, the vortices are frozen into a configuration determined by the competition between the interaction of the vortices with each other and with the microscopic impurities in the material. Because the vortices are immobile, the phase of the pair wavefunction has a long range order but a random pattern which reflects the specific positions of the frozen vortices. This phase order is analogous to the magnetic order that occurs in random magnetic alloys called spin glasses in which the spin axes of the electrons are frozen in time, but rather than

being aligned as in a ferromagnet, or in a spatially periodic pattern as in an antiferromagnet, they are oriented in a sample specific arrangement, determined by the microscopic structure of the material. Vortex glass theory predicts that the current passing through the superconductor would decay according to $dj/dt \propto \exp\{(-j/j_c)^{-\mu}\}$, where $0<\mu<1$. The theory of collective creep gives more quantitative predictions in the weak pinning case for the parameters μ and j_c which determine the response of vortices in the vortex glass phase. The theory explores the concept of the Anderson's vortex bundle in a vortex lattice pinned collectively by densely disturbed weak point pinning centers. It is found that the vortex bundle size, V_B, and the hopping distance, u_{hop}, of the vortex lattice bundles increase as a power law with increasing j and the energy barrier, U(j), can be written as

$$U(j) = U_0 \left(\frac{j_c}{j}\right)^{\mu} \qquad (12)$$

However, the exponent μ, the energy U_0 and the initial current density j_c depend on the dimensionality of the thermally activated vortex bundles. This is determined by considering the two factors: the forces that the randomly distributed pinning centers exert on the vortices and the elastic interaction between the vortices. Expected values for μ are: $\mu=1/7$ for single vortex hopping, $\mu=3/2$ for small vortex bundles hopping where the dispersion of the elastic moduli of the vortex lattice is relevant and $\mu=7/9$ for large bundles

hopping. These regions also depend on the current range, j, used in the experiment. Hopping of single vortices is associated with currents j close to j_c, hopping of small bundles is associated with intermediate currents and large bundles hopping is associated with small currents. Feigel'man *et al*[17] showed that in order to define the critical current density j_c for which U(j)=0, Equation 12 should be modified to the form

$$U(j)=U_0((\frac{j_c}{j})^{\mu}-1) \qquad (13)$$

which leads to the same results. This kind of pinning potential would result in a dissipation of the current according to the equation

$$j(t)=j_c(1+\frac{kT}{U_0}\ln(\frac{\tau_i+\tau}{\tau}))^{\frac{-1}{\mu}} \qquad (14)$$

where τ_i and τ are characteristic times which depend on both U_0 and T.

1.2.5 The energy barrier $U_{eff}(j)$ and relaxation processes in high-T_c superconductors:

Very systematic measurements of the current dependence of flux creep activation barrier at low temperatures have been performed by Maley *et al*[8], Kung *et al*[19,20] and by Thompson *et al*[21]. Maley *et al*[8] extracted the current dependence of U_{eff} from Beasley-Labusch-Webb equation for thermally activated motion of flux[5]. The relaxation rate of the magnetization *M* according to this model is

$$\frac{dM}{dt} = \frac{Ba\omega_0}{\pi d} \exp\left(-\frac{U_{eff}(j)}{kT}\right) \qquad (15)$$

where B is the local magnetic induction, ω_0 is the characteristic attempt frequency, a is the hopping distance, and d was taken as the average grain diameter for powdered grain aligned samples. This equation allows one to obtain $U_{eff}(j)$ in the form

$$U_{eff}(j) = -kT\ln\left|\frac{dM}{dt}\right| + kT\ln(B\omega_0 a/\pi d) = -kT\left(\ln\left|\frac{dM}{dT}\right| - C\right) \qquad (16)$$

where $C = \ln(B\omega_0 a/\pi d)$. Here it was assumed that $M \propto jd$. Magnetic relaxation measurements were used to find dM/dt as a function of the current density j. This was achieved by recording the decay of magnetization from its critical value $M=j_c d$ for various temperatures between 10 and 30 K in a magnetic field of 1 T. Changing a temperature value ensured in this case a continuous change in j_c, and allowed the measurement of $U_{eff}(j)$ for a wide range of the current. It should be emphasized here that instead of measuring U_{eff} on the current density j over a wide range $0<j\leq j_c$ at fixed temperature, the dependence of U_{eff} on j was measured over a narrow range of j close to j_c for a wide temperature range. As a result a curve of $U_{eff}(j)$ was produced, which consists of multiple segments whose slopes increase with increasing temperature. Each curve segment is measured at a different temperature T for current density j close to $j_c(T)$. Selection of the constant C in Equation (16) multiplied by T for each temperature causes all

of the data to fall on the same smooth $U_{eff}(j)$ curve. This method applied to powdered grain aligned YBCO samples[8] shows a logarithmic-like dependence of U_{eff} on j. U_{eff} diverges in the limit of small currents and approaches zero asymptotically in the limit of large currents.

Kung *et al*[19,20] extended the application of the method of Maley to grain aligned, melt-textured YBCO superconductors over a temperature range between 5 and 80 K. However in this case a single value of C did not result in a smooth $U_{eff}(j)$ curve over a wide range of temperature, especially for high temperature data. This problem was solved by introducing a temperature scaling function $G(T)=(1-T/T_x)^2$ where T_x is a characteristic temperature taken from the magnetic irreversibility line. G(T) was chosen in order to account for the explicit temperature dependence of U_{eff}, which is, in fact, a consequence of the experimental technique adopted in these studies. The above procedure produced a continuous curve of $U_{eff}/G(T)$ vs j. The values of $U_{eff}/G(T)$ diverge in the low current region. The function $\ln(U_{eff}/G)$ is proportional to $\ln(j)$ over a wide temperature range. Kung *et al*[19] made an attempt to rationalize this behavior by considering the result of collective flux creep theory[17] which states that the activation barrier $U_{eff}(j)$ should grow with decreasing current according to a power law described in Equation 13, where the exponent μ depends on the particular regime of flux creep. The data of Kung *et al*. show a similarity to the theoretical

predictions with the low current density regime characterized by a small slope with μ=7/9 (large flux bundle creep regime) for a temperature range 30-50 K and the high current density regime characterized by higher slope with μ=3/2 (small flux bundle creep regime) for a temperature range 5-10 K. It should be pointed out here that the low and high current regimes were achieved by performing the relaxation measurements at high and low temperatures, respectively. The diverging behavior of U_{eff} at low currents (high temperatures) was interpreted as due to a vortex-glass state. Thompson *et al.*[21] applied Maley's method[8] in order to measure the dependance of U_{eff} on current density j in single crystals of YBCO over a temperature range 5-60 K in a magnetic field of 1 T. They indicated that the low temperature data (high current regime) are consistent with the collective flux creep theory with μ=3/2 for a temperature range 5-30 K.

The above experiments utilized the measurement of the relaxation of the magnetization in order to derive $U_{eff}(j)$. Conversion of magnetization M to current density j was achieved by taking M proportional to j in agreement with the Bean's critical state model[22]. It was assumed that the current density j is the same everywhere in the sample and this condition persists not only at $j \approx j_c$ but also when the current density relaxes down to a value $j < j_c$. Schnack *et al.*[23] pointed out that this procedure may not be always correct for high temperature superconductors, since the

inhomogeneous vortex distribution across a superconductor results in a nonuniform magnetization current j. Variation of the current density j during the measurements of U_{eff} vs j, in Maley's method (Ref. 8 and 19-21) was accomplished by changing the sample's temperature. Magnetization relaxations were measured from an initial value of j_0 close to $j_c(T)$, and gave activation energy U_{eff} as a function of $j_0(T)$. It means that for the whole range of current density in the sample, the current is always close to the critical current value. Collective flux creep theory, if applicable in this case, should give $U_{eff}(j)=U_0(j_c/j)^{\mu}$ with μ=1/7 or 3/2 only, excluding a value of 7/9 which was suggested by Kung *et al*[19,20].

Zeldov *et al*.[6] claimed the logarithmic dependence of U_{eff} on the current density by attributing the resistive transition in YBCO superconductors in the presence of magnetic fields to flux creep. They assumed that the resistive transition consists of two regimes: the flux flow regime which dominates at high temperatures and the thermally activated flux creep regime which dominates at lower temperatures. The problem is that near the critical temperature T_c different processes may dominate. The dissipation observed at the superconducting transition was explained quantitatively by Martin *et al*.[24] as due to vortex-antivortex pair excitations. On the other hand, the behavior of the activation energy U_{eff} for low currents reported by Zeldov *et al*.[6], has not been fully proven due to the incomplete measurements of the resistivity ρ on

temperature T for small current density (see Fig. 1(a) in Reference 6).

Although a diversity of models has been proposed and analyzed to describe flux pinning and motion in high temperature superconductors, some questions remain unsolved. The first question is which type of vortices (Abrikosov or Josephson) is responsible for dissipating the current and what are the conditions which make one type of vortices more favorable than the other in a particular material. The second question concerns the nature of the process of current relaxation process measured for waiting times up to 100,000 sec. It is very important to separate non-steady-state transient regimes which occur at the beginning of the relaxation process from the steady state behavior that dominates at longer times. Associated with this is the question: which models should be used to describe the current relaxation in a steady-state and initial non-steady-state regimes? In order to analyze U(j), one needs to study the difference between relaxation of currents with magnitudes less than the critical current ($j<j_c$) and those of values close to j_c ($j\sim j_c$).

1.3 Granularity:

The second problem that seems unavoidable when dealing with high temperature superconductors is the problem of granularity and weak links. One of the main characteristic of such materials is that the BCS[25] coherence length is very short and is comparable to the dimensions of the unit cell.

This creates an unusual sensitivity of the transport properties to structural imperfections. The known imperfections in YBCO single crystal and epitaxial thin films are twin boundaries (which separate microcrystals with crystal axes rotated to interchange the "a" and "b" axes of the orthorhombic structure) and spatial variation in local stoichiometry or oxygen contents. In the ceramic bulk YBCO samples, there is an obvious granularity on a length scale of the order of microns. Granularity is expected to strongly affect the transport and magnetic properties of these samples. It is believed that the grains of good stoichiometric crystalline material are separated by off-stoichiometric material which at lower temperature may be either superconducting with lower T_c or nonsuperconducting (metallic, semiconducting or insulating). The presence of these two different phases in granular superconductors results in two separate sets of physical parameters required to describe them: one set is associated with the grains (e.g. intragrain transition temperature, T_{cg}, intragrain critical current, I_{cg}, intragrain penetration depth, λ_g, intragrain coherence length, ξ_g,...etc) and the other is associated with the junctions, i.e. weak links (e.g. junction intergrain transition temperature, T_{cj}, junction intergrain critical current, I_{cj}, junction intergrain penetration depth, λ_j, junction intergrain coherence length, ξ_j,...etc). A direct consequence of this is the two stage superconducting transition which means that upon cooling the

resistance is first partially lost at T_{cg} when the grains become superconducting and then completely lost at T_{cj} when the phases of the order parameter in adjacent grains lock themselves together to give long range phase coherence. This model has been considered theoretically by many researchers. For instance, Clem *et al*[26] analyzed the model using a dimensionless quantity ϵ which is the ratio of the Josephson coupling energy E_j to the condensation energy E_c of the grain. They incorporated the Josephson's coupling model[27] into a Ginzburg Landau theory[28] of granular superconductors. This approach yielded an expression for the critical current density j_c that has the Ambegaokar-Baratoff[29] temperature dependance characteristic of Josephson (SIS) tunneling at low temperatures

$$I_{cj}(T) = \frac{\pi}{2e}\frac{\Delta(T)}{R_N}\tanh\left(\frac{\Delta(T)}{2kT}\right) \qquad (17)$$

and the Ginzburg-Landau[30] temperature dependance near T_c

$$I_{cj}(T) = const\,(T_c - T)^{3/2} \qquad (18)$$

Tinkham *et al.*[31] argued that the intergranular coupling is better modeled as an S-N-S type weak link than as a (SIS) tunnel junction directly connecting two bits of an ideal material because the short coherence length allows a continuous depression of the superconducting order parameter near the interface. Vortex energy[32] and vortex pinning[33] in a granular superconductor have been analyzed by the Tinkham discrete model[31], which considers thermally activated flux motion in

terms of a characteristic Josephson pinning energy (barrier or activation energy "U") resulting from the spatial variation of the coupling energy. In the following, a brief review of these models is given.

1.3.1 Ambegaokar-Baratoff model:

This model reproduces and generalizes Josephson's[34] calculations for the dc supercurrent flowing through an SIS junction using Green's functions. In the general case, when the energy gaps in the two superconductors are not the same, the maximum Josephson current that can flow through the junction is given by

$$I_{cJ}=\frac{1}{R_n}\Delta_1(T)\mathbf{K}\sqrt{\frac{1-\Delta_1(T)^2}{\Delta_2(T)^2}} \qquad (19)$$

where R_n is the junction normal resistance, $\Delta_1(T)$ and $\Delta_2(T)$ are the energy gaps in the two superconductors, $\Delta_1(T)<\Delta_2(T)$ and K is the complete elliptic integral of the first kind. When the two superconductors are identical, $\Delta_1(T) = \Delta_2(T)$ and Equation 19 transforms to Equation 17. For temperature close to T_c, $\Delta(T)$ is much smaller than kT, the tanh function could be approximated by its argument and the critical current becomes

$$I_{cJ}=\frac{\pi}{2eR_n}\frac{\Delta(T)^2}{2kT_c} \qquad (20)$$

If the BCS dependence of $\Delta(T)$ on the temperature is used, the asymptotic behavior of $I_{cJ}(T)$ near T_c becomes

which means that the critical current is proportional to the

$$I_{cJ} \propto (1-\frac{T}{T_c}) \qquad (21)$$

temperature close to T_c.

1.3.2. Proximity model:

If the insulating material in the junction barrier is replaced by a normal metallic layer, Cooper pairs can diffuse from one superconductor to the other, assuming that the barrier thickness does not exceed 1000 Å. DeGennes[35] showed that the current through the junction due to the diffusion process is given by

$$I_{cJ}=C(T-T_c)^2 \exp\left(\frac{-2d_N}{\xi_N(T)}\right) \qquad (22)$$

where C is a constant, $2d_N$ is the barrier width and $\xi_N(T) \propto T^{-1/2}$ represents the penetration distance of Cooper pairs into the normal metal. Close to T_c this formula can be replaced by a simple expression

$$I_{cJ}=constant(T_c-T)^2 \qquad (23)$$

which gives a quadratic temperature dependence of $I_{cJ}(T)$ close to T_c.

1.3.3. The granular discrete model:

Tinkham *et al*[31] adopted a highly simplified model of grains of ideal crystalline superconductor connected in a three dimensional cubic array by weak links, each having critical current I_c. The lattice spacing of the array is "a", the grain volume is V_g and the macroscopic critical current

density is given by

$$j_{cJ}=\frac{I_c}{a^2} \tag{24}$$

The two parameters j_{cJ} and "a" will characterize the model, i.e. all the other parameters will be expressed in terms of j_{cJ} and "a". A semiquantitative approach was used by the authors to discuss the effects of granularity on the properties of high temperature superconductors. It was found that the three dimensional array of junctions will screen magnetic fields below H_{cJ1} exponentially up to a distance λ_J where λ_J, the effective penetration depth is given by

$$\lambda_J=\left(\frac{c\phi_0}{8\pi^2 a j_{cJ}}\right)^{1/2} \tag{25}$$

In order to define H_{c1J}, the lower critical field, one has to describe a coherence length ξ_J (in the same way as the Ginzburg-Landau ξ). In the discrete model, ξ_J was obtained using the GL definition (Equation 4-37 in Ref. 28) of the maximum phase gradient equal to $1/\sqrt{3}\xi$. Since in the granular discrete model the maximum phase gradient at j_{cJ} is $\pi/2a$, which corresponds to a 2π phase change in the phase of the wavefunction going around an isolated vortex, then

$$\xi_J=\frac{2a}{\sqrt{3}\pi}\sim 0.4a \tag{26}$$

Having λ_J and ξ_J defined, one can define a GL parameter κ_J where

Then H_{c1J} could be defined by substituting λ_J and ξ_J for λ and

$$\kappa_J = \frac{\lambda_J}{\xi_J} = \left(\frac{3\phi_0 c}{32 j_{cJ} a^3}\right)^{\frac{1}{2}} \qquad (27)$$

ξ in the GL expression for H_{c1}. This gives

$$H_{c1J} = \frac{2\pi a j_{cJ}}{c} \ln\left(\frac{\lambda_J}{\xi_J}\right) \qquad (28)$$

The physical significance of H_{c1J} is that it sets the limit for the strength of external magnetic fields that are screened exponentially over a distance λ_J by reversible surface currents. It is also possible to define an upper critical field H_{c2J} using the analogy between the discrete model and the GL model

$$H_{c2J} = \frac{3\pi\phi_0}{8a^2} \qquad (29)$$

It should be noted here that for the granular model H_{c2J} is temperature independent and is determined completely by the grain size "a". It should also be noted that apart from the numerical factor of $3\pi/8$, H_{c2J} is the field at which one flux quantum fits into each unit cell of area a^2.

1.3.4 Vortex energy in the discrete model:

In order to obtain the energy of a vortex in a granular superconductor, Tinkham *et al*[32] studied a two dimensional regular square lattice formed of 2000Å thick $PbBi_{0.05}$ squares on a 1500Å thick Cu film. This is the special case of the three dimensional granular discrete model. For an isolated vortex in zero field, the energy increase due to the vortex is

given by

$$E=E_J \sum_{p=1,3,5,..}^{p_{max}} 4p(1-\cos\gamma_p) \qquad (30)$$

where the index p runs over concentric pxp contours (p=1,3,5...) surrounding the square which contains the vortex center (Fig. 1), E_J is the Josephson coupling energy, and γ_p is the phase difference associated with each link. Since the sum of the phase differences around any contour enclosing the vortex should be 2π, by symmetry one can see that $\gamma_p=2\pi/4p$. Using the small angle approximation for the cosine term and summing over the proper p index, Equation 30 becomes

$$E=\frac{\pi^2}{4}E_J \ln(p_{max}) \qquad (31)$$

If a magnetic field B is present in this system, the phase difference associated with each link will be given by

$$\gamma_p=\frac{2\pi}{4p}(1-fp^2) \qquad (32)$$

where $f=Ba^2/\phi_0$ is the frustration index, i.e. the flux per cell in units of ϕ_0. The phases are subjected to the constraint

$$\sum_{i=1}^{4}\theta_i=2\pi(m-f) \qquad (33)$$

where m is the fluxoid quantum number. Fig. 1 gives a simple illustration of the above mentioned variables. It contains 9 unit cells with a vortex at the center. The central plaquette

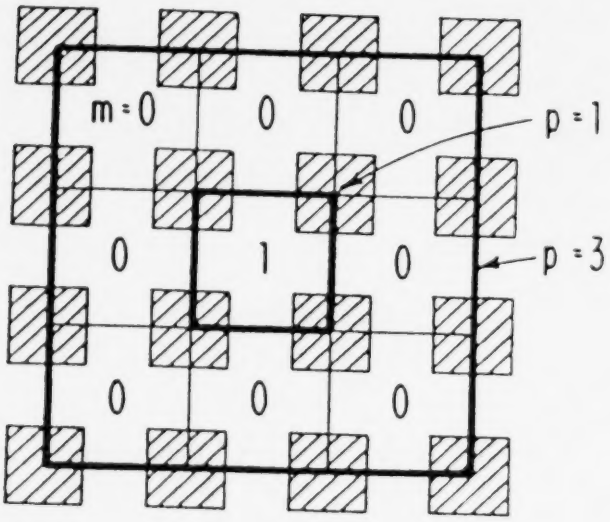

Fig. 1. Schematic representation of the 2-D discrete model. The hatched squares are the superconducting islands and the bold lines are the contours used in the sum (Equation 30 and 34). The lattice contains one vortex only at the center (m=1).

has p=1, the outer one has p=3; m=1 for the central cell and zero for the other eight; f=1/9 for the whole configuration.

In general, for f<<1, each m=1 cell is surrounded by many m=0 cells and the array could be treated as composed of a block containing 1/f cells with an m=1 cell in the center. In this case the increase in the energy due to the vortex will be given by

$$E=8E_J \sum_{p=1,3,5..}^{p_{max}} p\sin^2\left(\frac{\pi(1-fp^2)}{4p}\right) \qquad (34)$$

Note that $p_{max}\sim 1/f^{1/2}$ in order to have $m_{av}=f$. Accordingly the terms in the sum corresponding to the outer contours in the block are small because $(1-fp^2)\sim 0$. Consequently, only the central unit cell will dominate the sum and the energy increase will be given by

$$E=4E_J \qquad (35)$$

1.3.5. Vortex pinning in the discrete model:

The discrete model was used also to discuss vortex pinning in granular superconductors. Different pinning regimes have been considered:

(1) Pinning due to the discrete nature of the model.

(2) Pinning due to inhomogeneities in the physical parameters of the system.

The first regime has been studied by Lobb *et al*[33]. It was shown that for the vortex to move from one position to another, it should overcome an energy barrier. An illustration is shown in Fig. 2 which presents three possible positions of a vortex in a square lattice. Points a and c are equivalent and have energy minima while point b has an energy maximum. Calculations showed that for a vortex to move from position a to c it has to hop over an energy barrier of $0.2E_J$ which is 5% of the basic core energy ($4E_J$).

The second regime was discussed by Tinkham *et al*[31] and was attributed to the expected large scale inhomogeneities which stem from compositional variations and crystallographic defects. These features are reflected in the discrete model by having E_J take on a range of values in different links. Moreover, the coordination number affects the core energy for each link; e.g. the core energies of a vortex in 3- and 5-member plaquettes are $4.5E_J$ and $3.5E_J$ respectively instead of $4E_J$ in square plaquettes. Such variations in the core energy and in the magnitude of E_J may provide the pinning energy "U" for the vortex in granular superconductors.

1.3.6. Clem's model:

Clem *et al*[26] revealed that the dependence of I_{cJ} on temperature depends on the ratio between the junction coupling energy E_J and the condensation energy E_c

$$\varepsilon = \frac{E_j(T)}{E_c(T)} \qquad (36)$$

where $E_c(T)$ is

$$E_c(T) = \frac{H_c(T)^2}{8\pi V} \qquad (37)$$

Here V is the grain volume and H_c is the thermodynamical critical field. If $\varepsilon<1$ (weak coupling limit) the temperature dependence of I_{cJ} is that of Ambegaokar-Baratoff (linear close to T_c). For $\varepsilon>1$ (strong coupling limit) I_{cJ} varies with temperature in a similar way to the critical current of

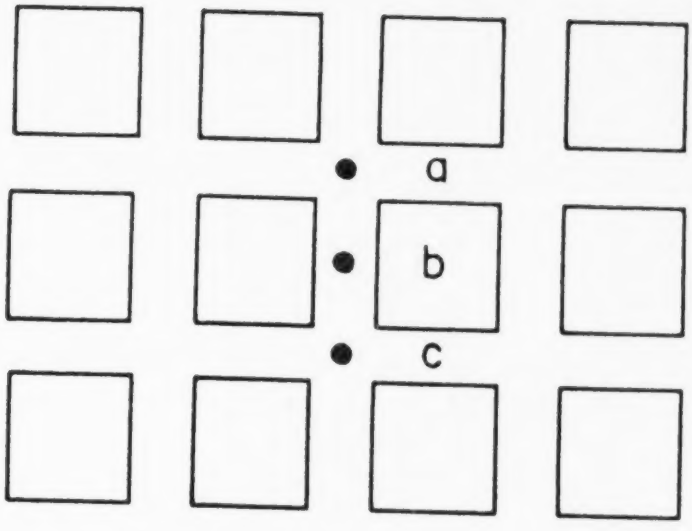

Fig. 2. Three positions for a vortex center in an array. Points a and c are equivalent; both have minimum energy. In order to move from a to c point b must be crossed, which is a position of maximum energy.

individual superconducting grains according to the Ginzburg-Landau approach. It should be noted that apart from a numerical factor of the order unity, $\varepsilon \sim (\xi/a)^2$, i.e. ε is determined by the ratio of the coherence length and the grain size.

1.3.7 Granularity in high-T_c ceramic superconductors:

Experiment[36,37] has shown that at low magnetic fields up to 200-300 G grain boundaries in ceramic YBCO behave like

junctions between weakly coupled superconducting grains. At higher fields weak links are decoupled but, however, there still exists a second non-weak link component of intergrain conduction which is not decoupled by the magnetic field. This component is believed to arise from regions of strong conduction within each grain boundary e.g. formed by microbridges of intrinsic grain-like material[38].

In spite of intensive studies of grain boundaries and weak links in YBCO there are still several problems crucial for the understanding of their superconducting properties which remain unsolved.

The first one concerned the intrinsic nature of superconducting weak links. It is unclear whether intergrain junctions are the superconductor-insulator-superconductor (SIS)-type Josephson tunnel junctions or the superconducting-normal-superconducting (SNS)-type proximity junctions and what is the mechanism by which the Ginzburg-Landau order parameter is suppressed at the grain boundaries. Resolving these questions could help to explain to what extent the low critical current density of YBCO ceramic samples is related to the intrinsic characteristics of the grain boundaries. The second problem concerns magnetic field effects on the critical current of intergrain junctions. While it is well documented that the intragrain j_c is controlled by the intragrain flux creep, no evidence was provided for an intergrain flux creep controlled transport current. An additional problem is to

distinguish between the current limiting behavior of grain boundaries in low magnetic fields and the changes in the transport current caused by the intergrain flux trapping and depinning.

1.4. Experimental Requirements:

Discussion of the two major issues; flux pinning/motion and weak links, requires detailed measurements of the transport current I. These measurements should include:

1) The decay of the transport current I with time at different temperatures and for a wide range of current between zero and the critical value I_c.

2) The dependance of the critical current I_c on temperature for various magnetic fields.

3) The dependance of the critical current I_c on magnetic field for various temperatures.

The experimental technique used in these measurements should be able to distinguish between intragrain and intergrain currents. Intragrain current is the microscopic current circulating around a flux line trapped in the grain of the superconductor (Abrikosov vortex). On the other hand, intergrain current is the macroscopic transport current carried by the sample and transmitted from one grain to the other through (or along) a grain boundary. A fundamental requirement in such measurements is to measure a real response of I_c to changing temperature, magnetic field and time. This is especially important at temperatures close to the transi-

tion temperature T_c. However, many experimental methods that have been used to estimate the transport critical current density in high temperature superconductors do not satisfy that requirement. The techniques widely applied for that purpose are:

1) The I-V four probe technique.

2) The AC magnetic method.

There are several reasons that make those two methods unreliable.

The problem with the I-V method is Joule heating at the contacts and the value of the minimum resistance, that can be measured usually in a range of about 10^{-7}-10^{-5} ohm. The latter is related to the sensitivity of the instruments and to a voltage (or an electric field) criterion of 0.1-2μV (1-10μV/cm) used to define the critical current. As a consequence, this method does not make a clear distinction between very low resistance and superconductivity. Its insensitivity to a resistive dissipation of supercurrent at temperature close to T_c seems to be the main reason for the observed discrepancy in the I_c vs temperature dependence reported by different groups for ceramic or thin film high-T_c materials.

The ac induction technique, on the other hand, uses ac susceptibility measurements and the critical state model (the Bean's critical state equation) to estimate critical currents. According to the Bean's critical state model[22], a superconducting sample responds to the external magnetic field

with shielding currents that flow at the level of critical current density j_c. In the case of ceramic samples diamagnetic shielding consists of two components: intergrain and intragrain ones. At low magnetic fields, superconducting ceramic samples exhibit strongly nonuniform distribution of intergrain shielding supercurrents because of the magnetic interaction between shielding current loops, and demagnetization effects at the sample edges. The estimation of the intergrain j_c in this case can be provided only via the invocation of a suitable critical state model. For this model to be valid, it must include the sample geometry and intragrain shielding currents flowing on the grain surface. These multiple factors make the ac methods very difficult to apply to ceramic samples at low magnetic fields.

In the next chapter, we describe the experimental procedure which uses persistent supercurrents flowing in a superconducting ring. Magnitudes of these currents and their critical values were determined using a contactless magnetic field measurement method. This procedure allowed us to measure (a) the magnitude of the maximum current as a function of temperature and applied field, and (b) the time decay of the current for various levels of current between zero and the critical value.

Measurements were performed on two types of YBCO materials: a grain-aligned c-axis oriented YBCO and polycrystalline non-grain-aligned ceramics of YBCO and RBCO where R=Gd, Eu,

Pr.

Experimental results obtained for different classes of samples under different cooling conditions are presented in Chapter 3. This includes detailed measurements of the dependence of the persistent current on temperature and magnetic field including time relaxation. Analysis of the experimental data and discussion of the results are given in Chapter 4. In this chapter some of the crucial issues are addressed such as the range of applicability of the classical model for flux motion to high temperature superconductors, the dependence of the energy barrier on current density, the estimate of the pinning potential as inferred from relaxation measurements and its temperature dependance, limitation of critical current in granular YBCO and the role played by flux creep in controlling the critical current close to T_c.

Along with conclusions in Chapter 5, we list some of the unsettled questions and suggest possible future research directions.

Chapter II

Experimental Procedure

The ultimate requirements for any experiment which probes the intrinsic characteristics of high-T_c superconductors using currents are (1) to be able to establish a persistent supercurrent which is self supported such that it gives an accurate response to changing temperature and applied magnetic fields, and (2) to avoid or minimize the effects of contacts (i.e. Joule heating) which reduce the sensitivity and result in inaccurate measurements especially at temperatures close to the transition temperature where the critical current is small.

Such requirements can be met if one induces persistent current in a ring-shaped sample. The magnitude of the current can be deduced from the profile of the magnetic field above the sample. The profiles of the magnetic fields are measured using a scanning cryogenic Hall probe.

2.1. Induction of persistent currents:

In order to induce a persistent current in a ring shaped sample one has to introduce flux lines into its central hole. Also one has to be able to generate this current in the absence and in the presence of the external magnetic field using zero field cooling and field cooling procedures, respectively. One could use the following procedure:

For the zero field cooling (ZFC) case the temperature of the sample, which is controlled by a non inductive foil

resistor as a heater and measured with both carbon-glass and platinum resistance thermometers, is brought to the operating temperature in the absence of any external magnetic field. After stabilizing the temperature, a small magnetic field is applied successively in a direction normal to the plane of the ring. The ring responds to the magnetic field by shielding its interior with diamagnetic surface currents. When the applied magnetic field increases flux lines will creep through the ring's bulk into the central hole. In the case of ceramic YBCO this process is facilitated by cutting small constrictions radially in the ring's bulk such that the bridges available for the flux lines to cross through the bulk are as small as possible. This geometry is shown in Fig. 3. Then the external magnetic field is reduced to zero. The ring responds to the new situation by establishing a persistent current which circulates around the ring in order to confine the flux lines inside the hole and prevent them from moving out. This current is directly proportional to the field trapped in the hole and is self-supporting. Further increase in the applied magnetic field results in increasing the trapped field and hence in increasing the persistent current. However, this process is limited by the maximum current that can flow in the sample at this particular temperature. Fig. 4 shows how the magnetic field due to the current builds up with increasing the applied magnetic field and Fig. 5 presents the saturation of the trapped field due to the persistent current when it reaches

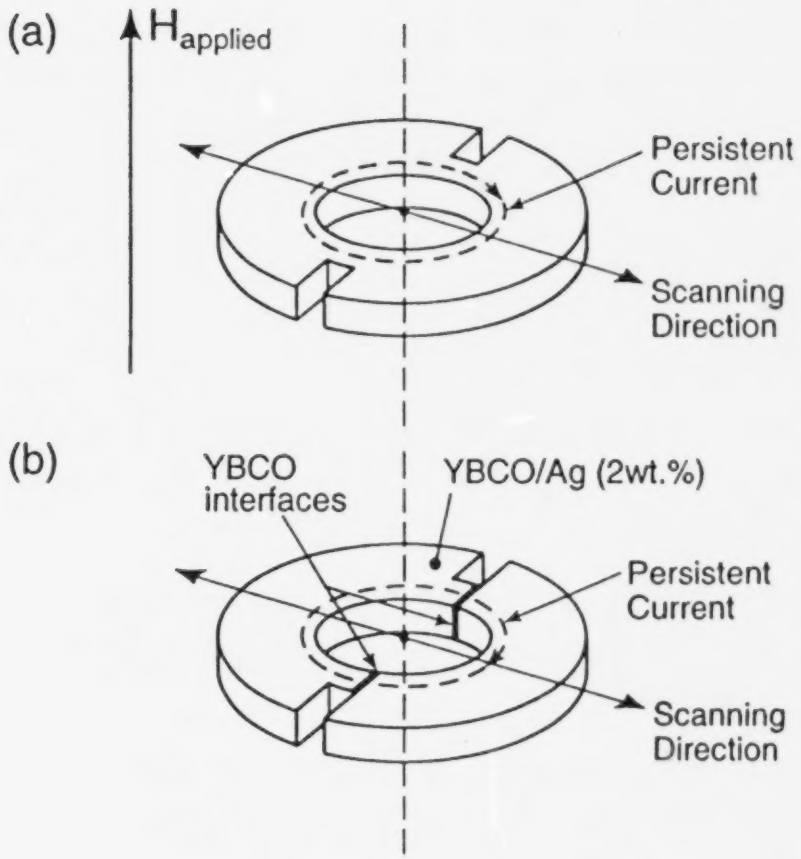

Fig. 3. Schematic of the ring's geometry used in the studies of the critical currents. Scanning direction denotes the direction of motion of a cryogenic Hall probe across the ring.
(a) The continuous ring prepared to measure the persistent current in YBCO and YBCO/Ag composites.
(b) The YBCO/Ag ring with two parallel YBCO interfaces prepared to investigate the role of intergrain microbridges in transporting current between grains.

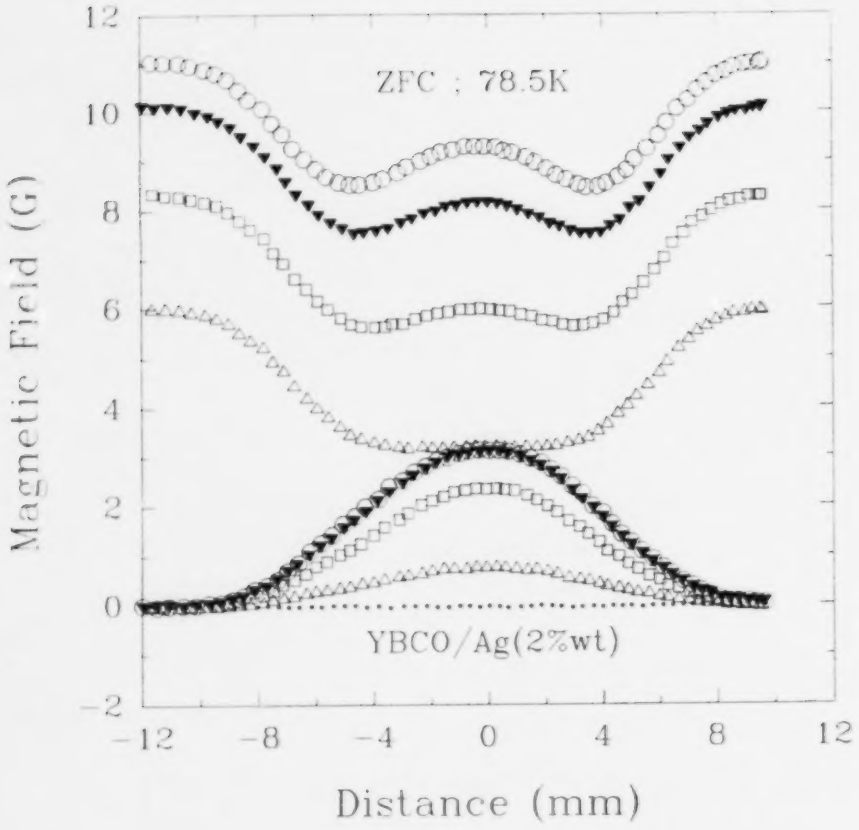

Fig. 4. The profiles of the magnetic field measured at 78.5K by a Hall probe above the zero field cooled ring of YBCO/Ag. The upper four curves show the profiles of the diamagnetic shielding measured at applied fields of 6.0, 8.4, 10 and 11 G. Note that the amount of the magnetic flux in the ring's hole increases with increasing the applied field. The corresponding four lower curves represent the magnetic field supported by a persistent current when the external field is reduced to zero. The amount of flux enclosed by the current saturates when the current reaches a critical value. The distances ±8 and ±3 mm mark the ring's outer and inner edges respectively.

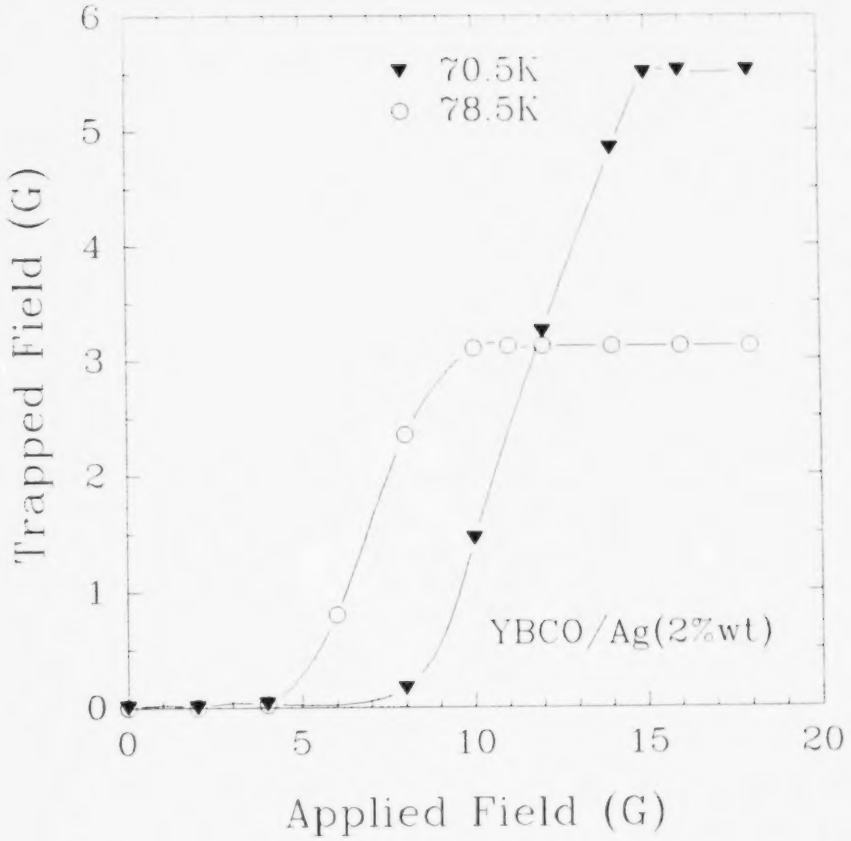

Fig. 5. Dependence of the magnetic field trapped in the ring's center on the applied field measured at 70.5 and 78.5 K. The magnitude of the trapped field is proportional to the persistent current I circulating around the ring, and its saturation value is proportional to the intergrain critical current I_c

its critical value.

In the case of field cooling (FC), an external magnetic field H_a is applied at a temperature $T>T_c$ followed by a decrease oftemperature down to the operating temperature $T<T_c$. This field H_a is kept constant during the experiment. At the operating temperature, an additional magnetic field is applied and then switched off as in the case of the zero field cooling. This is followed by the measurement of the axial component of the trapped field. However, the estimation of the critical current from the trapped field is not as simple as it is in the case of zero field cooling. The problem is that when the temperature is reduced below T_c in the presence of H_a,the magnitude of the field in the ring's hole is not equal to H_a, but to H_a-H_m, where H_m is the field resulting from Meissner expulsion (Fig 6). In this case, the trapped field is superimposed on the Meissner field. Similarly to the zero field cooling case, the critical value of the persistent current is determined from the saturation value of the axial component of the field trapped in the ring's central hole.

2.2. Magnetic measurements of the magnitude of the persistent current:

Some standard techniques (like the I-V technique) which are used to measure the current require contacts and leads attached to the sample and connected to the measuring instruments. Our alternative is to measure the magnitude of the trapped field in the central hole of the ring since it is

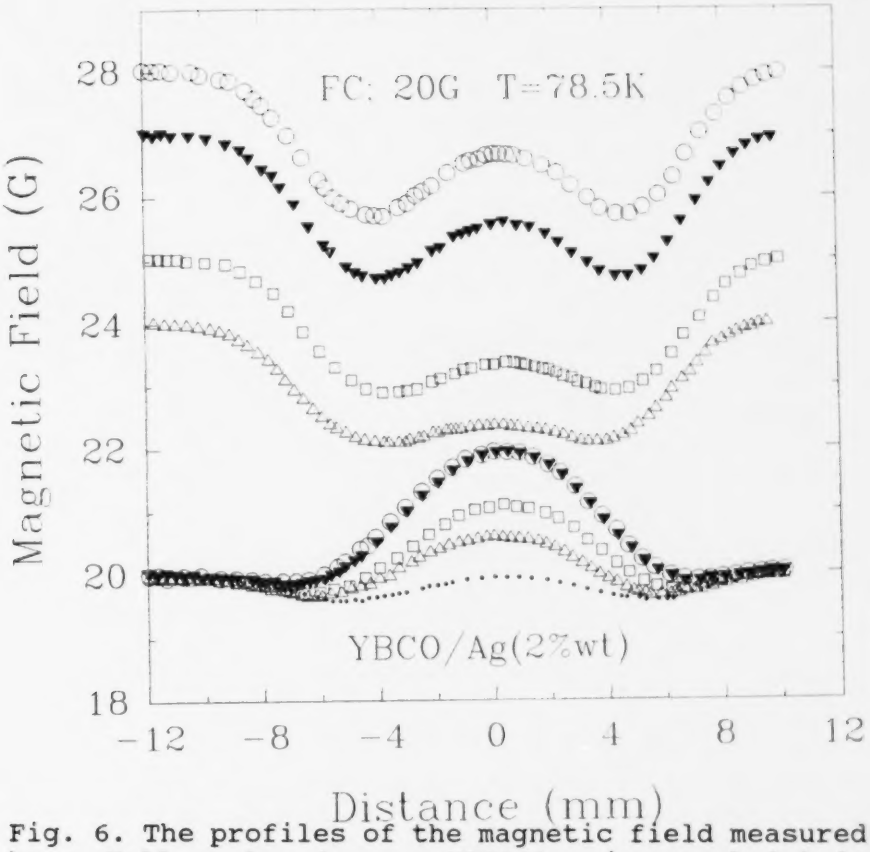

Fig. 6. The profiles of the magnetic field measured at 78.5 K by a Hall probe above a YBCO/Ag ring cooled below T_c in a field of 20 G. The dotted curve shows the profile of the Meissner field at 20 G. The upper four curves show the profiles of that Meissner field superposed on the shielding fields when the additional fields of 4, 5, 7, and 8 G were applied to the ring at a temperature of 78.5 K. Note that the amount of the magnetic flux in the ring's hole increases with the additional field. The corresponding four lower curves represent the Meissner field at 20 G superposed on the trapped field that was supported by the persistent current when the additional external field was removed. The saturation value of the trapped field is proportional to the intergrain critical current value at an applied field of 20 G. directly proportional to the magnitude of the persistent current circulating in the bulk, according to the Biot-Savart law. The profiles of the axial magnetic field produced by the persistent current are measured across the ring by an axial cryogenic Hall probe with sensitivity

of 20-30 mG over a temperature range 60-90 K and of sensitive area of 0.4mm^2. The probe is connected to a Gaussmeter and a computer controlled system which allows the measurements of magnetic field profiles over a scanning distance of 22 mm. The probe measures the component of the magnetic field perpendicular to the plane of the ring at a height of 2.0 mm from the ring's surface as measured at room temperature. Variation of that distance with temperature at low temperatures was tested using a copper wire wound ring-shaped coil instead of the sample. This coil was able to produce magnetic field profiles similar to those generated by the persistent current in the superconducting ring. It was found that the changes in the magnetic field recorded by the Hall probe were within 1.0% of the reading over the whole applied temperature range between 77K and 200 K.

The Hall probe scanning mechanism is capable of recording the field profiles produced by both the shielding currents (in the presence of the external applied field) and the persistent currents (after removing the external applied field). Shielding currents may have nonuniform distribution and lead to variations in the Lorentz force on vortices across the sample. Also they have two components which are hard to separate: (1) intergrain, and (2) intragrain currents. When the external applied magnetic field is reduced to zero, the superconducting ring responds by establishing a persistent current which confines the trapped field in the central hole. The persistent

current consists of the two components mentioned above but in this case it is easier to distinguish between them. The axial component of the persistent current's self-field (intergrain current) has a single maximum at the ring's center whereas a field due to magnetic vortices trapped in the bulk of the ring (intragrain current) has two maxima above the ring's bulk and a minimum in the ring's center. These vortices are of intragrain (Abrikosov) and intergrain (Josephson) nature, and the vortex field is superposed on the field profile generated by the persistent current as shown in Fig. 7. In order to avoid the contribution of the vortex field, the measurements of the critical current were performed on ceramic rings containing two parallel narrow constrictions (bridges) and at low applied magnetic fields up to 10-20 G. The bridges allow the creep of magnetic flux lines from outside into the ring's central hole at low magnetic fields and minimize trapping of intergrain vortices in the bulk of the ring. Profiles which are produced by persistent currents have very symmetric bell-like shape. Scanning of magnetic fields along, and normal to the bridges resulted in similar field profiles. Persistent currents are generated in the ring starting at low applied fields. This allows one to detect any changes in the symmetric bell-shaped profiles of the current self-field caused by the trapped vortices. The magnitude of the critical current is inferred from the maximum magnitude of the current's self-field at the ring's center using the Biot-Savart equation.

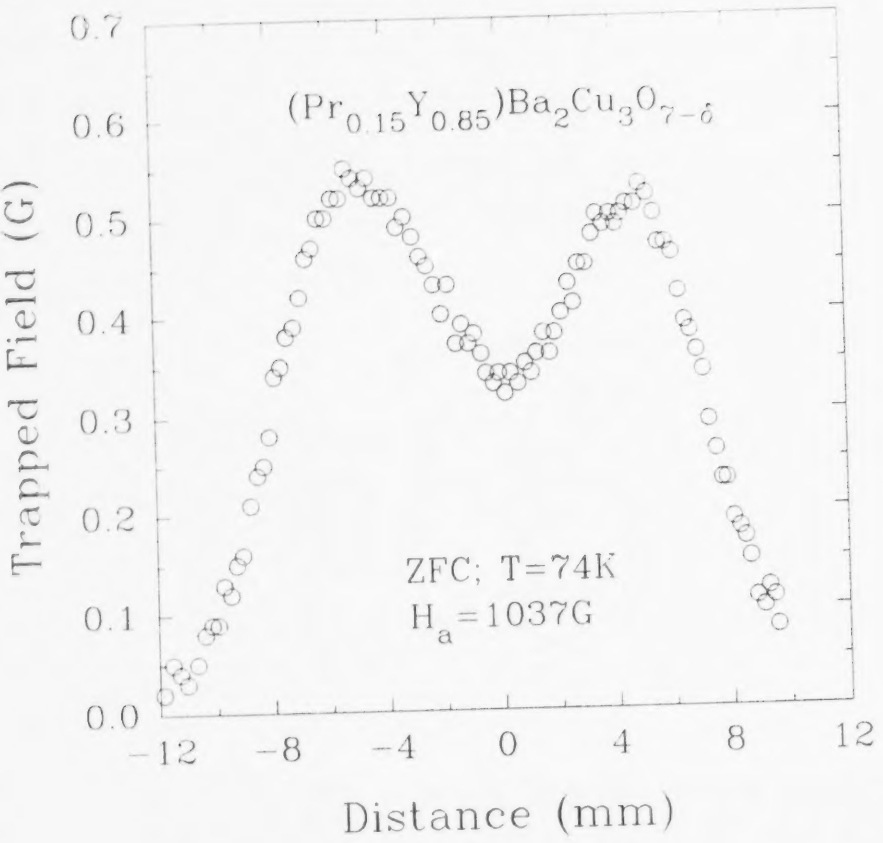

Fig. 7. The profile of the trapped magnetic field measured at 74 K by a Hall probe above the zero field cooled ring of $Pr_{.15}Y_{.85}Ba_2Cu_3O_{7-\delta}$ after applying and switching off a magnetic field H_a=1037 G. Magnetic vortices penetrate the grains causing the trapped field profile to have two maxima over the ring's bulk and one minimum at the center in contrast with the profiles shown in Figs. (2) and (3).

2.3. Measurements of the decay of persistent currents:

In typical measurements of the sample's zero field cooled magnetization (shielding), in the presence of external applied magnetic field H_a, the internal vortex field is $B_{int}=H_a-$

$\int j(B(r))dr$ where the second term on the right side is the field produced by shielding supercurrents induced in the sample. Nonuniform distribution of shielding currents leads to a variation of the Lorentz force across the sample. The measurements of the magnetization relaxation gives therefore a spatially averaged value of the effective energy barrier U_{eff}. A change in j can be achieved only by changing the sample's temperature. These problems can be avoided in experiments which detect the relaxation of the trapped magnetic flux instead of that of the shielding in ring shaped samples. In this case the internal magnetic induction is a sum of the vortex field trapped in the ring's bulk and the field generated by the persistent current.

Inducing a persistent current in the ring allows one to maintain a constant Lorentz force on the vortices and a constant normalized decay rate $(1/B)(dB/dt)$ at various points across the ring. The magnitude of the persistent current can be changed without changing the sample's temperature. This kind of measurement is equivalent to that of motion of vortices in the presence of a transport current set up by a constant current generator. In our studies the persistent current plays the role of the transport current, it is, however, possible to measure its decay.

The measurements of the decay of the persistent current were performed for symmetric bell-like profiles of the trapped field with a constant gradient of the magnetic induction

(+dB/dr) over the ring's bulk. This ensured elimination of negative gradients of the magnetic induction (-dB/dr) which could force magnetic vortices to creep towards the ring's center. The measurements of the decay of persistent currents in grain aligned materials have been initiated 30 sec after the external magnetic field was reduced to zero and terminated within 20,000 sec. The long time used in these measurements allows us to distinguish between transient and steady state behavior of the persistent current. In polycrystalline ceramic samples, the relaxation of the persistent current was measured for times up to 20,000 sec. However, it was found that transient regimes are not predominant in these materials and steady state relaxation is reached much faster than in the grain aligned materials. Consequently, it was sufficient to record time decays up to 1000 sec in ceramic samples. A schematic of the experimental set-up and its various components is presented in Appendix B.

2.4. Samples preparations:

Two types of YBCO samples were investigated in this work: (1) grain-aligned c-axis oriented, and (2) polycrystalline ceramics.

Samples of grain-aligned YBCO have been prepared using the melt-powder-melt-growth (MPMG) process[39,40] in the Superconductivity Research Laboratory (SRL) at ISTEC, Japan. This method proved to be effective in manufacturing c-axis oriented grain aligned bulk YBCO superconductors whose low

angle grain boundaries are capable of carrying large critical current densities. On the other hand introducing fine (0.5-1μm) second phase particles of Y_2BaCuO_5, was believed to enhance pinning of magnetic vortices. The material used in these studies was as-processed $Y_1Ba_2Cu_3O_{7-\delta}$ containing 28 mol.% of Y_2BaCuO_5 inclusions. Ring shaped specimens were cut from this material. Four cases were studied whose specifications are shown in Table 1.

Sample	Dimensions	Description
GAR1	I.D. = 6.0 mm O.D. = 10.0 mm Thickness = 1.0 mm Width of the bulk = 2.0 mm	Continuous ring, same cross sectional area for the whole bulk
GAR2	Same as GAR1	This ring has radial 1 mm notches cut through the bulk to create narrow bridges as shown in Fig. 3.
GAR3	Same as GAR1	Same as GAR1
GAR4	I.D. = 6.0 mm O.D. = 10.0 mm Thickness = 0.7 mm	This ring was made by thinning down GAR3 to 2/3 of its original thickness.

Table 1: Dimensions and description of grain aligned YBCO samples.

The superconducting properties of the samples were analyzed with ac pickup coils[1] and a scanning Hall probe system. The ac-susceptibility (χ_{ac}) measurements were done using a frequency of 3 kHz for $(H_{ac})_{rms}$=1.8 G. The measurement of the real part (χ') of ac-susceptibility gave a transition temperature T_c(ac-susceptibility)=89 K and its width ΔT_c~1 K. The imaginary part (χ'') of χ_{ac} exhibits a single sharp peak at 88.5 K. A Hall probe was able to detect a magnetic flux trapped in the ring's bulk at temperatures up to 89.5 K.

Polycrystalline samples of YBCO were prepared using the standard solid state Reaction method. First a homogeneous mixture of high purity oxides Y_2O_3 and CuO, and carbonate $BaCO_3$ was prepared in a form of powders. The powders were pressed under a pressure of 2.5-2.7 kbar forming disks with diameter of 16 mm. The disks were calcined in air or flowing pure oxygen for 24 hours at temperatures of 925-950°C. The resulting product was pulverized and new disk shaped pellets, 16.0 mm diameter and 3.0 mm thick, were formed under a pressure of 6.2 kbar. The disks were sintered in flowing oxygen at 925-930°C for 7 hours and cooled at variable rates down to the room temperature (3°C/min. between 925 (930) and 700°C and 1°C/min. below 700°C). After sintering a 6.0 mm diameter hole was cut in the disk center using a diamond drill sprayed with water. The resulting ring was then cut along its

---

[1] ac-susceptibility measurements have been performed at the University of Lethbridge, Lethbridge, Alberta, by Dr. M. Mohamed.

diameter in order to form two bridges of width 1.0 ~ 1.5 mm close to the inner hole, as shown in Fig. 3. The effect of the bridges on magnetic field profiles is discussed in Apendix C.

In another group of samples silver was introduced to form YBCO-Ag composites (YBCO + Ag(x%wt) where x = 2 and 4). In this case, silver powder was added to YBCO before the sintering process. Special ceramic rings of YBCO-Ag composite containing two parallel superconducting interfaces were manufactured. The interfaces were prepared by cutting a continuous ring of YBCO/Ag (2% wt) composite along its diameter and through the constrictions, evaporating a few microns of silver on the cut surfaces and welding (sintering) the assembled two pieces of the ring under an axial stress of 6.6 g/mm^2 perpendicular to the contact surface. This process was carried out at a temperature of 930°C for 5 hours in an atmosphere of flowing oxygen. The rings obtained using this procedure contain the superconducting interfaces within the bridges which limit the ring cross sectional area available for the current. The interfaces were investigated using the scanning electron microscope. The interfaces are of a thickness of about 5~10 microns, they do not contain silver and are highly porous.

Variation from the standard structure of YBCO was achieved in a group of rings by substituting yttrium, partially or completely, with other rare earth elements. Praseodymium was substituted for yttrium in two rings forming compounds of

$Pr_{0.15}Y_{0.85}Ba_2Cu_3O_{7-\delta}$ and $Pr_{0.2}Y_{0.8}Ba_2Cu_3O_{7-\delta}$. This was done by replacing the proper portion of Y_2O_3 with Pr_6O_{11} oxide. The powder was calcined at 905°C for a total time of 137 hours. The powder was recrushed and annealed three times during the calcining process, then pressed into disk shaped samples and sintered in flowing oxygen for 7 hours at a temperature of 920°C. $Gd_1Ba_2Cu_3O_{7-\delta}$ and $Eu_1Ba_2Cu_3O_{7-\delta}$ compounds were manufactured by replacing Y_2O_3 oxide with Gd_2O_3 and Eu_2O_3 respectively, and using calcining and sintering procedure similar to those used to produce $Y_1Ba_2Cu_3O_{7-\delta}$ compounds. Tables (2), (3) and (4) summarize the composition, preparation conditions, geometry and dimensions of different rings in various groups of compounds.

Group	Ring	Composition	Calcining Conditions				
			#	P kbar	T °C	t hrs	Gas
A	PCR-A1	YBCO	1	2.7	950	24	air
	PCR-A2	YBCO	1	2.7	950	24	air
	PCR-A3	YBCO	1	2.5	925	24	O_2 flow 1 LPM
B	PCR-B1	YBCO/Ag(2%wt)	1	2.7	925	24	O_2 flow 1 LPM
	PCR-B2	YBCO/Ag(2%wt)	1	2.7	925	24	O_2 flow 1 LPM
	PCR-B3	YBCO/Ag(2%wt)	1	2.7	925	24	O_2 flow 1 LPM
	PCR-B4	YBCO + Ag(4%wt)	1	2.7	925	24	O_2 flow 1 LPM
	PCR-B5	YBCO + Ag(4%wt)	1	2.7	925	24	O_2 flow 1 LPM
C	PCR-C1	YBCO/Ag(2%wt)	1	2.3	925	24	O_2 flow 0.6 LPM
	PCR-C2	YBCO/Ag(2%wt)	1	2.3	925	24	O_2 flow 0.6 LPM
D	PCR-D1	$Gd_1Ba_2Cu_3O_{7-\delta}$	1	2.7	950	24	air
	PCR-D2	$Eu_1Ba_2Cu_3O_{7-\delta}$	1	2.7	950	24	air
	PCR-D3	$(Pr_{.15}Y_{.85})$BCO	3	none	905	138	air
	PCR-D4	$(Pr_{.2}Y_{.8})$BCO	3	none	905	138	air

Table (2): Calcining conditions of polycrystalline ceramic rings. # is the number of times the sample was calcined, P is the compacting pressure of pellets during preparation, T is the calcining temperature and t is the calcining time. The gas column presents the type of gas used in the calcining process. When oxygen is used, the flow rate is given. Note that samples PCR-D3 and PCR-D4 were calcined in the form of a powder.

Group	Ring	Composition	Sintering Conditions				
			#	P kbar	T °C	t hrs	O_2 flow LPM
A	PCR-A1	YBCO	2	6.2	930	7	0.5
	PCR-A2	YBCO	2	6.2	930	7	0.5
	PCR-A3	YBCO	1	6.2	925	7	1.0
B	PCR-B1	YBCO/Ag(2%wt)	1	6.2	925	7	1.0
	PCR-B2	YBCO/Ag(2%wt)	1	6.2	925	7	1.0
	PCR-B3	YBCO/Ag(2%wt)	1	6.2	925	7	1.0
	PCR-B4	YBCO + Ag(4%wt)	1	6.2	925	7	1.0
	PCR-B5	YBCO + Ag(4%wt)	1	6.2	925	7	1.0
C	PCR-C1	YBCO/Ag(2%wt)	1	6.2	925	7	1.0
	PCR-C2	YBCO/Ag(2%wt)	1	6.2	925	7	1.0
D	PCR-D1	$Gd_1Ba_2Cu_3O_{7-\delta}$	2	6.2	920	7	0.5
	PCR-D2	$Eu_1Ba_2Cu_3O_{7-\delta}$	2	6.2	920	7	0.5
	PCR-D3	$(Pr_{.15}Y_{.85})$BCO	2	6.2	920	7	0.5
	PCR-D4	$(Pr_{.2}Y_{.8})$BCO	2	6.2	920	7	0.5

Table (3): Sintering conditions of polycrystalline ceramic rings. Note that the two samples in group C received an extra sintering during the process of welding the two semi-rings as described in the text.

Group	Ring	Dimensions	Bridges	Inter-faces
A	PCR-A1 YBCO	I.D.= 6mm O.D.= 15mm t=3mm	Yes	No
	PCR-A2 YBCO	same as A1	Yes	No
	PCR-A3 YBCO	same as A1	Yes	No
B	PCR-B1 YBCO/Ag(2%wt)	same as A1	Yes	No
	PCR-B2 YBCO/Ag(2%wt)	same as A1	No	No
	PCR-B3 YBCO/Ag(2%wt)	I.D.= 10mm O.D.= 15mm t=3mm	No	No
	PCR-B4 YBCO + Ag(4%wt)	same as A1	No	No
	PCR-B5 YBCO + Ag(4%wt)	I.D.= 6mm O.D.= 11.5mm t=3mm	No	No
C	PCR-C1 YBCO/Ag(2%wt)	same as A1	Yes	Yes
	PCR-C2 YBCO/Ag(2%wt)	same as A1	Yes	Yes
D	PCR-D1 $Gd_1Ba_2Cu_3O_{7-\delta}$	same as A1	Yes	No
	PCR-D2 $Eu_1Ba_2Cu_3O_{7-\delta}$	same as A1	Yes	No
	PCR-D3 $(Pr_{.15}Y_{.85})$BCO	same as A1	Yes	No
	PCR-D4 $(Pr_{.2}Y_{.8})$BCO	same as A1	Yes	No

Table (4): Dimensions and geometry of polycrystalline ceramic rings.

Chapter III

Experimental Results

3.1 Experimental results for the grain-aligned YBCO:

The measurements of the magnitude and decay of supercurrents in the four ring-shaped samples of grain-aligned YBCO, described in Table 1, were performed over a temperature range of 78 - 90 K and a time range between 30 and 20,000 sec. In all four cases, the magnetic field was applied in a direction parallel to the c-axis and normal to the ring's plane and the supercurrent circulated around the central hole in the ab plane. *The temperature and time dependence of the supercurrent were the same in all four cases except the magnitude of the current, which is a strong function of the geometry and the dimensions of the sample under consideration.*

Figures 8 and 9 show profiles of the axial component of the magnetic field generated by the persistent current circulating in a zero field cooled ring. This magnetic field was measured at 81 K and 85 K for various levels of persistent current between zero and the critical value. The profiles shown in these figures are typical for the axial component of the trapped field for the whole temperature range (78 - 90 K) measured in the four samples of grain aligned, c-axis oriented YBCO rings. A magnetic field up to 1200 G was used to generate different values of persistent current. A bell-shaped profile of the trapped field is an indication that the persistent

current is proportional to the magnetic field trapped in the ring's central hole. At low enough applied magnetic fields, e.g. up to 150 G at 85 K, the magnetic flux is mostly trapped in the ring's bulk resulting in asymmetric trapped profiles which have two maxima above the ring's bulk and a minimum at the ring's center.

Figures 10 and 11 show typical profiles of the diamagnetic shielding fields H_s normalized to the applied magnetic field H_a, which were measured above a zero field cooled ring for different applied fields up to 1000 G at 81 K and 500 G at 85 K. The dependence of the axial component of the trapped magnetic field on the applied field revealed that above a certain applied field, the magnetic field generated by the persistent current saturates. Figure 12 shows this for T = 81 K and T = 85 K, indicating that the magnitude, I, of the persistent current is close to its critical value I_c. The difference between I and I_c depends on the relaxation phenomena. Dependence of the shielding field on the applied field at 81 K is shown in Figure 13. The applied magnetic field at which the flux lines penetrate the sample corresponds to that at which the shielding field vs. the applied field curve deviates from the linear behavior. For example, Figure 13 reveals that for the grain aligned ring GAR1 at 81 K flux lines start to penetrate the sample when the magnitude of the applied magnetic field exceeds 300 G.

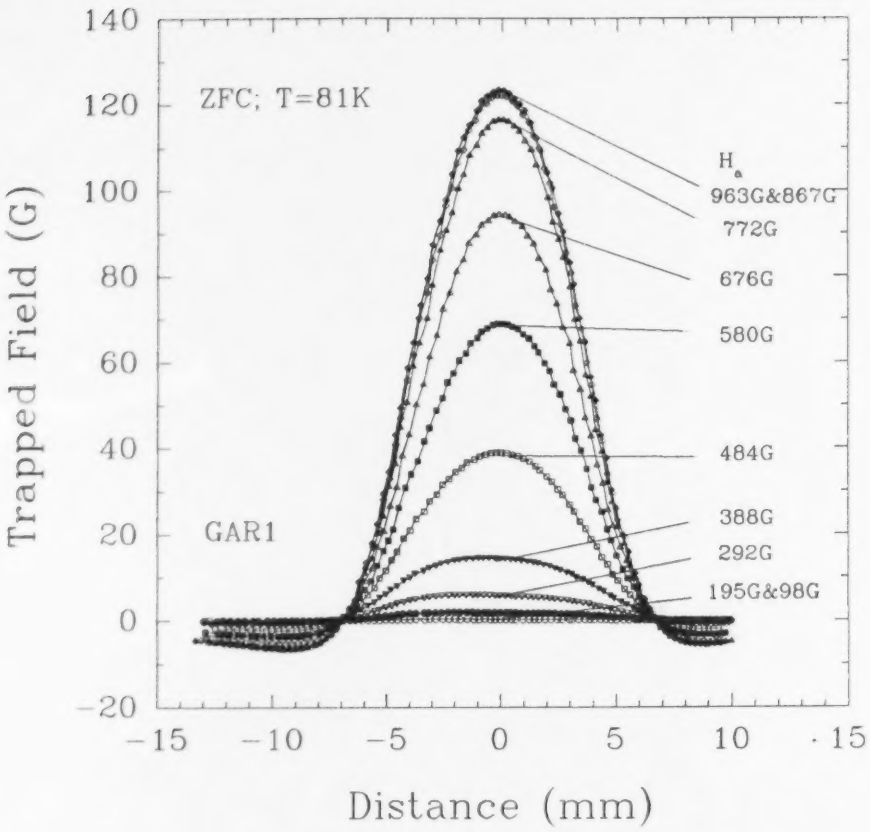

Fig. 8. The profiles of the axial component of the trapped magnetic field generated at 81 K by the persistent current circulating in the zero field cooled grain-aligned YBCO ring (No. GAR1) with the c-axis parallel to the ring's axis. Various profiles represent various levels of the persistent current between zero and the critical value. The persistent current was induced by applying external magnetic field up to 1000 G. Distances +5, -5 mm and +3, -3 mm mark the ring's outer and inner radii, respectively.

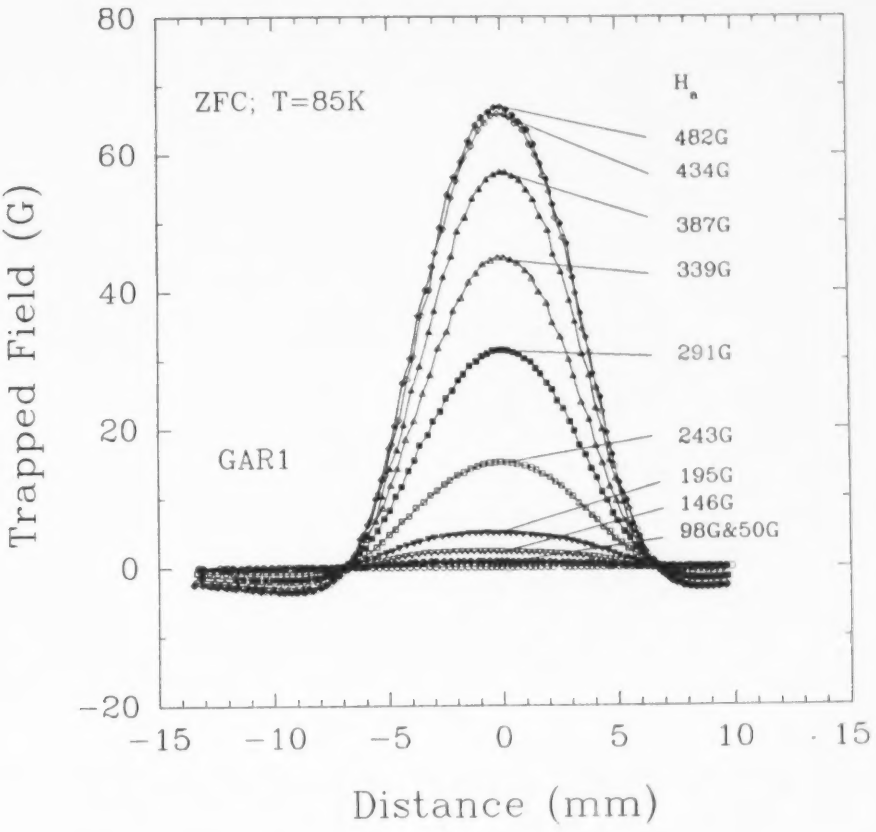

Fig. 9. The profiles of the axial component of the trapped magnetic field generated at 85 K by the persistent current circulating in the zero field cooled grain-aligned YBCO ring (No. GAR1). The persistent current was induced by applying external magnetic fields up to 500 G.

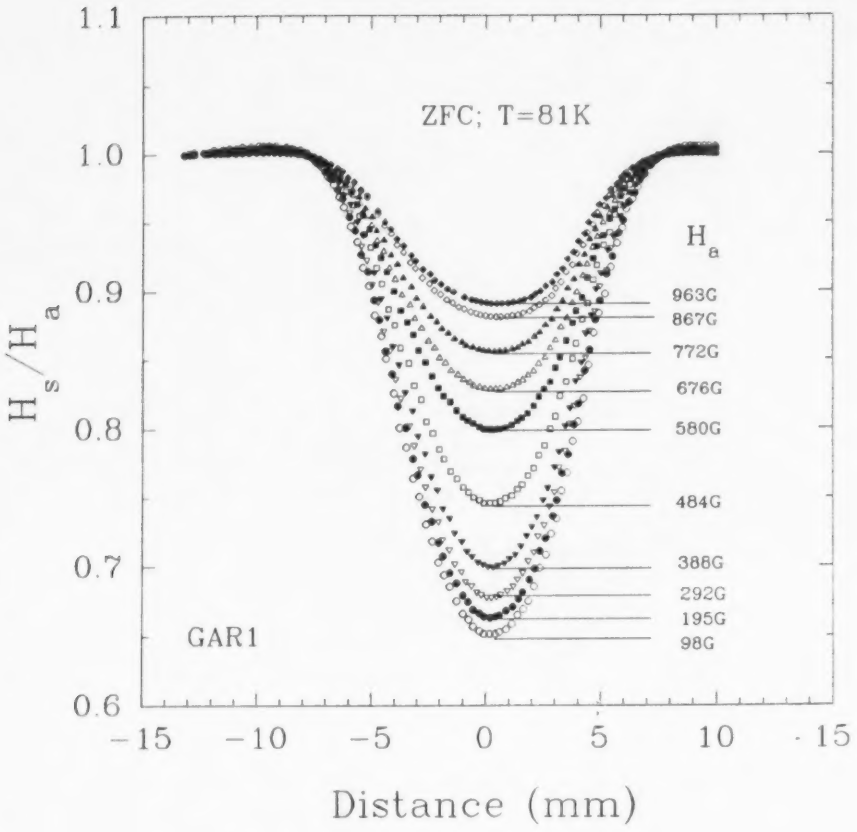

Fig. 10. The profiles of the shielding field H_s, normalized to the applied magnetic field H_a, which was generated at 81 K by the diamagnetic shielding currents circulating in the zero field cooled grain-aligned YBCO ring (No. GAR1). The profiles are measured in the presence of the external magnetic field, and each one has its corresponding trapped field profile in Fig. 6.

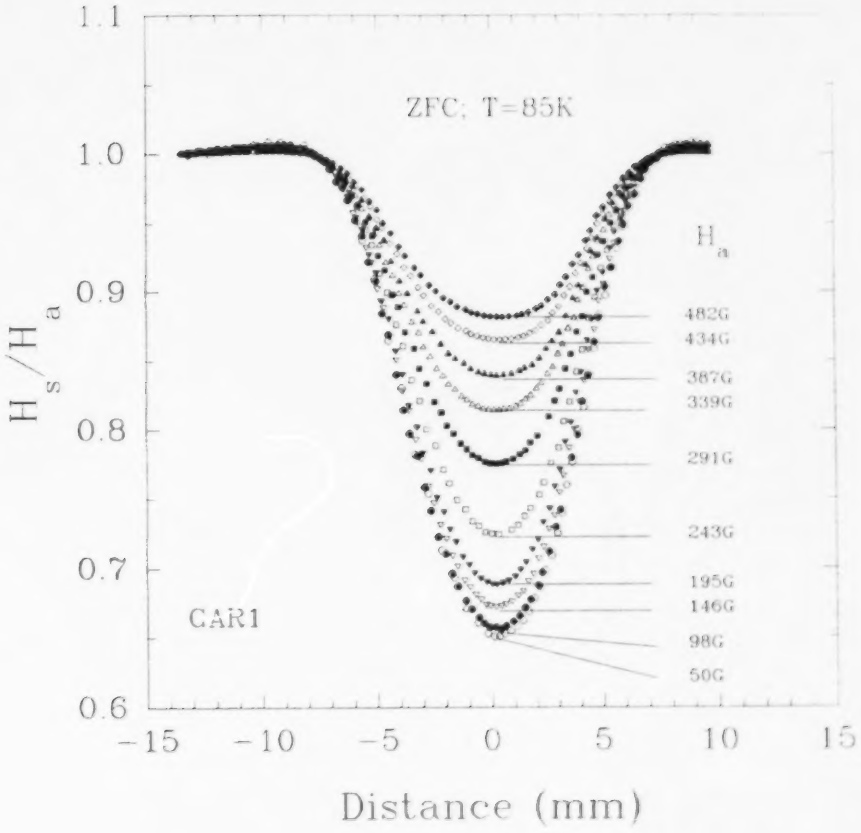

Fig. 11. The profiles of the shielding field H_s, normalized to the applied magnetic field H_a, which was generated at 85 K by the diamagnetic shielding currents circulating in the zero field cooled grain-aligned YBCO ring (No. GAR1). Each profile has its corresponding trapped field profile in Fig. 7.

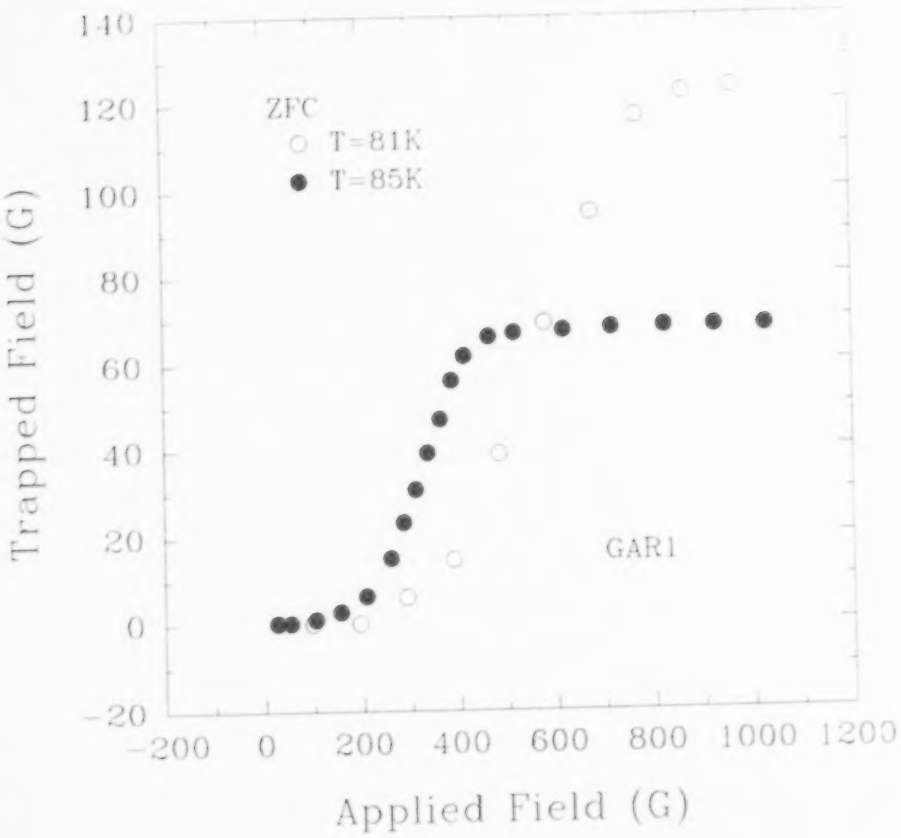

Fig. 12. Dependence of the axial component of the persistent current's self-field on the applied field measured at 81 and 85 K above the center of a zero field cooled grain-aligned YBCO ring (No. GAR1). The trapped field saturates for applied fields above 800 G at 81 K and 400 G at 85 K. Measurements were performed 30 s after the applied field was switched off.

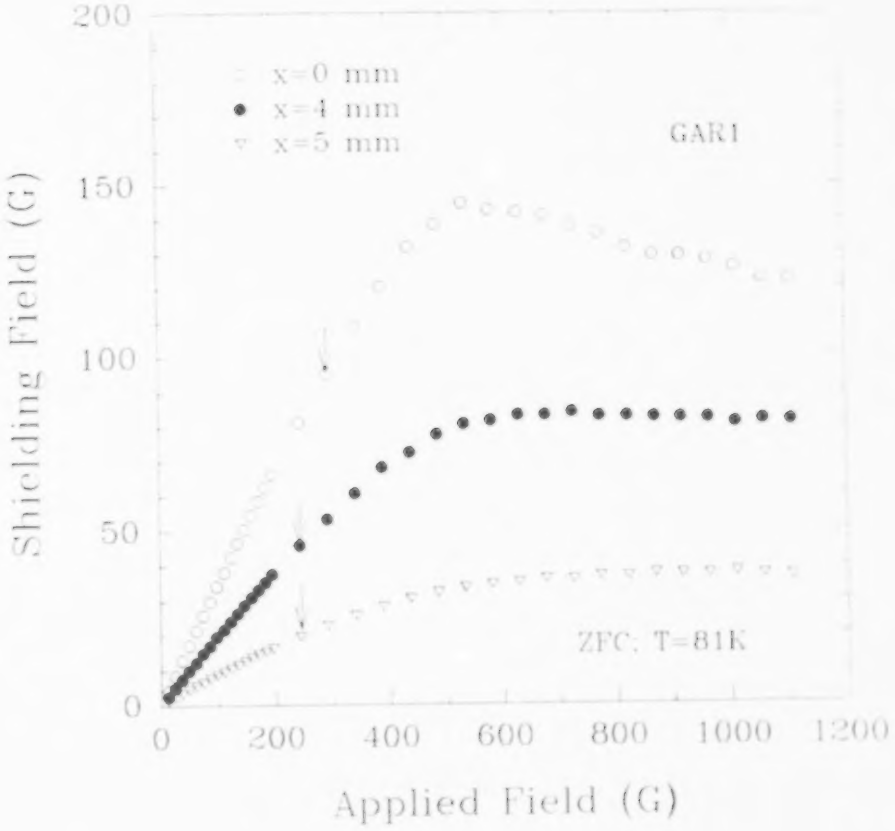

Fig. 13. Dependence of the shielding field measured above the center, the bulk and the edge of a zero field cooled grain-aligned YBCO ring (No. GAR1), on the applied field at T=81 K. x denotes the position of the Hall probe measured from the center of the ring and the arrows mark the fields at which the shielding field vs. the applied field curve deviates from the linear behavior at each of the above specified positions.

The decay of the persistent current has been measured over a time range between 30 sec and 20,000 sec and over a temperature range 78 K - 90 K *in all four zero field cooled grain-aligned YBCO samples*. Figures 14 and 15 present the decays of the persistent current from various levels between zero and I_c measured in two samples at temperatures 81 K and 85 K respectively. The currents of an initial magnitude I_0^{max} close to I_c exhibit the fastest decays which approach a steady state logarithmic relaxation after approximately 1000 sec. I_0^{max} was calculated from the saturation value of the persistent current's self-magnetic field measured as a function of the applied field (see Figure 12). The measurements of I_0^{max} were done 30 sec after the external applied field was reduced to zero. The current of an initial magnitude I_0 below approximately $0.75I_0^{max}$ experiences a slow initial decay which eventually converges into a steady state logarithmic decay after waiting a certain time, t_p. The normalized decays $I(t)/I(0)$ of this slow initial relaxation for $I_0 \leq 0.75I_0^{max}$ are weakly dependent on the initial current I_0. This can be seen from curves (a) 1-4 and (b) 1-3 in Figures 16 and 17 which show the dependence of the persistent current normalized to its initial value, on time. The initial slow decays for $I_0 \leq 0.75I_0^{max}$ are non-logarithmic in time and can be easily distinguished from fast logarithmic decays measured after 1000 sec for initial currents I_0 close to I_c. These logarithmic decays are characterized by the same value of the normalized

logarithmic decay rates $S=(1/I_0)dI/dln(t)$, see curves (a) 5-10 and (b) 4-9 in Figure 16. The maximum trapped field profiles at T=81K measured initially at t=30 sec and after 20,000 sec are shown in Figure 18. The profiles reveal that the percentage of the trapped field which creeps out of the sample during the relaxation process is the same along the ring diameter, i.e. (1/B)dB/dlnt=constant across the ring.

The magnitude of I_0 could be controlled not only via the external applied magnetic field required to set up the persistent current in the ring, but also through a flux creep annealing technique[8,21]. Figure 19 shows the decay rates of the persistent currents measured at T=81 K in ring No. GAR1 and at T=85 K in ring No. GAR3 without and with annealing. The annealing was carried out by establishing the maximum persistent current at T=81 K (or 85 K), warming up the sample by either 0.5 K or 1 K, then cooling down again to 81 K (or 85 K). The curves show that all decays will converge into a logarithmic decay after time t_p which varies with the initial current I_0. For initial currents $I_0<I_c$, the relaxation begins with successively smaller values of the initial current decay rate and t_p increases with decreasing the initial current.

The relaxation phenomena described above are typical for a temperature range of 78-88 K. When the temperature approaches T_c, a dramatic decrease of the decay rates occurs at temperatures between 88.5 K and 90 K. This effect is seen at a temperature of 88.5 K in Figure 20 for all magnitudes of the

persistent current I_0 between 0 and I_c. Figures 21 and 22 present a gradual decrease in the decay rate for the decays from I_0 close to I_c with increasing temperature from 88.6 K up to 89.1 K for ring No. GAR1 and from 88.5 K up to 88.9 K for ring No. GAR3.

The dependence of $I_0^{max} \approx I_c$ on temperature for the ZFC case is shown in Figure 23. The four plots represent the four cases which have been investigated (GAR1, GAR2, GAR3 and GAR4). The temperatures at which I=0 were found to vary between 89.5 K and 90.5 K. In Figure 24, the current $I_0^{max} \approx I_c$ is plotted vs temperature for a temperature range of 85 K to 90 K for the grain aligned YBCO ring No. GAR1 for ZFC and FC cases. For temperatures below 88.5 K the dependence of the current on temperature is linear. However, when the temperature approaches T_c, this dependence is no longer linear. Deviations from the linear dependence are also seen for the field cooling cases. The dependence of the critical current $I_0^{max} \approx I_c$ on the applied field measured at different temperatures: (a) 85 K and 87 K in the grain aligned YBCO ring No. GAR1 and (b) 86 K, 87 K and 88 K in the grain-aligned YBCO ring No GAR3 is shown in Figure 25 for fields up to 700 G for GAR1 and 1000 G for GAR3. The behavior of I(H) resembles that of Kim[43], $I(H) \propto 1/H$.

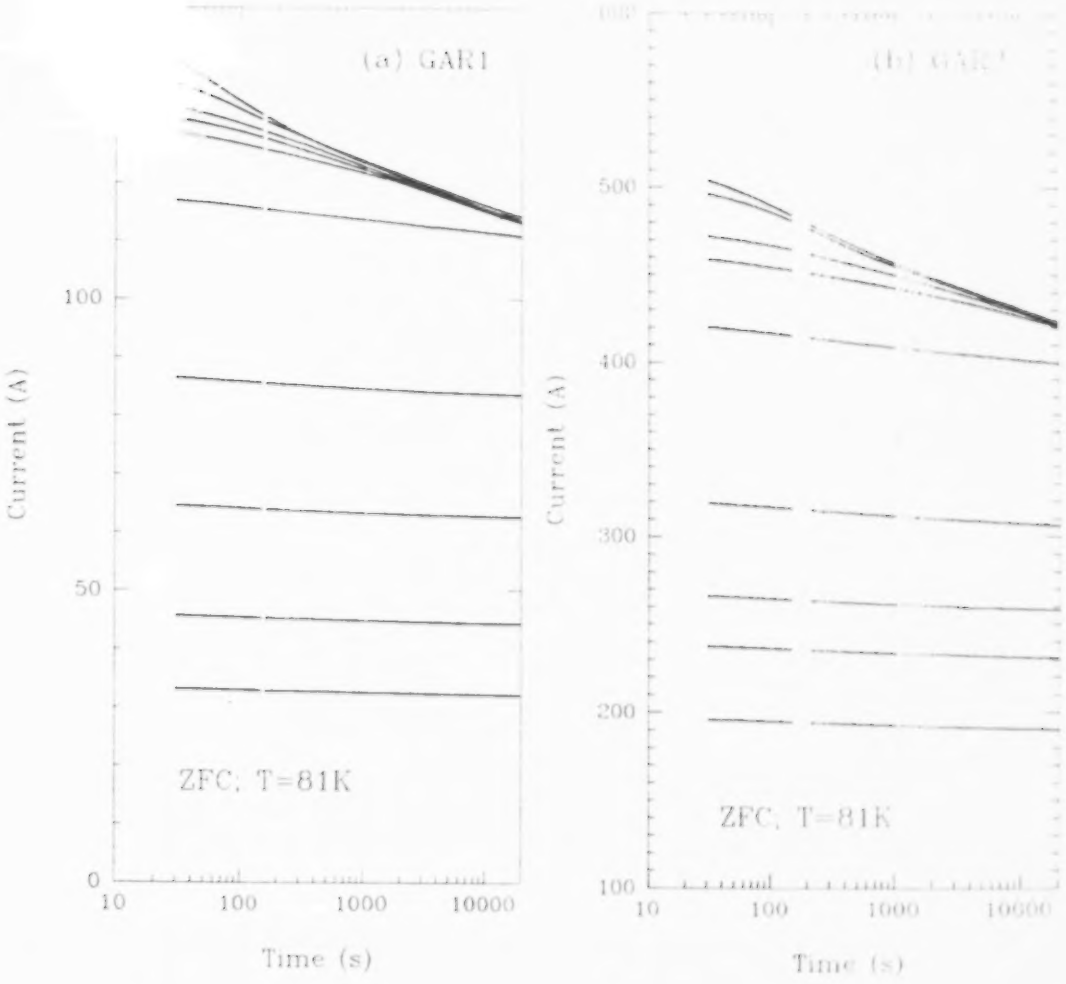

Fig. 14. Dependence of the persistent current flowing in the zero field cooled grain-aligned YBCO rings: (a) GAR1 and (b) GAR3 on time over a range between 30 and 20,000 sec at 81 K. The slow initial decays converge into a long term steady state logarithmic decay.

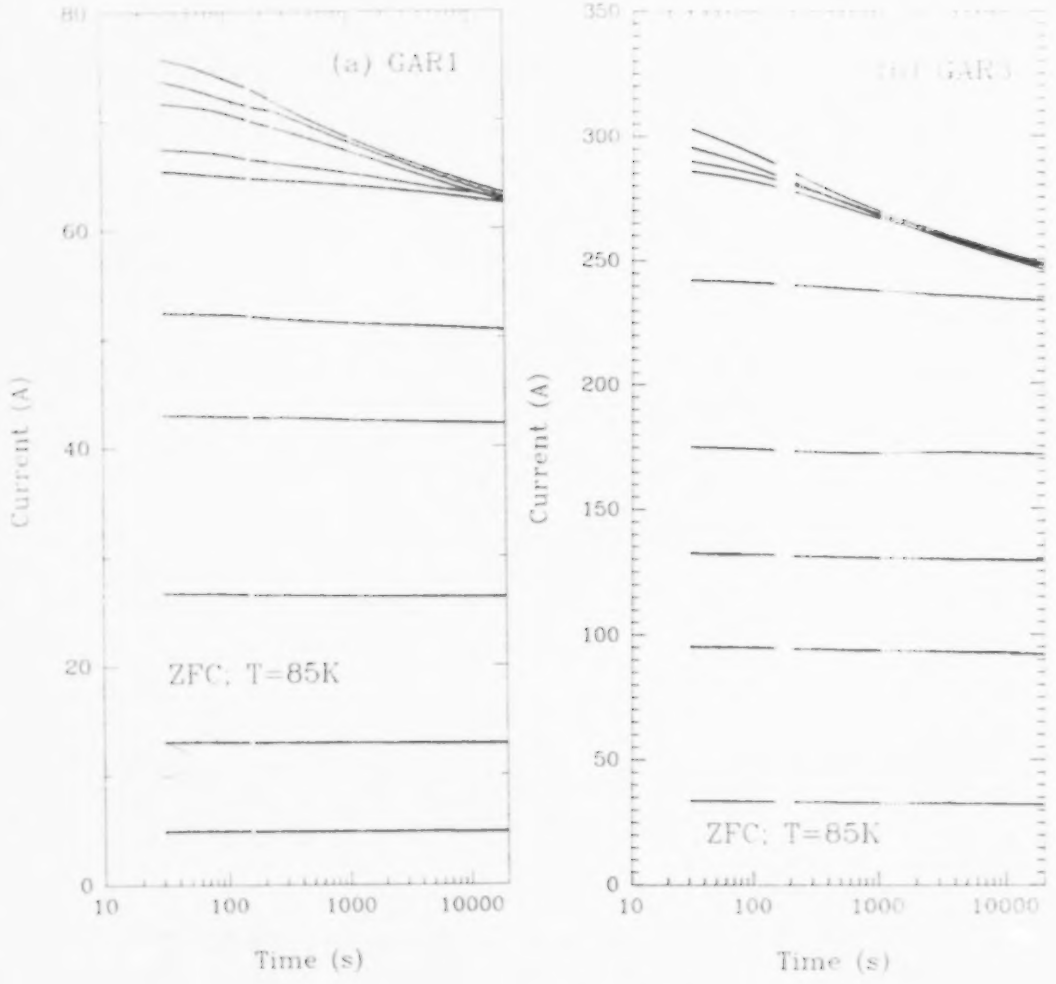

Fig. 15. Dependence of the persistent current flowing in the zero field cooled grain-aligned YBCO rings: (a) GAR1 and (b) GAR3 on time over a range between 30 and 20,000 sec at 85 K.

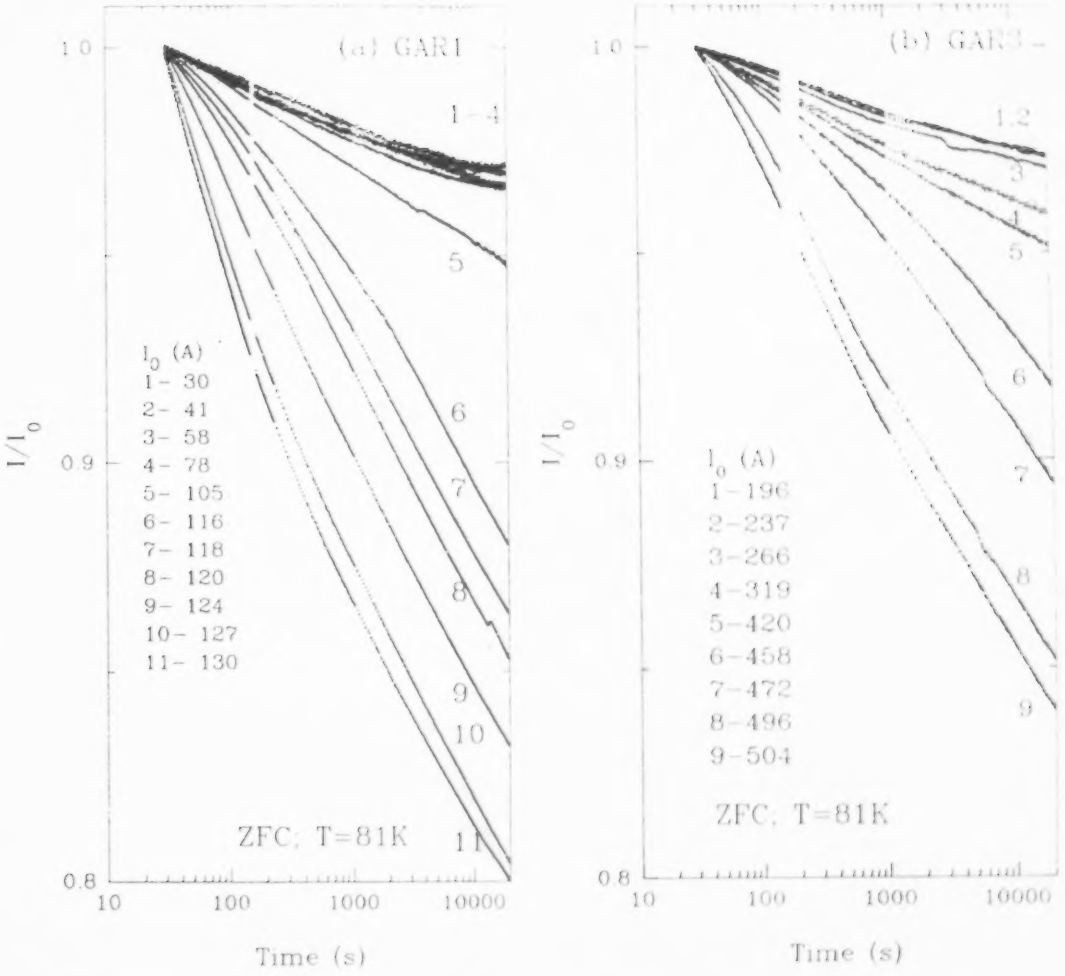

Fig. 16. Dependence of the persistent current normalized to an initial value I_0 in the zero field cooled grain-aligned YBCO rings: (a) GAR1 and (b) GAR3 on time over a range of 30 to 20,000 sec at 81 K. For small I_0 (see curves 1-4 in (a) and 1-3 in (b)) the normalized decay rates are independent of I_0.

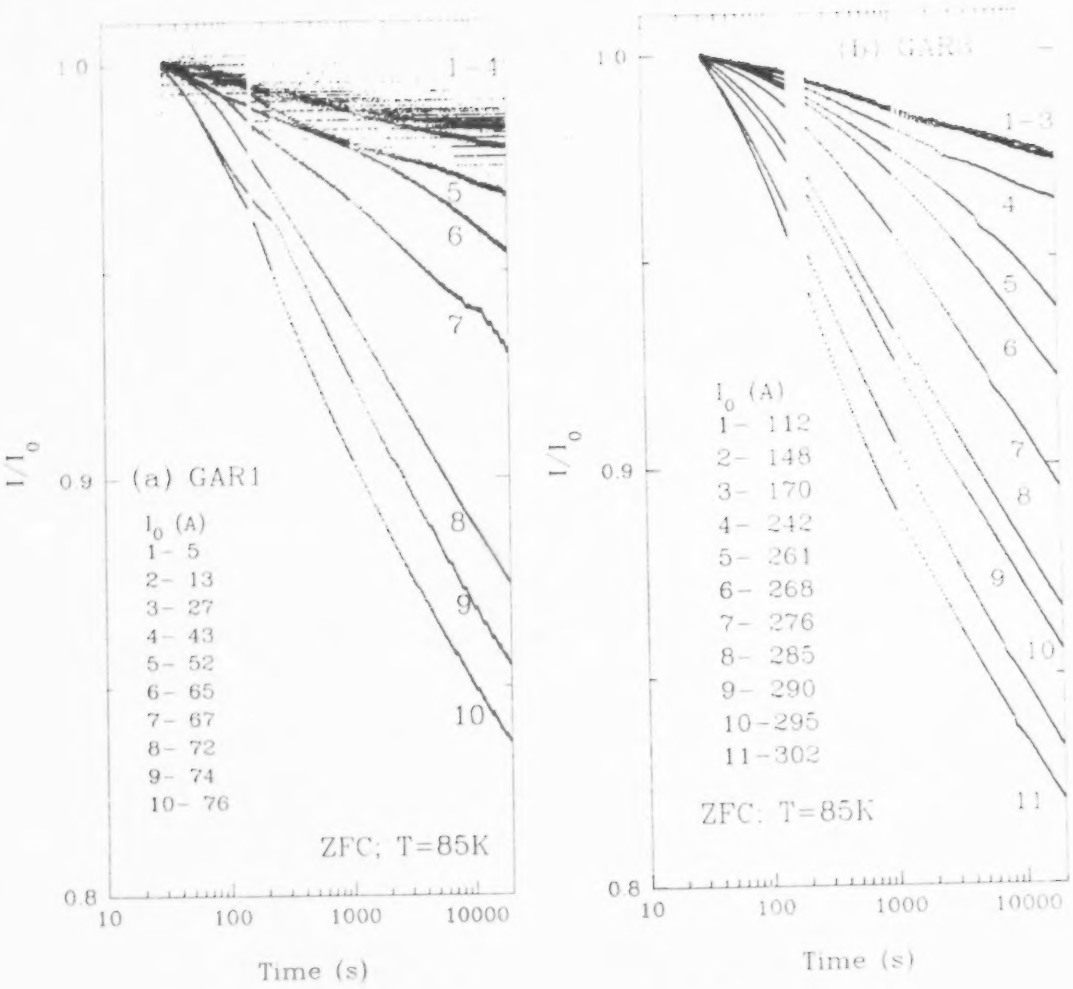

Fig. 17. Dependence of the persistent current normalized to an initial value I_0 in the zero field cooled grain-aligned YBCO rings: (a) GAR1 and (b) GAR3 on time over a range of 30 to 20,000 sec at 85 K. For small I_0 (see curves 1-4 in (a) and 1-3 in (b)) the normalized decay rates are independent of I_0.

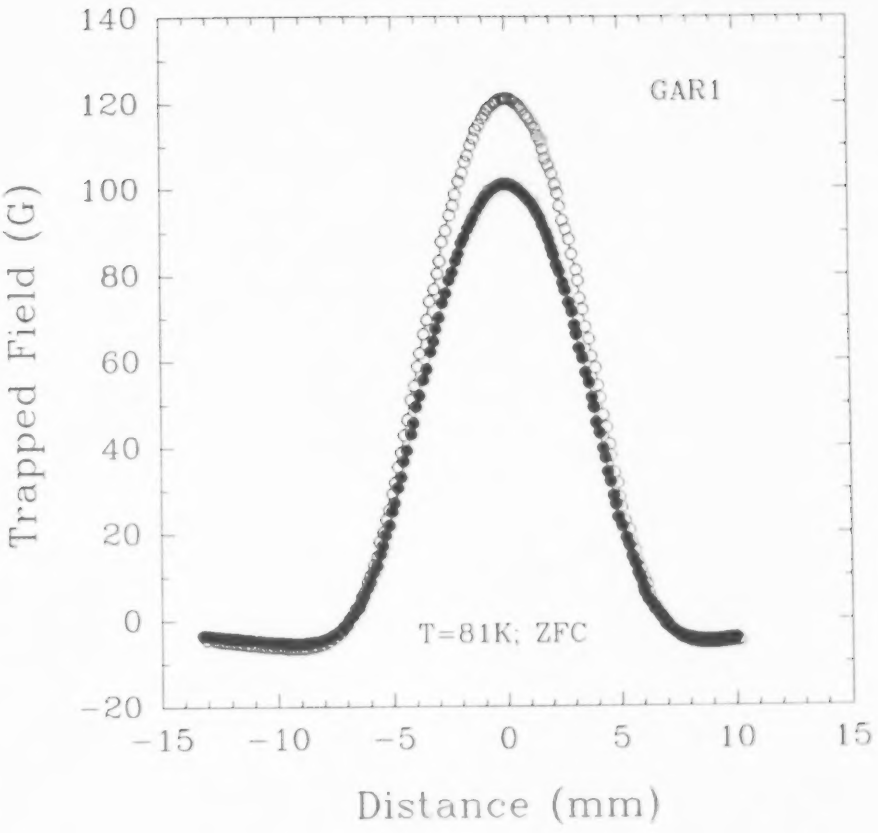

Fig. 18. The Profiles of the max. trapped field due to the persistent current $I_0 \approx I_c$ in the zero field cooled grain-aligned YBCO ring GAR1 at 81 K measured after 30 sec (open circles) and after 20,000 sec (solid circles).

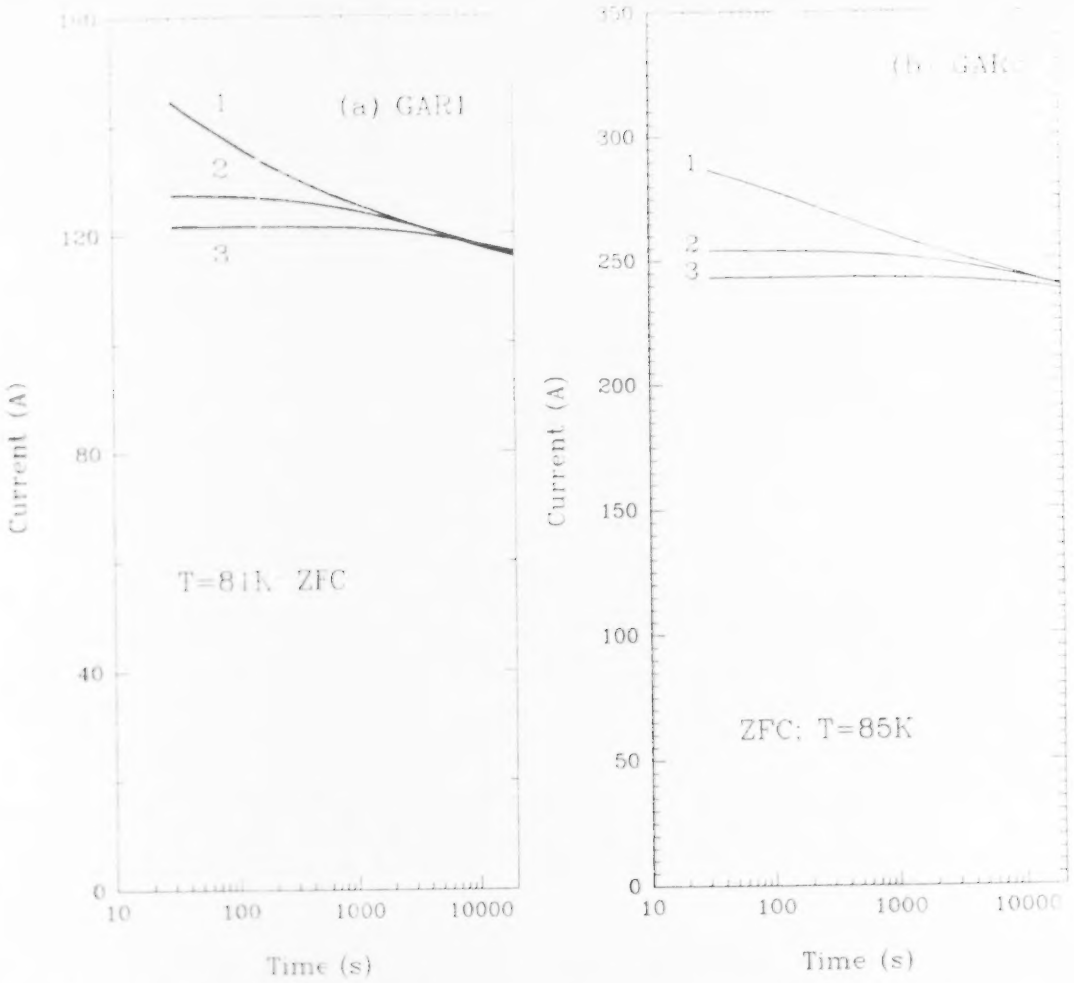

Fig. 19. Relaxation of the persistent current after a flux creep annealing procedure was applied to zero field cooled YBCO grain-aligned rings (a) No. GAR1 at 81 K and (b) No. GAR3 at 85 K. (1) Decay of the persistent current measured from a maximum value I_0^{max} of the current at 81 K (or 85 K). (2) Decay of the persistent current from a reduced value $I<I_0^{max}$ obtained through flux creep annealing procedure by establishing the current I_0^{max} at 81 K (or 85 K for case (b)), warming the sample up to an intermediate temperature of 81.5 K (or 85.5 K for case (b)) followed by cooling down to 81 K (or 85 K for case (b)) and measuring the decay. (3) The same as is (2) except the intermediate temperature is 82 K (or 86 K for case (b)).

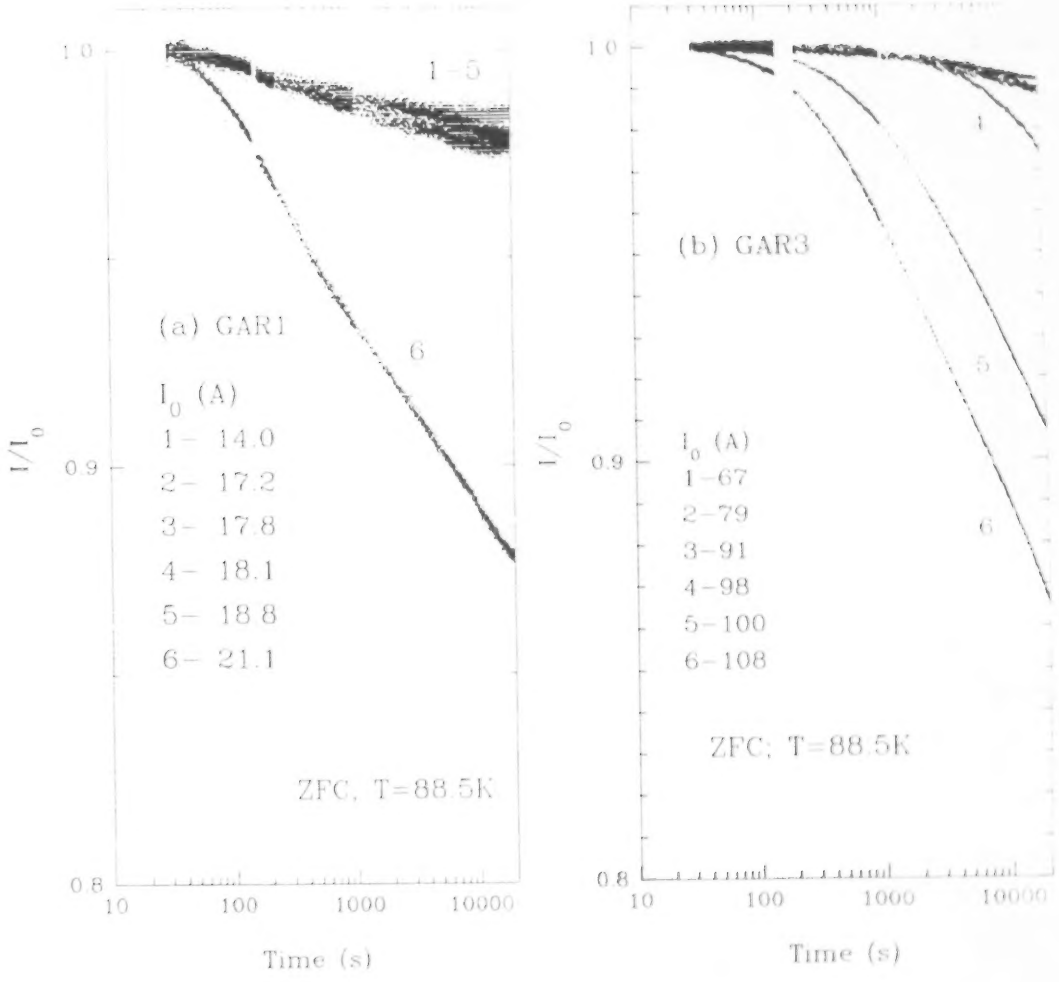

Fig. 20. Dependence of the persistent current normalized to an initial value I_0 on time over a range of 30 to 20,000 sec measured for various values of I_0 at T=88.5 K in the zero field cooled grain-aligned rings (a) No. GAR1 and (b) No. GAR3. At this temperature, the decay is slow for any level of the current $I_0 < I_0^{max}$ (see curves 1-5 in (a) and 1-3 in (b)).

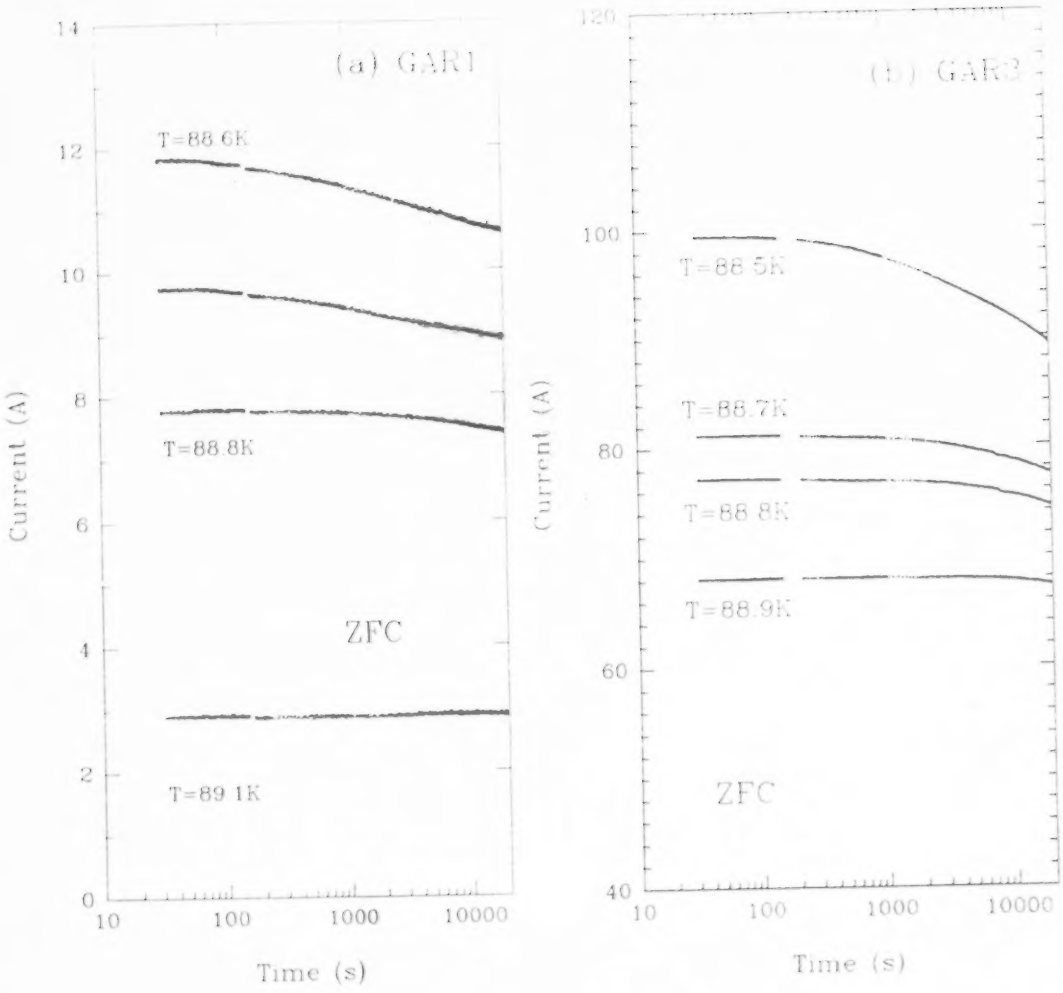

Fig. 21. Dependence of the persistent current on time over a range 30 to 20,000 sec measured from a maximum current I_0^{max} close to I_c for various temperatures close to T_c (a) between 88.6 K and 89.1 K in ring No. GAR1 and (b) between 88.5 K and 88.9 K in ring No. GAR3.

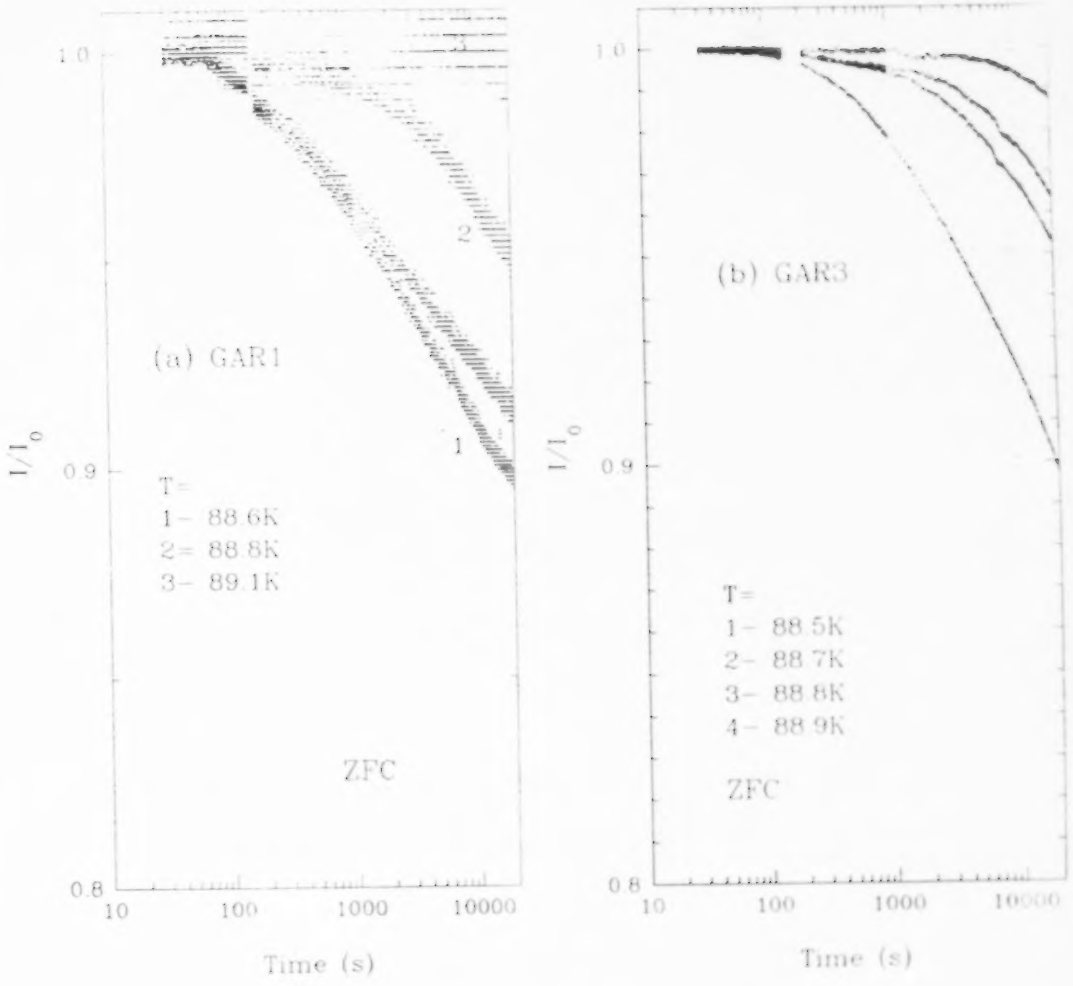

Fig. 22. Dependence of the same persistent currents as in Fig. 21, normalized to the initial values I_0^{max}. For high temperatures the slow initial decays persist longer. The persistent current at 89.1 K in (a) does not show any decay within a noise level of 1%. The noise that appears in this measurement is mainly due to normalizing the current to a small initial value of 3 Amp.

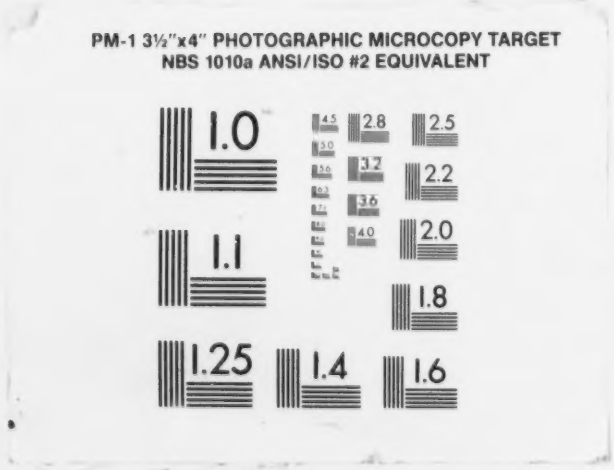
PM-1 3½"x4" PHOTOGRAPHIC MICROCOPY TARGET
NBS 1010a ANSI/ISO #2 EQUIVALENT
1.0
1.1
1.25
1.4
1.6
2.8
2.5
3.2
2.2
3.6
2.0
4.0
1.8

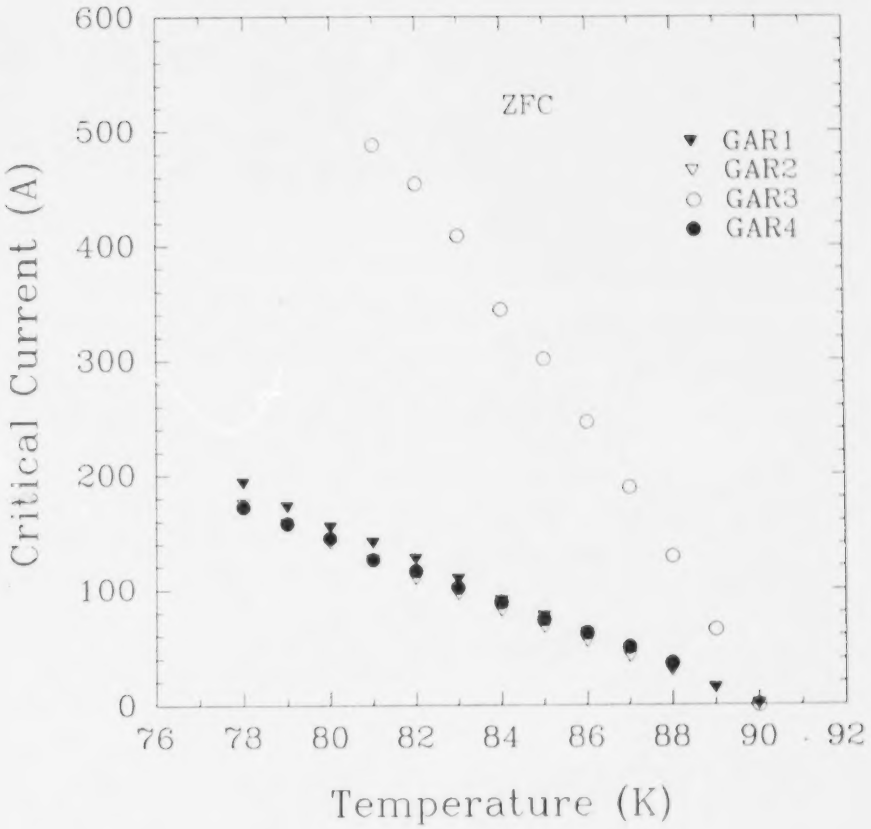

Fig. 23. Dependence of the maximum magnitude of the persistent current I_0^{max} close to I_c on temperature. I_0^{max} was calculated from the saturation value of the trapped field in the zero field cooled grain-aligned YBCO rings GAR1, GAR2, GAR3 and GAR4.

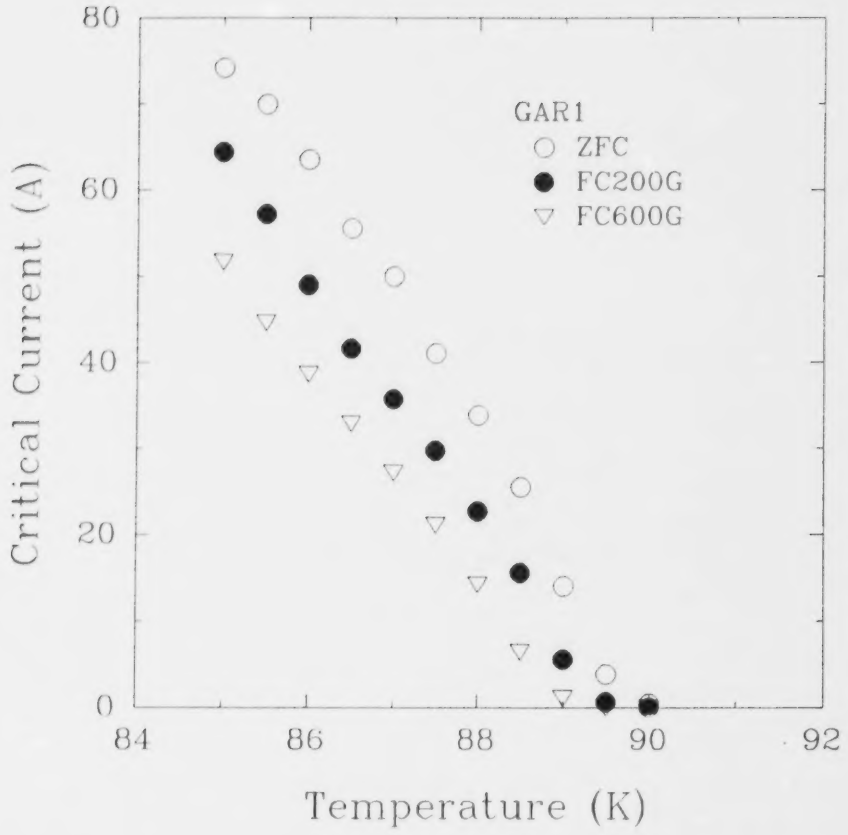

Fig. 24. Dependence of I_0^{max} close to I_c, in the grain-aligned YBCO ring No. GAR1, on temperature over a temperature range from 85 K to 90 K for ZFC and FC cases. Note that the dependence is linear up to 88.5 K. Above this temperature, the dependence deviates from linearity. This is seen for both the ZFC and FC cases.

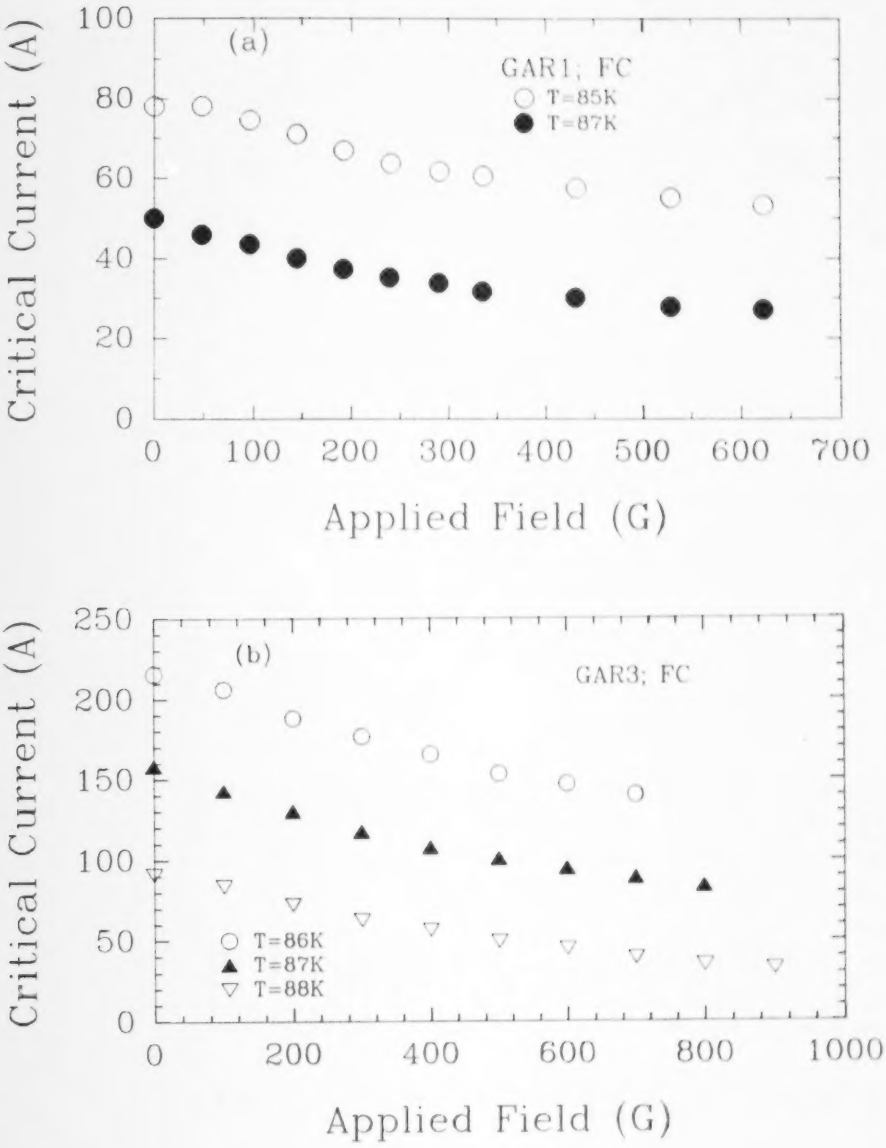

Fig. 25. Dependence of the maximum persistent current on the applied magnetic field: (a) For the grain-aligned ring No. GAR1 measured at 85 K and 87 K. (b) For the grain-aligned ring No. GAR3 measured at 86 K, 87 K and 88 K.

3.2 Experimental results for ceramic YBCO rings:

This section focuses on the behavior of the intergrain critical current in ceramic YBCO, especially its dependence on temperature, magnetic field and time. Four different measurements were performed:

(1) The dependence of the critical current I_c on temperature measured in the zero field cooled rings, i.e. $I_c(T)$ at $H_{app}=0$. These measurements are necessary to identify the type of the intergrain junctions which connect the superconducting grains.

(2) The dependence of the critical current I_c on temperature measured in the field cooled rings at constant applied magnetic fields. This is necessary to understand how the presence of the magnetic fields affects the basic properties of intergrain junctions and consequently the behavior of the transport current.

(3) The dependence of the critical current I_c on the applied magnetic field measured in the field cooled rings at constant temperatures.

(4) The dissipation (time dependence) of the persistent current at various temperatures for the zero field cooled and field cooled rings.

3.2.1 Dependence of I_c on temperature:

Figures 26-28 present the dependence of the I_c on temperature over a range of 60-90 K measured in YBCO ceramic rings for group A which contains three rings of pure YBCO compound (Table 2). In Figure 26, the magnitude of the

critical current is plotted as a function of temperature for ring PCR-A1. The critical current was measured over a temperature range of 60-90 K for zero field cooling (ZFC) and for field cooling (FC) in an applied magnetic field of 20 G. The temperature dependence of I_c for the second ring in group A, PCR-A2, is shown in Figure 27 for the same temperature range for ZFC, FC(20G) and FC(40G) cases. For the third ring in group A, the dependence of the critical current on temperature in the temperature range 60-90 K is shown in Figure 28 for four different cooling conditions: ZFC, FC(10G), FC(20G) and FC(30G). The Hall probe can detect magnetic field generated by the persistent current of magnitude larger than 20 mA. This condition therefore sets the criterion for the "zero resistance" temperature T_c^* of the intergrain junctions, which is less than the transition temperature T_c for the superconducting grains. Applied magnetic fields up to 40 G cause gradual reduction of T_c^*. Table 5 presents the value of $T_c^*(H)$ for three YBCO samples.

Figures 29-33 present the temperature dependence of the critical current I_c for the second group, group B of five samples of YBCO/Ag compounds. The temperature dependence was measured for PCR-B1 in four cases: ZFC, FC(20G), FC(40G) and FC(60G) (Figure 29). For ring PCR-B2 $I_c(T)$ was measured only in the case of ZFC as shown in Figure 30. For ring PCR-B3 $I_c(T)$ was measured in two cases; ZFC and FC(20G) (Figure 31).

YBCO Ring	T_c^* (ZFC) ± 0.5 K	T_c^* (FC) ± 0.5 K
PCR-A1	85.5	84.0 (20G)
PCR-A2	87.0	82.5 (20G) 78.0 (40G)
PCR-A3	87.5	86.5 (10G) 84.5 (20G) 82.5 (30G)

Table 5: Zero resistance temperature and its field dependence for group A of YBCO rings.

In Figure 32 the temperature dependence of I_c for ring PCR-B4 is presented for ZFC, FC(10G), FC(20G) and FC(30G) cases. Figure 33 shows the same results for ring PCR-B5. Table 6 summarizes the results for T_c^* and its reduction in an applied field for various samples of group B.

Ring YBCO/Ag(x%wt)	x	T_c^* (ZFC) ± 0.5 K	T_c^* (FC) ± 0.5 K
PCR-B1	2	87.0	85.0 (20G) 84.5 (40G) 84.0 (60G)
PCR-B2	2	87.0	---
PCR-B3	2	87.0	85.5 (20G)
PCR-B4	4	87.5	85.0 (10G) 81.5 (20G) 79.0 (30G)

PCR-B5	4	87.0	84.0 (10G) 82.0 (20G) 80.0 (30G)

Table 6: Zero resistance temperature and its field dependence for group B YBCO/Ag rings.

Group C, which includes two YBCO/Ag (2% wt) rings with superconducting interfaces, showed a huge reduction in I_c compared to that in similar compounds without interfaces, e.g. as in group B. The temperature dependence of the critical current for rings PCR-C1 and PCR-C2 is shown in Figures 34 and 35. The critical current was measured as a function of temperature over a temperature range 60-90 K for the ZFC, FC(10G) and FC(20G) cases
for both rings. Table 7 gives a summary of the transition temperatures and their corresponding field dependence for group C.

Ring **YBCO/Ag(2%wt)** **+ interfaces**	**T_c^* (ZFC) ±0.5 K**	**T_c^* (FC) ±0.5 K**
PCR-C1	86.5	86.0 (10G) 85.5 (20G)
PCR-C2	86.0	83.0 (10G) 77.0 (20G)

Table 7: Zero resistance temperature and its field dependence for group C (YBCO/Ag + interfaces) rings.

In group D, yttrium was replaced, either partially or completely, by other rare earth elements such as gadolinium, europium and praseodymium. Compounds which contained Gd (PCR-D1) and Eu (PCR-D2) showed an increase in T_c^* compared to those which contained yttrium (PCR-A1 and PCR-A2). These four samples received similar calcining and sintering conditions. On the other hand compounds that contained praseodymium experienced a large decrease in T_c^*. However, in the four rings studied in this group, $I_c(T)$ is linear close to the transition temperature. This behavior is not maintained for FC cases. The above is shown in Figures 36-39 and Table 8.

Ring	T_c^* (ZFC) ±0.5 K	T_c^* (FC) ±0.5 K
PCR-D1 (GBCO)	91.5	89.0 (20G) 87.5 (40G)
PCR-D2 (EBCO)	92.0	88.5 (20G) 88.0 (40G)
PCR-D3 ($(Pr_{.15}Y_{.85})$BCO)	77.5	76.5 (10G)
PCR-D4 ($(Pr_{.2}Y_{.8})$BCO)	72.5	71.0 (10G)

Table 8: Zero resistance temperature and its field dependence for group D rings.

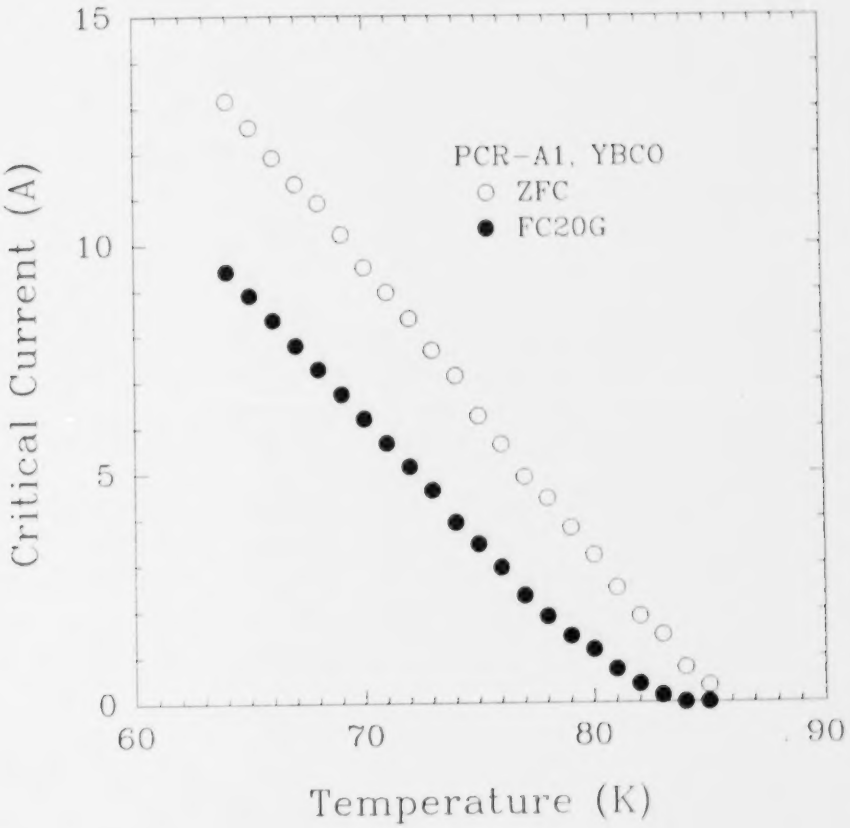

Fig. 26. Dependence of the intergrain critical current I_c in the YBCO ceramic ring PCR-A1 on temperature measured over a range between 64 and 86 K for ZFC and FC(20G) cases.

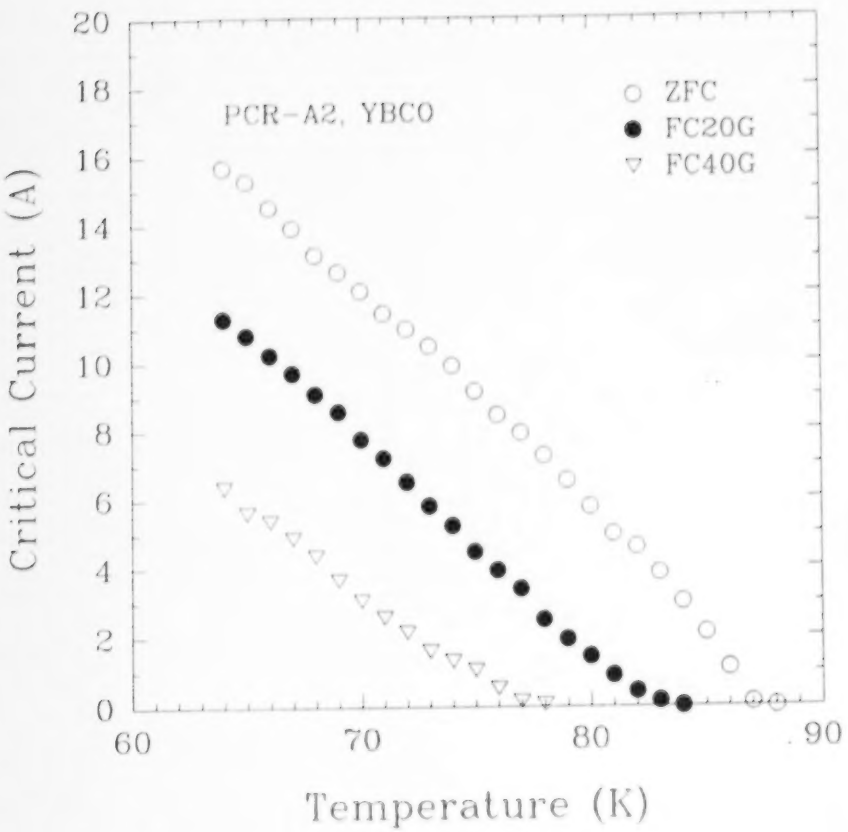

Fig. 27. Dependence of the intergrain critical current I_c in the YBCO ceramic ring PCR-A2 on temperature measured over a range between 64 and 88 K for the ZFC, FC(20G) and FC(40G) cases.

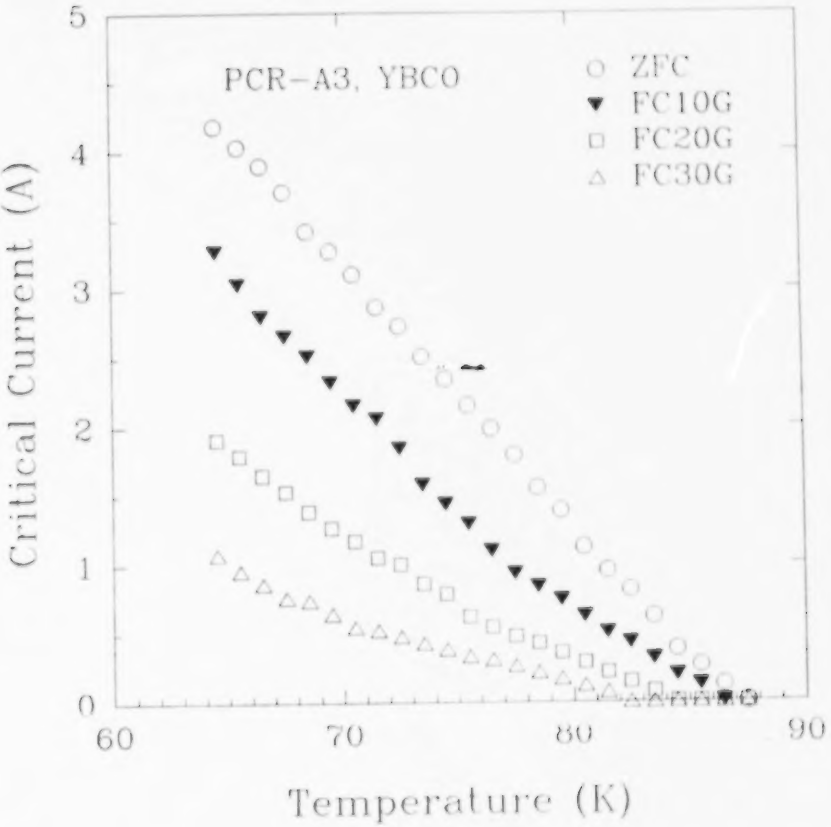

Fig. 28. Dependence of the intergrain critical current I_c in the YBCO ceramic ring PCR-A3 on temperature measured over a range between 64 and 87 K for the ZFC, FC(10G), FC(20G) and FC(30G) cases.

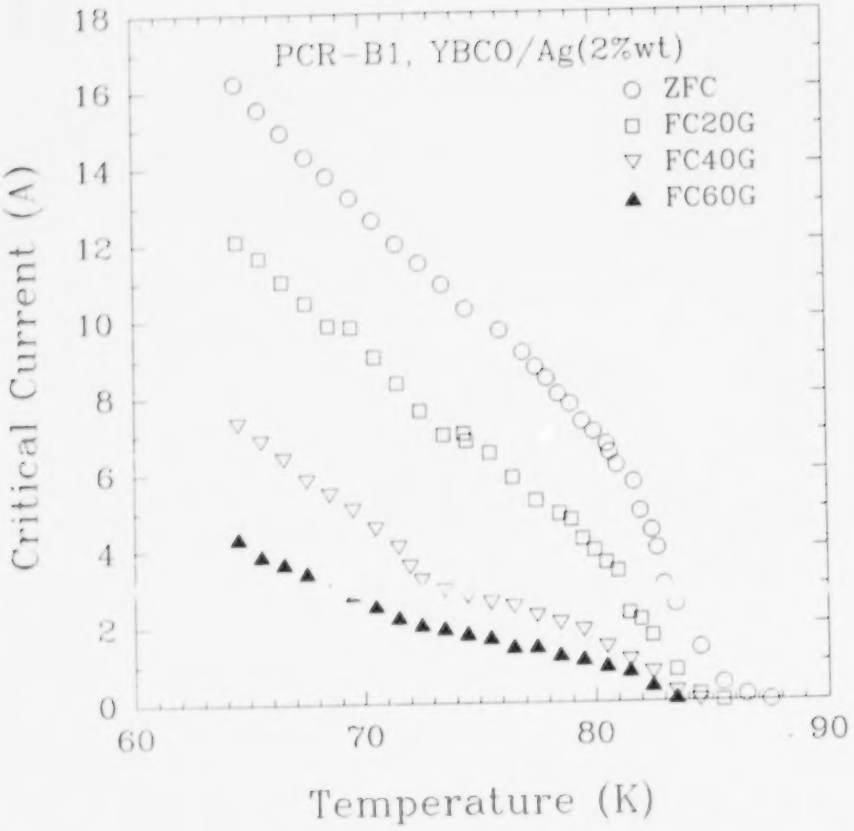

Fig. 29. Dependence of the intergrain critical current I_c in the YBCO/Ag(2%wt.) ceramic ring PCR-B1 on temperature measured over a range between 64 and 87 K for the ZFC, FC(20G), FC(40G) and FC(60G) cases.

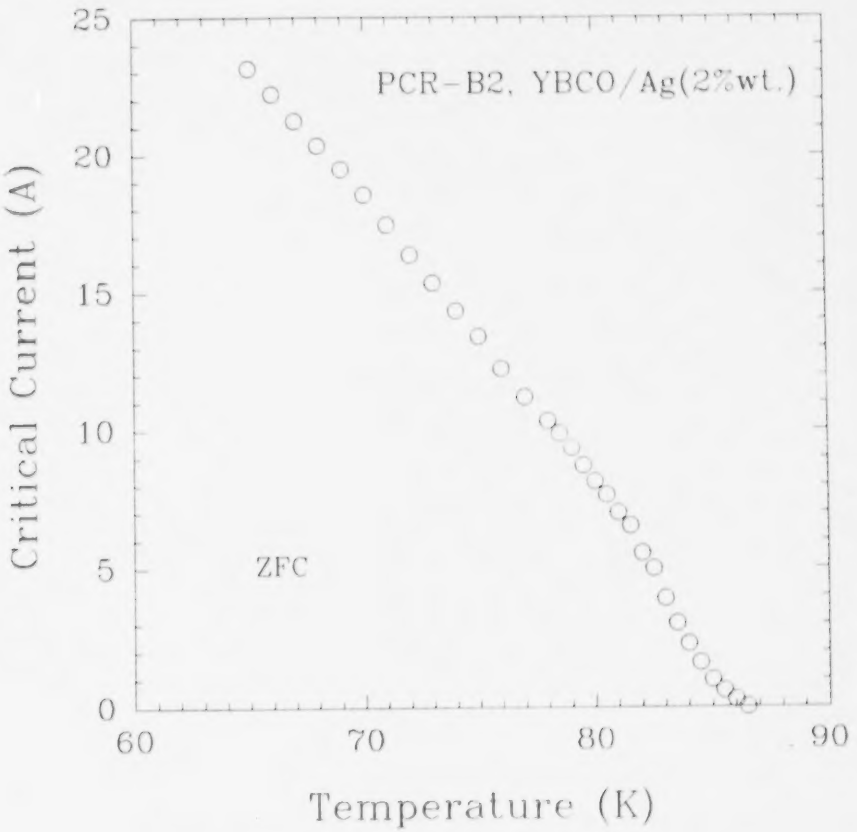

Fig. 30. Dependence of the intergrain critical current I_c in the YBCO/Ag(2%wt.) ceramic ring PCR-B2 on temperature measured over a range between 64 and 86 K for the ZFC case.

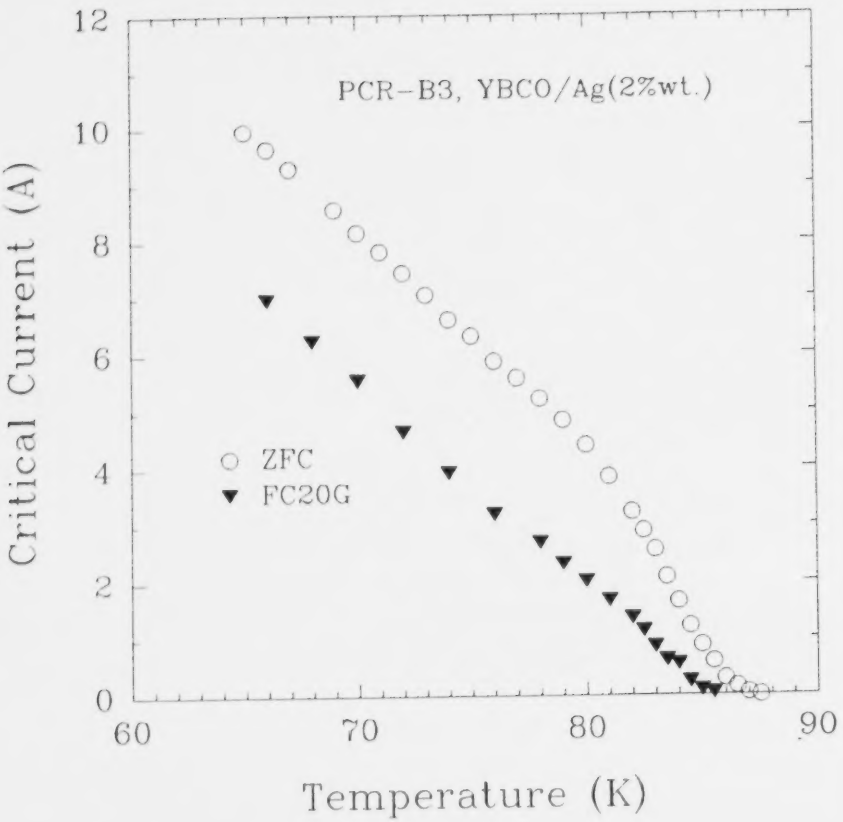

Fig. 31. Dependence of the intergrain critical current I_c in the YBCO/Ag(2%wt.) ceramic ring PCR-B3 on temperature measured over a range between 64 and 88 K for the ZFC and FC(20G) cases.

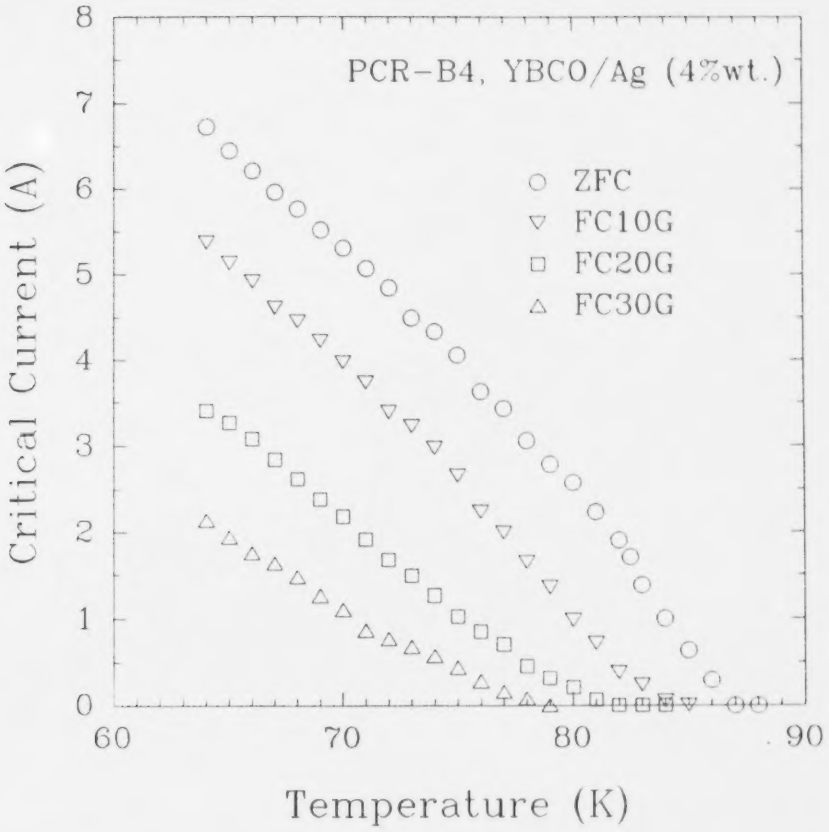

Fig. 32. Dependence of the intergrain critical current I_c in the YBCO/Ag(4%wt.) ceramic ring PCR-B4 on temperature measured over a range between 64 and 88 K for the ZFC, FC(10G), FC(20G) and FC(30G) cases.

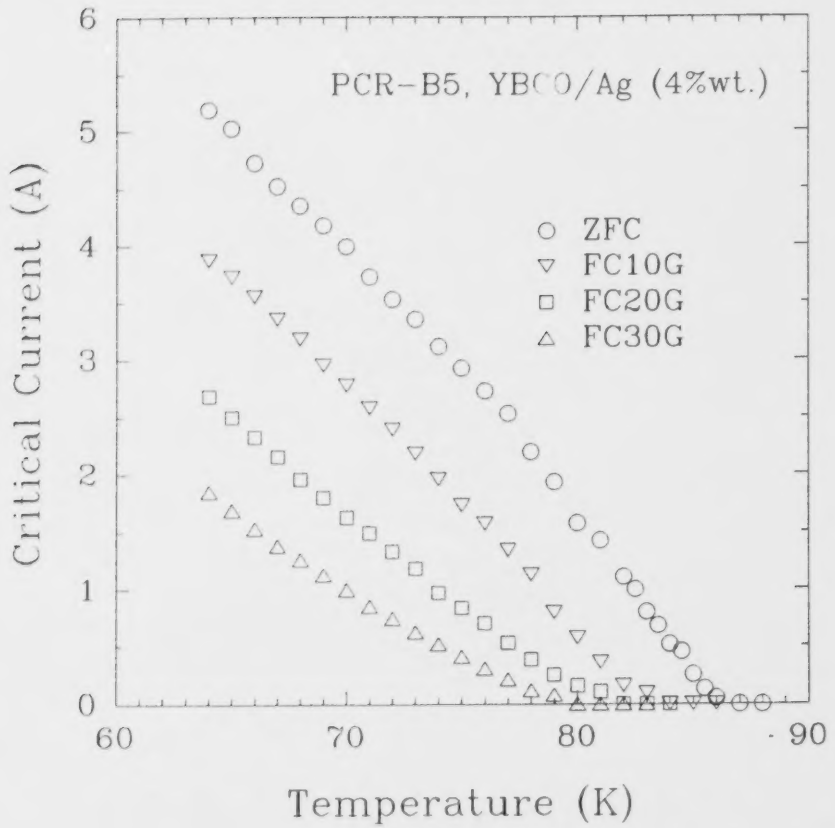

Fig. 33. Dependence of the intergrain critical current I_c in the YBCO/Ag(4%wt.) ceramic ring PCR-B5 on temperature measured over a range between 64 and 88 K for the ZFC, FC(10G), FC(20G) and FC(30G) cases.

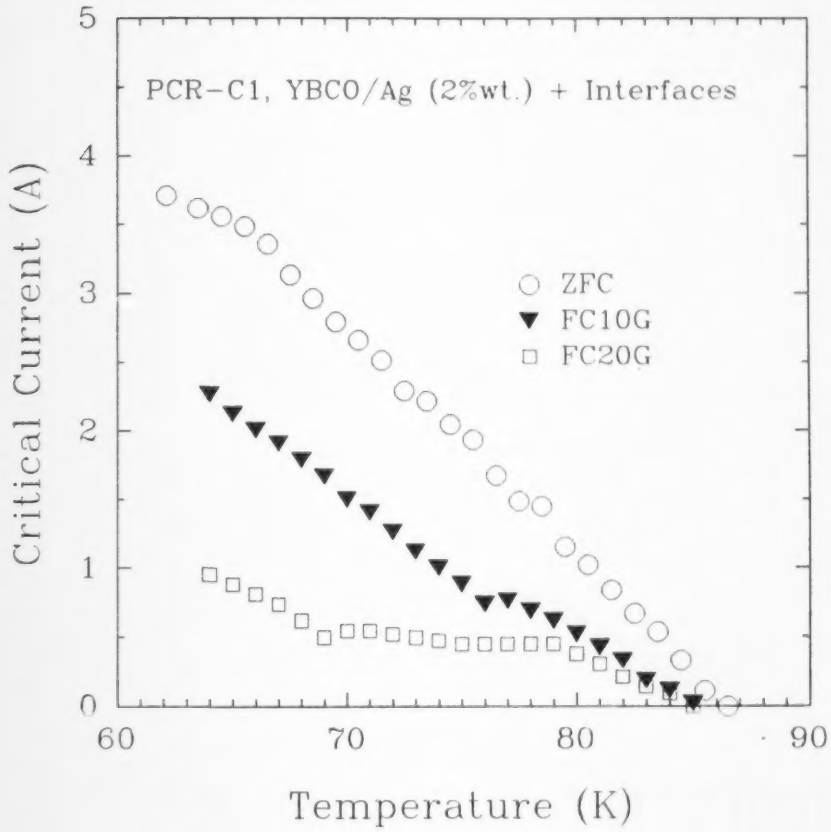

Fig. 34. Dependence of the intergrain critical current I_c in the YBCO/Ag(2%wt. with interfaces) ceramic ring PCR-C1 on temperature measured over a range between 64 and 87 K for the ZFC, FC(10G) and FC(20G) cases.

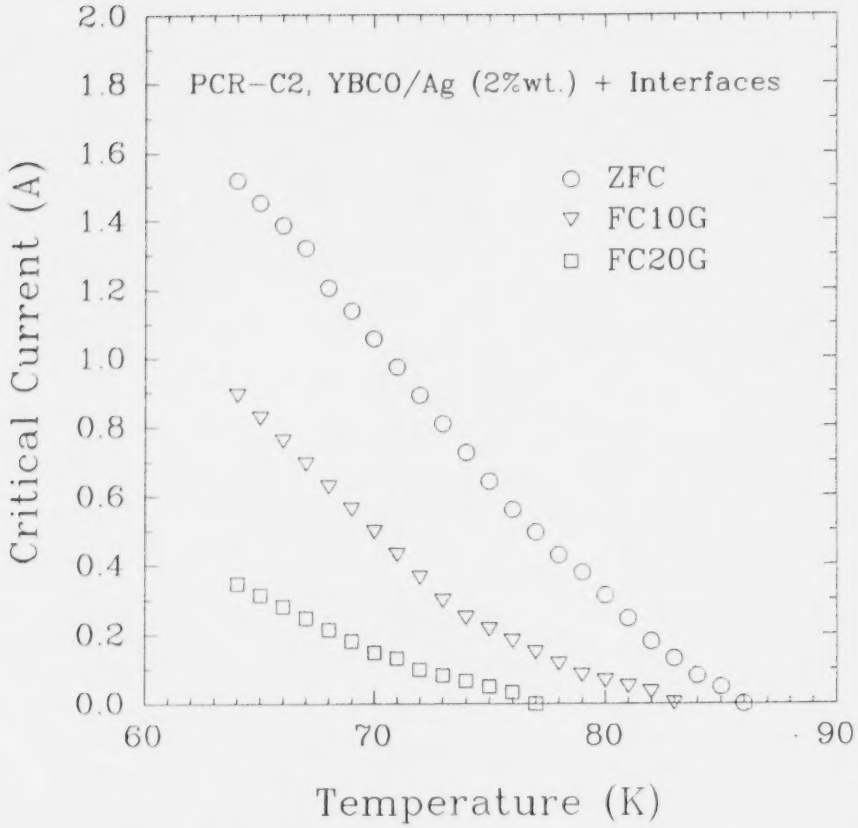

Fig. 35. Dependence of the intergrain critical current I_c in the YBCO/Ag(2%wt. with interfaces) ceramic ring PCR-C2 on temperature measured over a range between 64 and 87 K for the ZFC, FC(10G) and FC(20G) cases.

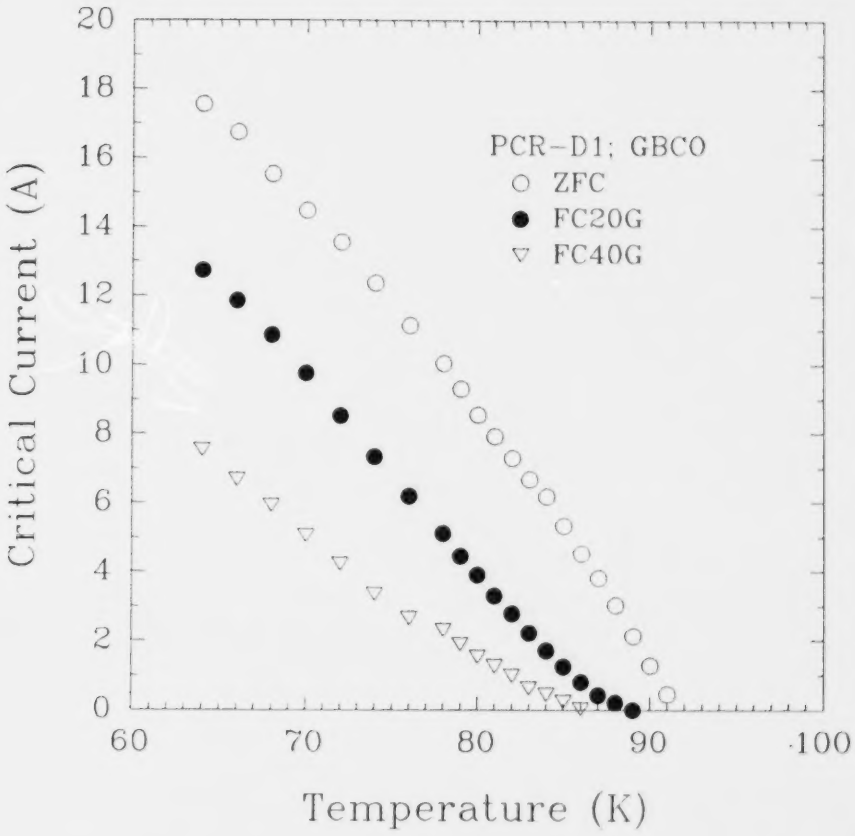

Fig. 36. Dependence of the intergrain critical current I_c in the GBCO ceramic ring PCR-D1 on temperature measured over a range between 64 and 94 K for the ZFC, FC(20G) and FC(40G) cases.

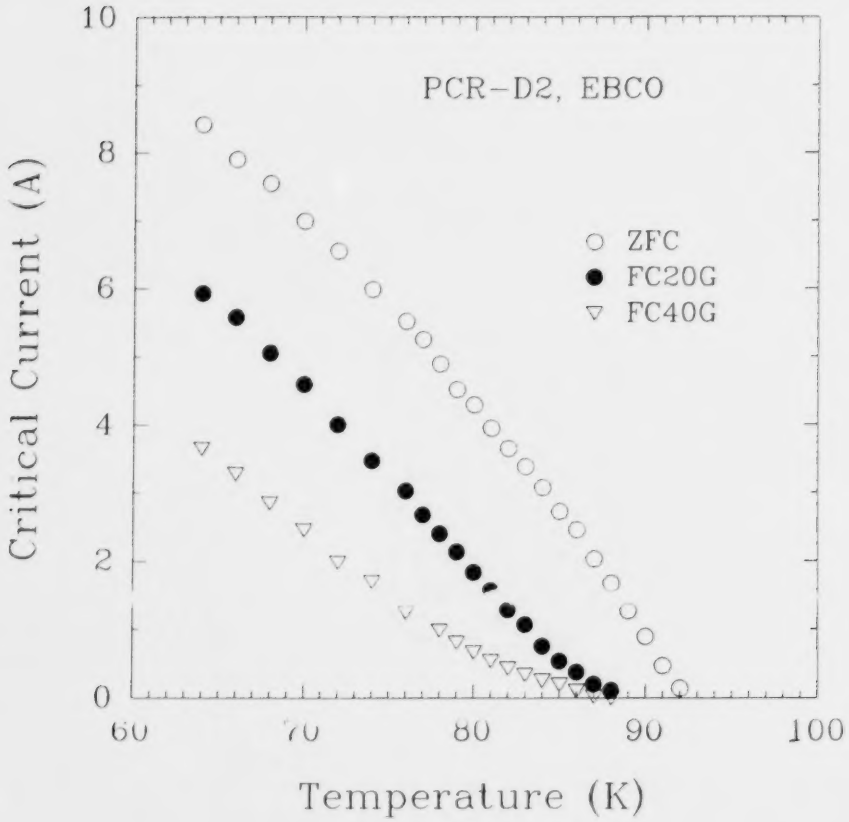

Fig. 37. Dependence of the intergrain critical current I_c in the EBCO ceramic ring PCR-D2 on temperature measured over a range between 64 and 94 K for the ZFC, FC(20G) and FC(40G) cases.

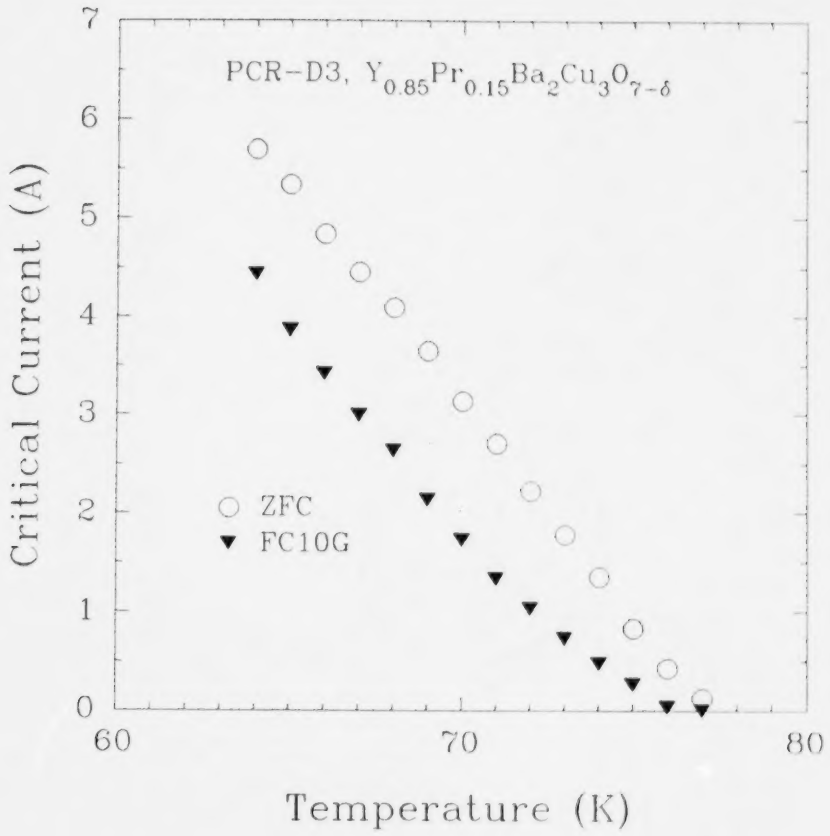

Fig. 38. Dependence of the intergrain critical current I_c in the $(Pr_{0.15}Y_{0.85})Ba_2Cu_3O_{7-\delta}$ ceramic ring PCR-D3 on temperature measured over a range between 64 and 78 K for the ZFC and FC(10G) cases.

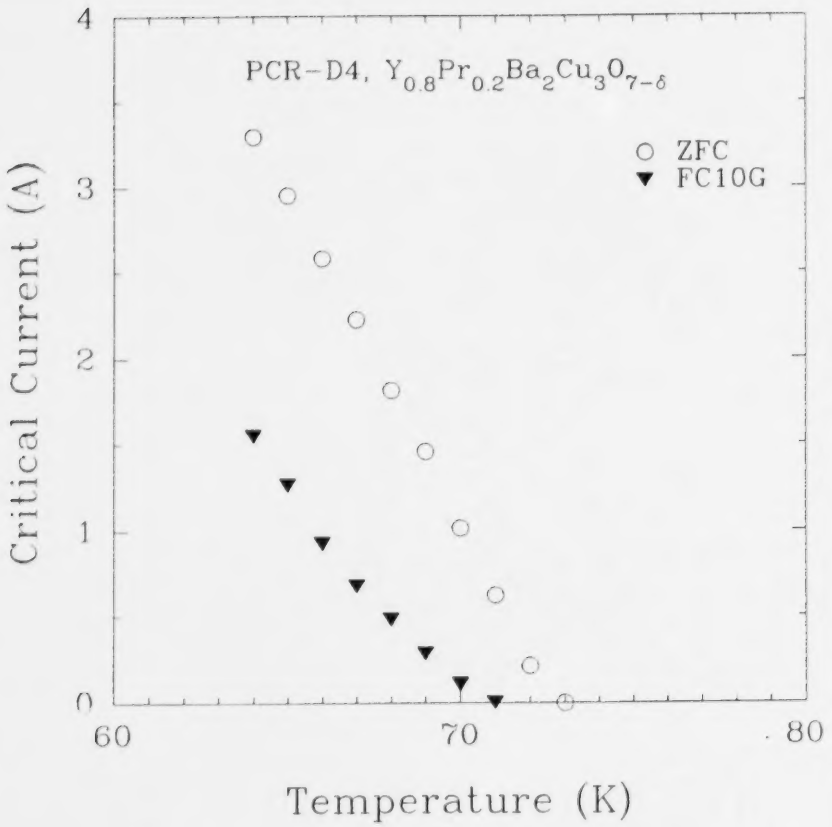

Fig. 39. Dependence of the intergrain critical current I_c in the $(Pr_{0.20}Y_{0.80})Ba_2Cu_3O_{7-\delta}$ ceramic ring PCR-D4 on temperature measured over a range between 64 and 72 K for the ZFC and FC(10G) cases.

3.2.2 Dependence of I_c on the magnetic field:

The dependence of the critical current I_c on magnetic fields up to 80 G was measured in YBCO (PCR-A3) and YBCO/Ag(2%wt.) (PCR-B1) rings at various temperatures between 60 and 90 K. The results are presented in Figures 40 and 41. Strong suppression of the critical current with magnetic field can be seen at low magnetic fields. At fields higher than a certain value H^*, I_c approaches a constant value. H^* increases if the temperature of the sample is reduced. This behavior is observed as a general trend at temperatures about 5-10 K below T_c^* in the YBCO and YBCO/Ag rings. However, at temperatures close to T_c^* intergrain transport current in those rings is completely suppressed by magnetic fields of the order of 20-60 G.

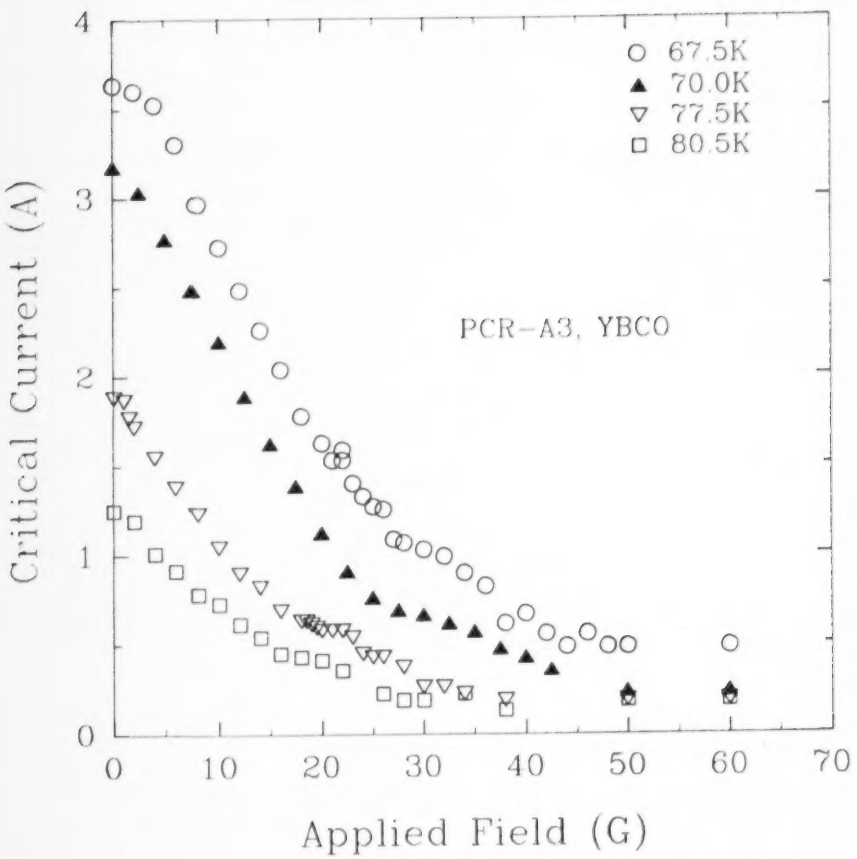

Fig. 40. Dependence of the intergrain critical current I_c on magnetic field up to 60 G for the YBCO ceramic ring PCR-A3 measured at temperatures of 67.5, 70.0, 77.5 and 80.5 K. Note the sin(H)/H behavior of $I_c(H)$ at low fields and a saturation of I_c at magnetic fields above 40 G.

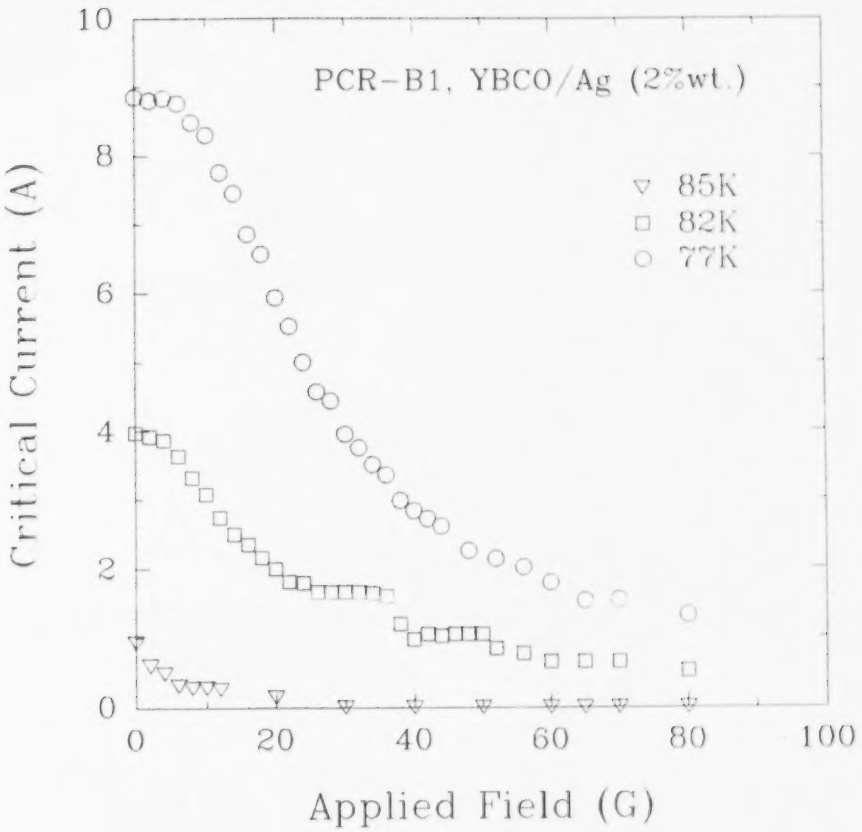

Fig. 41. Dependence of the intergrain critical current I_c on magnetic field up to 80 G for the YBCO/Ag(2%wt.) ceramic ring PCR-B1 measured at temperatures of 77.0, 82.0 and 85.0 K. The saturation of $I_c(H)$ occurs at magnetic fields above 60 G.

3.2.3. Dissipation of the persistent current:

The dependence of the persistent current flowing in ceramic rings on time was measured over a time scale up to 1000 sec at constant temperature and applied magnetic field. The decay phenomena did not happen in all samples and this classifies the rings into two major categories: the first includes eight rings in which the persistent current decays with time due to the motion of the flux lines and the second one includes the remaining six rings in which the magnitude of the current does not change with time. The Hall probe could not detect changes in the current less than 10 mA/decade and this sets the decay criterion in this experiment. The two categories are classified in Table 9.

Group	Dissipation	
	Yes	No
A	PCR-A1 (YBCO) PCR-A2 (YBCO)	PCR-A3 (YBCO)
B	PCR-B1 (YBCO/Ag 2%wt.) PCR-B2 (YBCO/Ag 2%wt.) PCR-B3 (YBCO/Ag 2%wt.)	PCR-B4 (YBCO/Ag 4%wt.) PCR-B5 (YBCO/Ag 4%wt.)
C		PCR-C1 (YBCO/Ag 2%wt.) +Interfaces PCR-C2 (YBCO/Ag 2%wt.) +Interfaces
D	PCR-D1 (GBCO) PCR-D3 $(Pr_{.15}Y_{.85})Ba_2Cu_3O_{7-\delta}$ PCR-D4 $(Pr_{.2}Y_{.8})Ba_2Cu_3O_{7-\delta}$	PCR-D2 (EBCO)

Table 9: Classification of the ceramic rings in different groups according to the dissipation phenomena.

The decay of the persistent current I(t) close to the critical current I_c was measured in the zero field cooled and field cooled samples for up to 1000 sec. It should be noted that the corresponding measurements, I(t), for grain-aligned YBCO rings were performed for time range up to 20,000 sec for currents I close to I_c. In the case of grain-aligned YBCO samples the current exhibits a transient nonlogarithmic decay for times up to 1000 sec which converges to a steady-state logarithmic one for times longer than 1000 sec. However, in the case of ceramic YBCO rings, the transient to a steady-state logarithmic regime was not observed and the current decays logarithmically with time over the entire waiting time range (up to 20,000 sec). This is shown in Figure 42 which presents the decay of the critical current in ring PCR-B2 (YBCO/Ag 2%wt.) measured at T=79 K over a time range between 10 sec and 10,000 sec. *The logarithmic behavior dominates the decay process and this behavior is characteristic for ceramic samples*. The dependence of the normalized decay rates, $S=(1/I_c)(dI/d\ln(t))$, on temperature for the eight rings is shown in Figures 43-50 for both ZFC and FC cases. In general, decay rates increase with increasing temperature of the sample and reach high values close to T_c^* for both ZFC and FC cases. The persistent current regains its original value $I_c(T)$ if additional magnetic flux was supplied into the ring's central hole by applying the original external magnetic field to the ring and subsequently reducing its magnitude to zero. This

shows that the value of the critical current in a specific ring is reproducible by applying the same magnetic field and that the cause of the decay of the persistent current is the creep of magnetic flux lines through the ring's bulk.

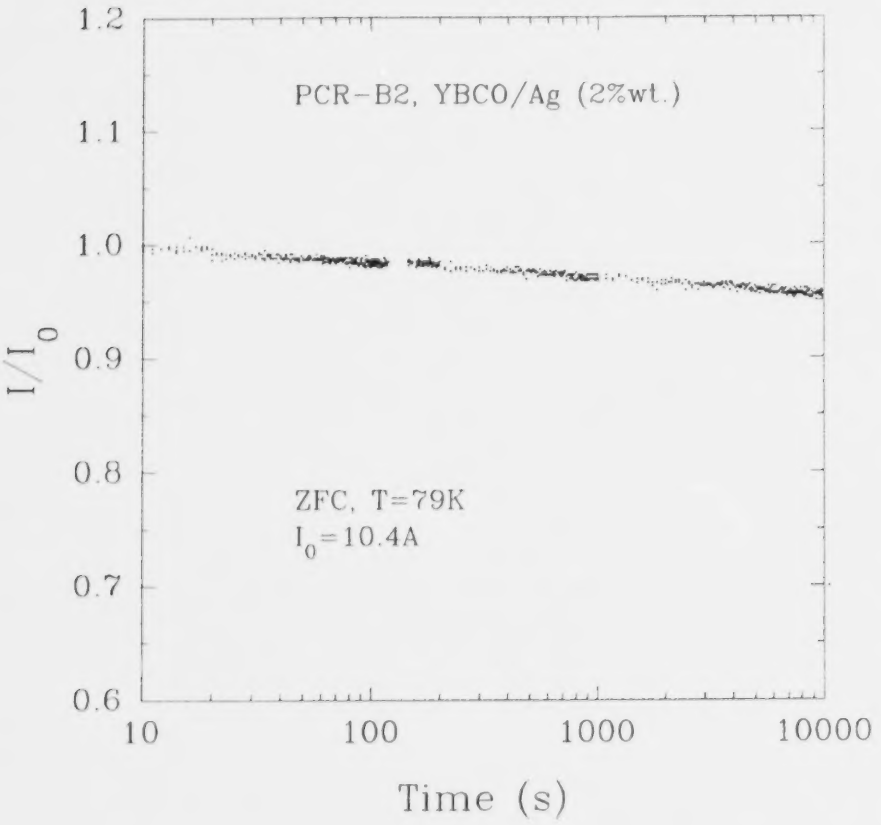

Fig. 42. Dependence of the persistent current normalized to an initial value $I_0 \sim I_c$ on time measured in ceramic YBCO/Ag (2%wt.) ring PCR-B2 at T=79 K for the ZFC case over a time range 10-10,000 sec. Logarithmic decay of the current starts at t=10 sec and persists for the entire range up to 10,000 sec.

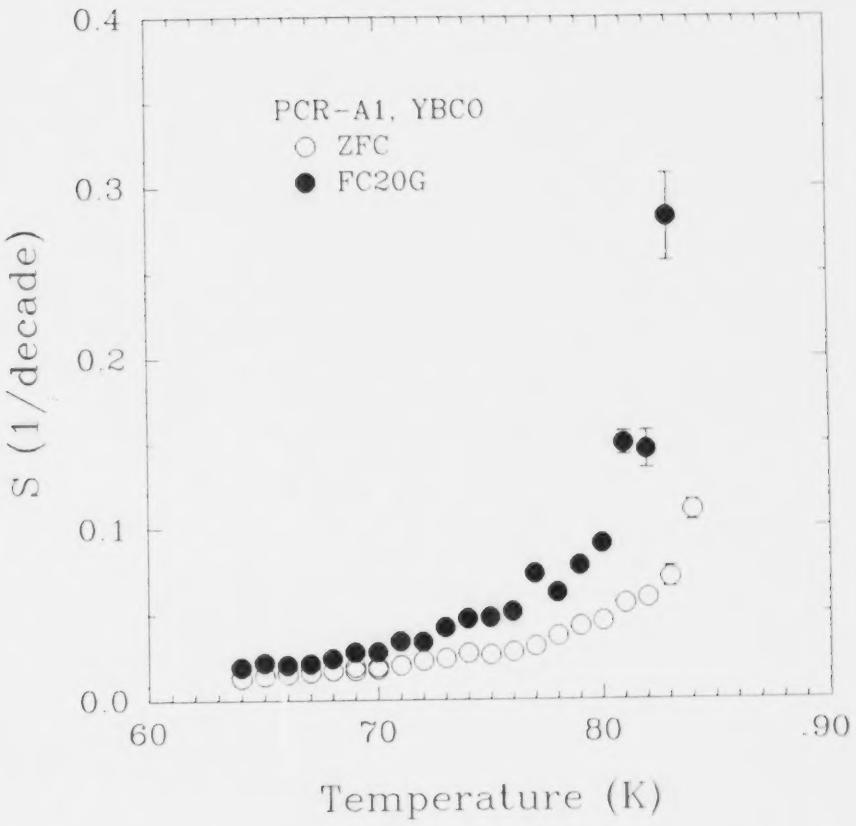

Fig. 43. Dependence of the persistent current decay rates on temperature measured in YBCO ceramic ring PCR-A1 for the ZFC and FC(20G) cases.

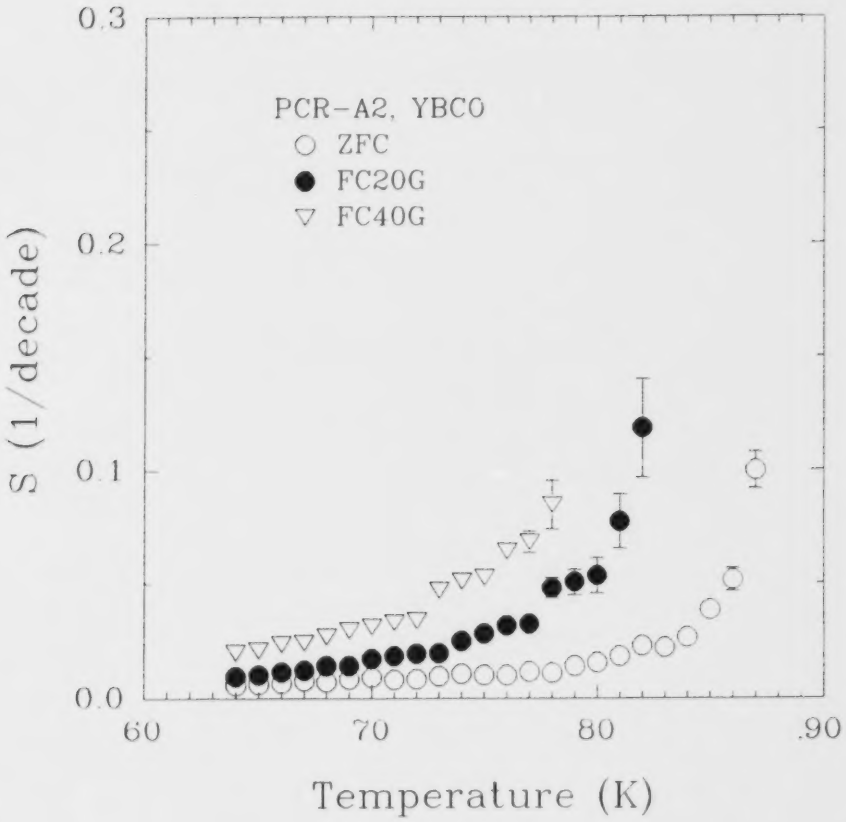

Fig. 44. Dependence of the persistent current decay rates on temperature measured in YBCO ceramic ring PCR-A2 for the ZFC, FC(20G) and FC(40G) cases.

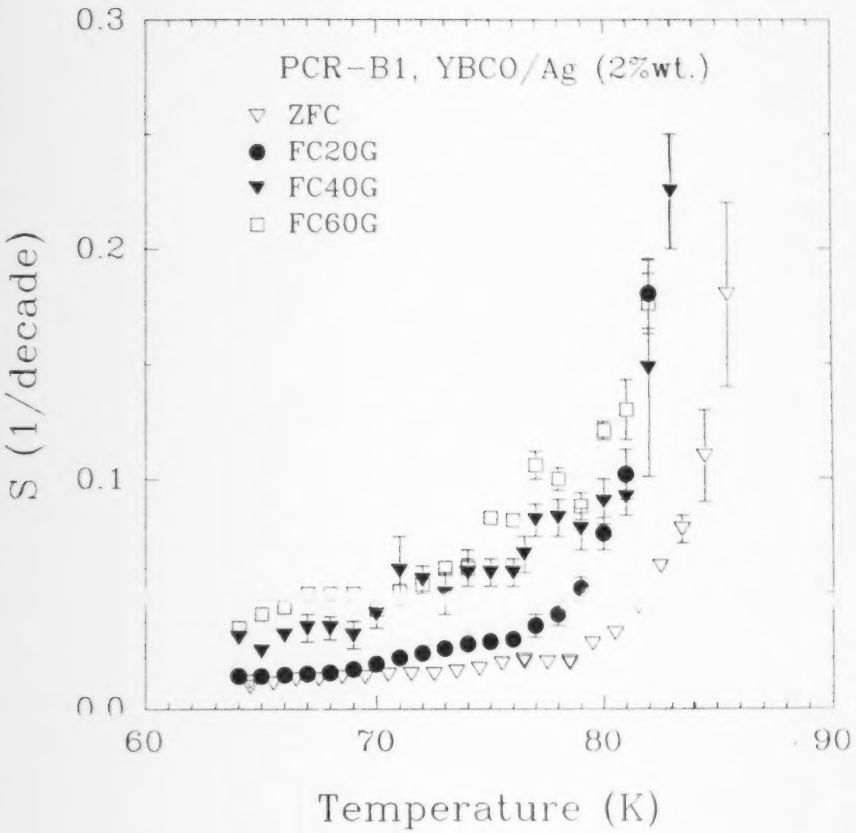

Fig. 45. Dependence of the persistent current decay rates on temperature measured in YBCO/Ag (2%wt.) ceramic ring PCR-B1 for the ZFC, FC(20G), FC(40G) and FC(60G) cases.

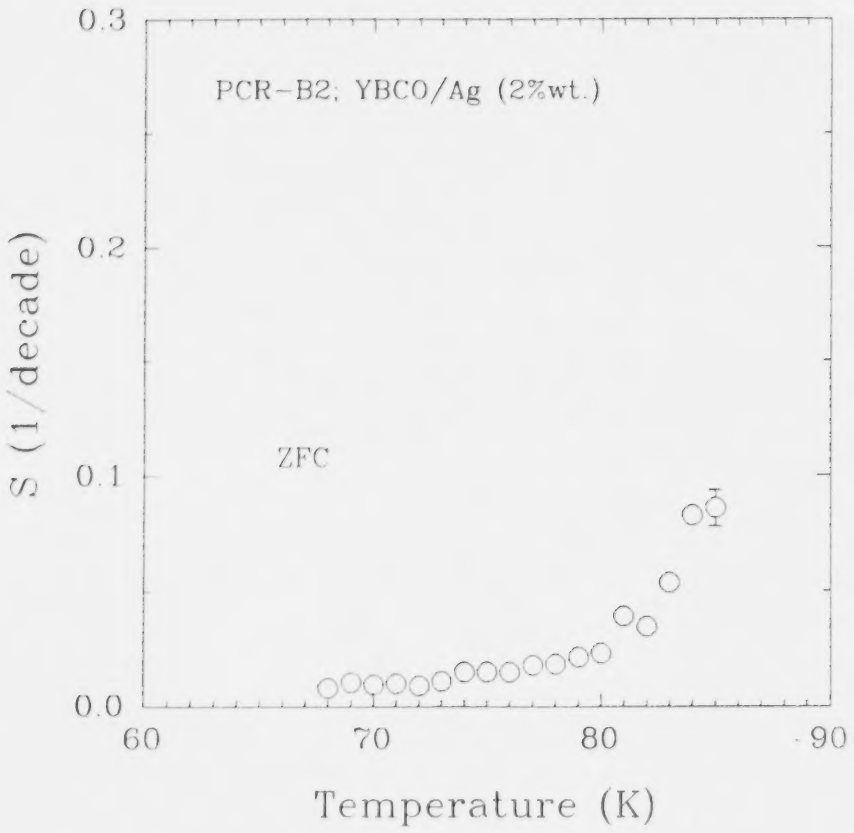

Fig. 46. Dependence of the persistent current decay rates on temperature measured in YBCO/Ag (2%wt.) ceramic ring PCR-B2 for the ZFC case.

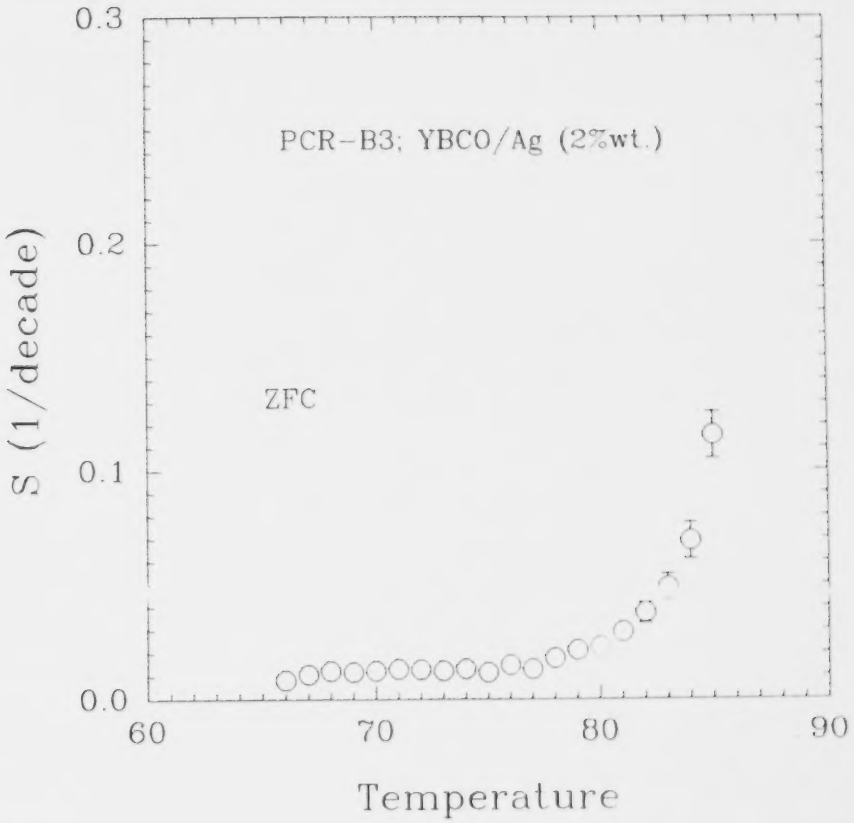

Fig. 47. Dependence of the persistent current decay rates on temperature measured in YBCO/Ag (2%wt.) ceramic ring PCR-B3 for the ZFC case.

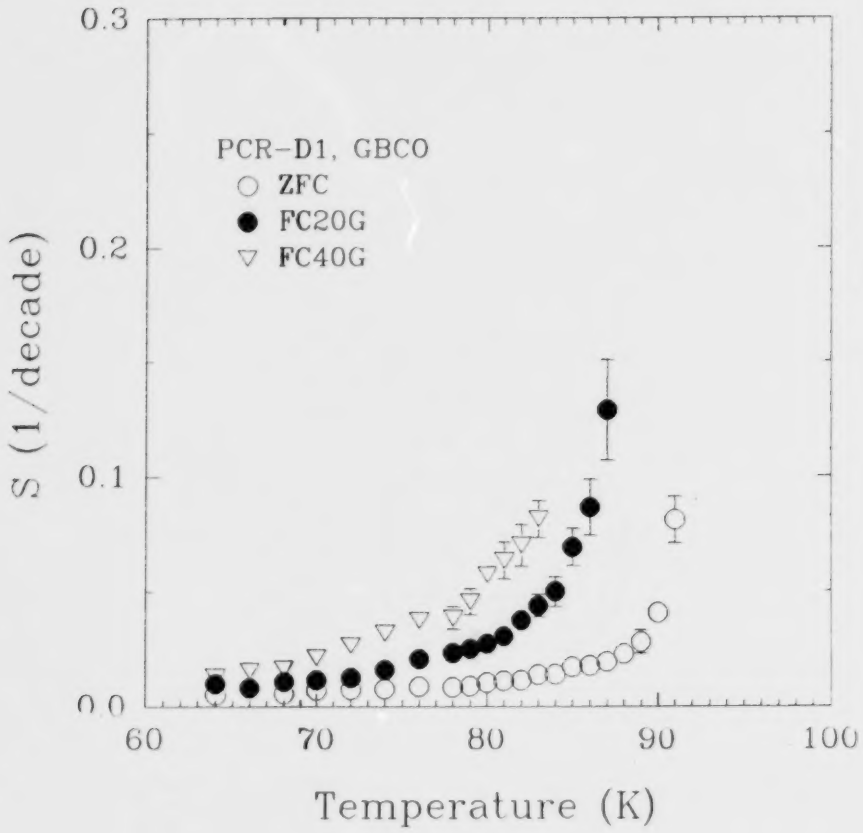

Fig. 48. Dependence of the persistent current decay rates on temperature measured in GBCO ceramic ring PCR-D1 for the ZFC, FC(20G) and FC(40G) cases.

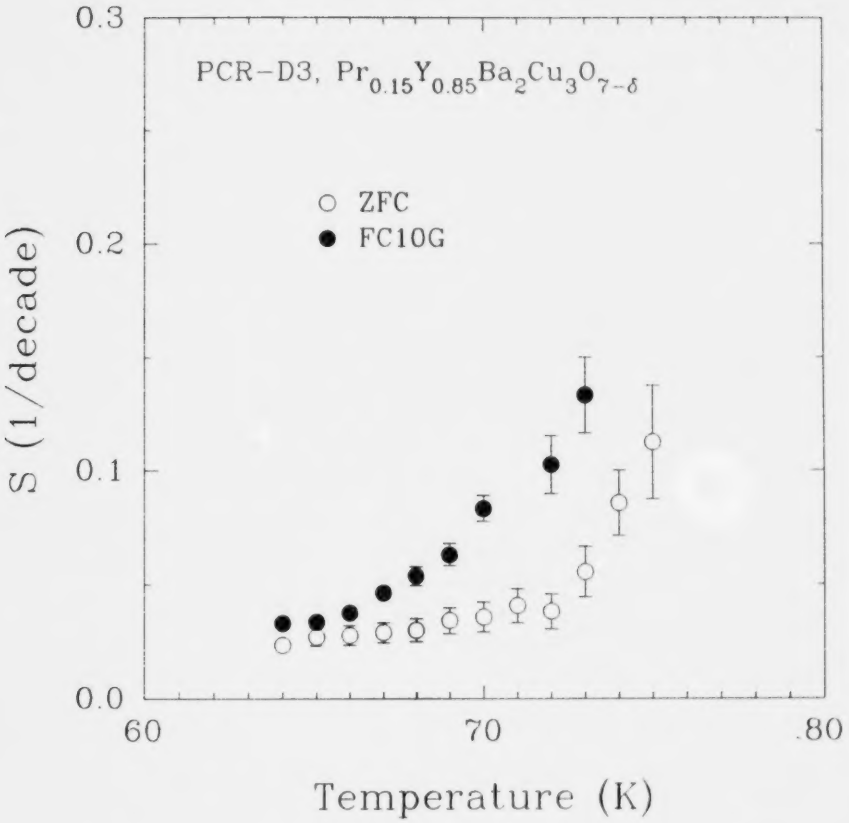

Fig. 49. Dependence of the persistent current decay rates on temperature measured in $(Pr_{.15}Y_{.85})Ba_2Cu_3O_{7-\delta}$ ceramic ring PCR-D3 for the ZFC and FC(10G) cases.

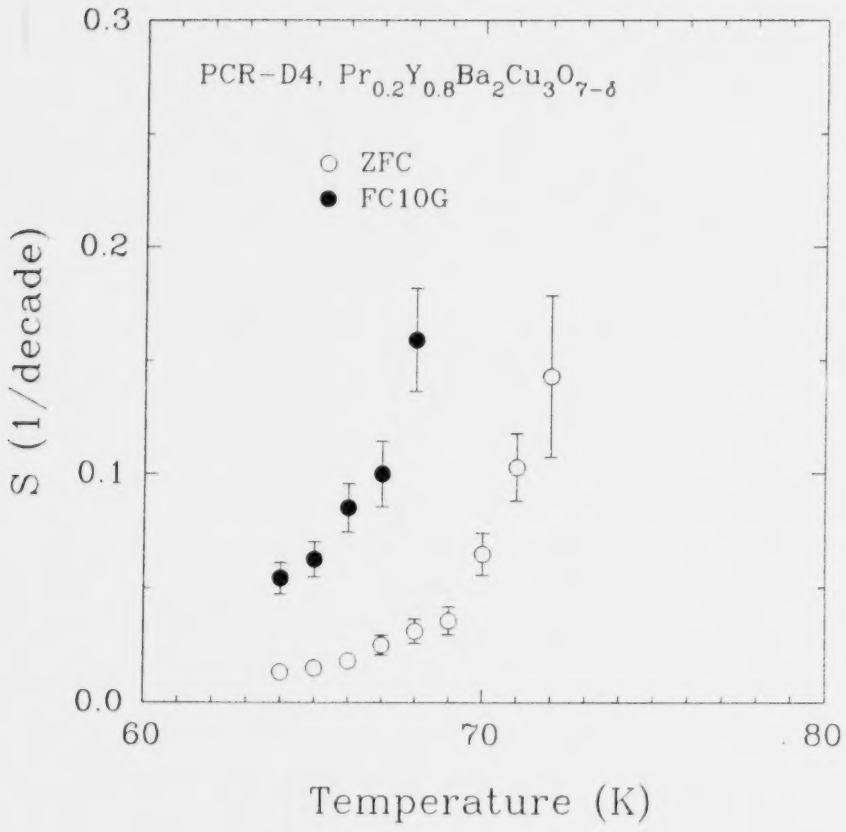

Fig. 50. Dependence of the persistent current decay rates on temperature measured in $(Pr_{.2}Y_{.8})Ba_2Cu_3O_{7-\delta}$ ceramic ring PCR-D4 for the ZFC and FC(10G) cases.

Chapter IV

Discussion

4.1 Grain-aligned YBCO rings:

The magnitude of the persistent supercurrent circulating in a ring shaped grain-aligned YBCO sample should remain unchanged in the absence of resistance along its path. The experimental observations presented in Figures 14 and 15 show the opposite. There is a considerable decay of the magnitude of the supercurrent, up to 20% of its initial value during the first 20,000 sec. This suggests that energy has been drained out of the current loop. This energy loss may be explained as follows: while trying to establish the persistent current in the zero field cooled ring shaped sample by applying an external magnetic field and reducing it to zero, some of the magnetic flux lines which cross the ring's bulk from outside into the inner hole are trapped in the bulk in the form of magnetic vortices. The magnetic vortex lines are pinned in the bulk and prevented from moving by the pinning potentials. However, two factors disturb this stable configuration. These factors are: the relatively high operating temperature which provides high thermal activation for the flux lines and the transport current which tends to distort the pinning potential by exerting the Lorentz driving force on the magnetic vortex lines. This creates a metastable situation and encourages the vortices to hop from one pinning site to another. The vortex motion dissipates energy which has to be compensated for by an

external source. The only available source in this case is the persistent transport current. Therefore, the energy lost during the motion of the magnetic vortices shows up as a decay of the persistent current. Since the nature of the magnetic vortices plays an important role in flux dynamics, it is important to ask what kind of magnetic vortices are involved in the current dissipation process. It is believed that in conventional type-II superconductors two types of magnetic vortices can exist; Abrikosov and Josephson vortices. These classical vortices have often cylindrical geometry and a length comparable to the sample dimensions. An Abrikosov vortex has a core of radius ξ, the coherence length. The Ginzburg-Landau order parameter Ψ is zero at the center of the vortex and approaches its equilibrium value at distances greater than ξ from the axis of the vortex core. Strong persistent currents flow around the core and drop to zero over a distance λ, the penetration depth. These currents screen the magnetic field directed along the axis of the vortex up to the same distance λ.

On the other hand a Josephson vortex does not have a core. The screening supercurrents build up slowly over a distance λ_j, Josephson penetration depth (instead of ξ for the case of Abrikosov vortices), and then drop to zero over the same distance. It is known that $\lambda_j >> \lambda$ ($\lambda_j \sim 100\lambda$). Figure 51 presents a comparison between Abrikosov (in type-II conventional superconductor) and Josephson (in Josephson junction)

vortices regarding the distribution of the screening current, distribution of the local magnetic field, the phase change across the vortex and the Ginzburg-Landau order parameter. Table 10 lists the expressions which describe the parameters shown in Figure 51 for both Abrikosov and Josephson vortices.

Parameter	Abrikosov Vortex	Josephson Vortex
$j(x)$	$j_0(x/\xi)^{-1}$, $\xi<x<<\lambda$	$2j_0\tanh(x/\lambda_J)\mathrm{sech}(x/\lambda_J)$
j_0	$c\phi_0/8\pi^2\xi\lambda^2$	$c\phi_0/8\pi^2 t\lambda_J^2$
$H(x)$	$(\phi_0/2\pi\lambda^2)K_0(x/\lambda)$, $\xi<x<<\lambda$	$(\phi_0/2\pi t\lambda_J)\mathrm{sech}(x/\lambda)$
$\phi(x)$	0 for $x=-\infty$ π for $x=0$ 0 for $x=\infty$	$2\sin^{-1}(\mathrm{sech}(x/\lambda_J)$
$\lvert\Psi(x)\rvert$	$\Psi_0\tanh(x/\sqrt{2}\xi)$	constant
F, F_J	$(\phi_0^2/16\lambda^2\pi^2)\ln(\lambda/\xi)$	$2\phi_0^2/\lambda_J t\pi^2$
H_{c1}, H_{cJ}	$(\phi_0/4\lambda^2\pi)\ln(\lambda/\xi)$	$\phi_0/\pi\lambda_J t$
λ, λ_J	$(c\phi_0/8\pi^2\xi j_0)^{1/2}$	$(c\phi_0/8j_0 t\pi 2)^{1/2}$

*Table 10: Characteristic parameters** for an Abrikosov vortex and for an isolated Josephson vortex. $j(x)$ is the current density, j_0 is the maximum current, $H(x)$ is the local magnetic field, $\phi(x)$ is the phase difference of the superconducting wavefunction Ψ, F is the free energy, H_c is the critical field, λ is the penetration depth, ξ is the Ginzburg-Landau coherence length, K_0 is the Bessel function of an imaginary argument, ϕ_0 is the flux quantum, and $t=2\lambda+1$, where 1 is the*

***The parameters in Table 10 and Figure 51 are quoted from: T. Yamashita and L. Rinderer, J. Low Temp. Phys. 21, 153 (1975).*

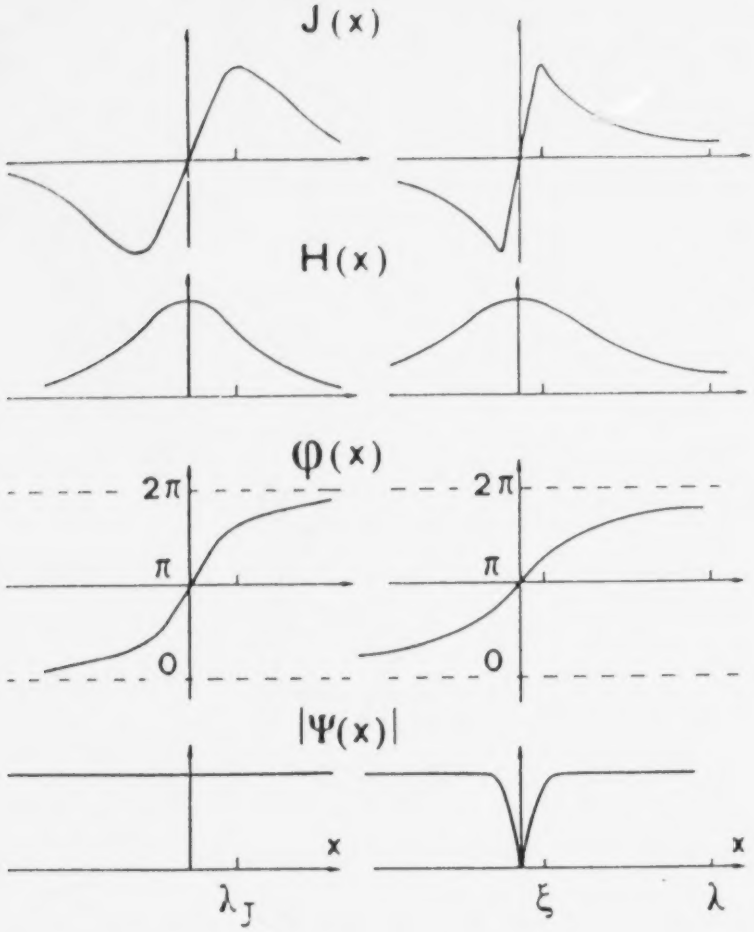

Josephson vortex Abrikosov vortex

Fig. 51. An isolated Josephson vortex compared schematically in one dimension with an Abrikosov vortex in conventional type-II superconductor.

The screening supercurrents are quite constant along the vortex direction in conventional superconductors but in high-T_c superconductors the vortices can be kinked, meander through the sample and can even exist in the form of decoupled "pan cakes" of thickness approximately equal to the spacing between Cu-O planes.

The nature of the vortices along with the operating temperature range determine whether the vortices exist, move and are pinned inside the grains (Abrikosov vortices) or in the grain boundaries (Josephson vortices). In general, Abrikosov type of vortices penetrate the superconducting grains of high-T_c superconductors along the twin boundaries within the grains. On the other hand, Josephson type of vortices are allowed to exist and creep along low angle and high angle grain boundaries. Studies of the flux motion in YBCO polycrystals using magneto-optical techniques[41] revealed that at low temperatures (over a range 7-20 K), flux lines completely penetrate the high angle grain boundaries first. Increasing the applied magnetic field causes the flux lines to gradually penetrate the low angle grain boundaries from the edges of the samples and from the adjacent high angle grain boundaries. Finally, at higher fields, flux lines start to enter the grains along the twin boundaries normal to high and low angle grain boundaries. However, in the high temperature range (30-50 K), flux lines entered the grains along the twin boundaries before moving to all of the low angle grain boundaries. It was also observed that very low angle grain boundaries (less than 4°) impede flux line motion across them and consequently may account for high current density.

Accordingly, one may argue that in the grain aligned YBCO the motion of Abrikosov vortices is responsible for the decay of the persistent current close to T_c. This argument is

supported by the magnetic field dependence of the critical current. The critical current decreases with an increasing applied magnetic field in field cooled rings according to the Kim relationship $1/(H+H_0)$, where H is the applied magnetic field. This behavior is characteristic of Abrikosov magnetic vortices in a strongly coupled conventional superconductors in contrast with Fraunhofer diffraction pattern like $I_c(H)$ which is characteristic of Josephson junctions. Therefore, we believe that the motion of Abrikosov vortices dissipates energy and leads to the decay of the persistent current in the grain-aligned YBCO ring shaped samples. In the following sections, the relationship between the motion of flux lines and the relaxation phenomena is explored. The sections deal with general equations governing flux motion and with discussion of the following features: the current and time dependence of the effective energy barrier $U_{eff}(j,t)$ close to T_c, the temperature dependence of the persistent current, the normalized decay rate S, the unperturbed pinning potential U_0 and the nonlogarithmic initial decay of the current.

4.1.1 Equations governing flux motion and time decay of the persistent current:

Ring shaped samples provide an accurate and effective method to detect the effect of flux motion on the magnitude of a self supporting persistent current. Using cylindrical coordinates (r,ϕ,z), with the ring's axis taken as the z-axis

and the persistent current circulating around the ring, the Lorentz force, F_L, on a vortex line perpendicular to the ring's plane is in the radial direction as shown in Figure 52. When the vortex line moves an electric field E is induced according to:

$$\vec{E}=\frac{1}{c}(\vec{B}^{l}x\vec{v}) \qquad (38)$$

which has the azimuthal direction along the tangent to the ring's perimeter. The magnitude of the electric field then could be written as

$$E_{\phi}=\frac{1}{c}B_{z}^{l}v_{r} \qquad (39)$$

where $B_z^{\,l}$ is the local magnetic induction in the ring's bulk due to the persistent current and v_r is the drift velocity of the vortices determined by the thermally activated hopping. The magnetic induction B and the electric field E are related through the Maxwell's equation

$$c\ curl\ \vec{E} = -(\frac{\partial\vec{B}}{\partial t}) \qquad (40)$$

Expressing the curl operator in the cylindrical coordinates and substituting for the components of E and B, Equation 40 which describes flux motion and dissipation of the persistent current due to the motion of the vortices in the ring's bulk could be written in the scalar form:

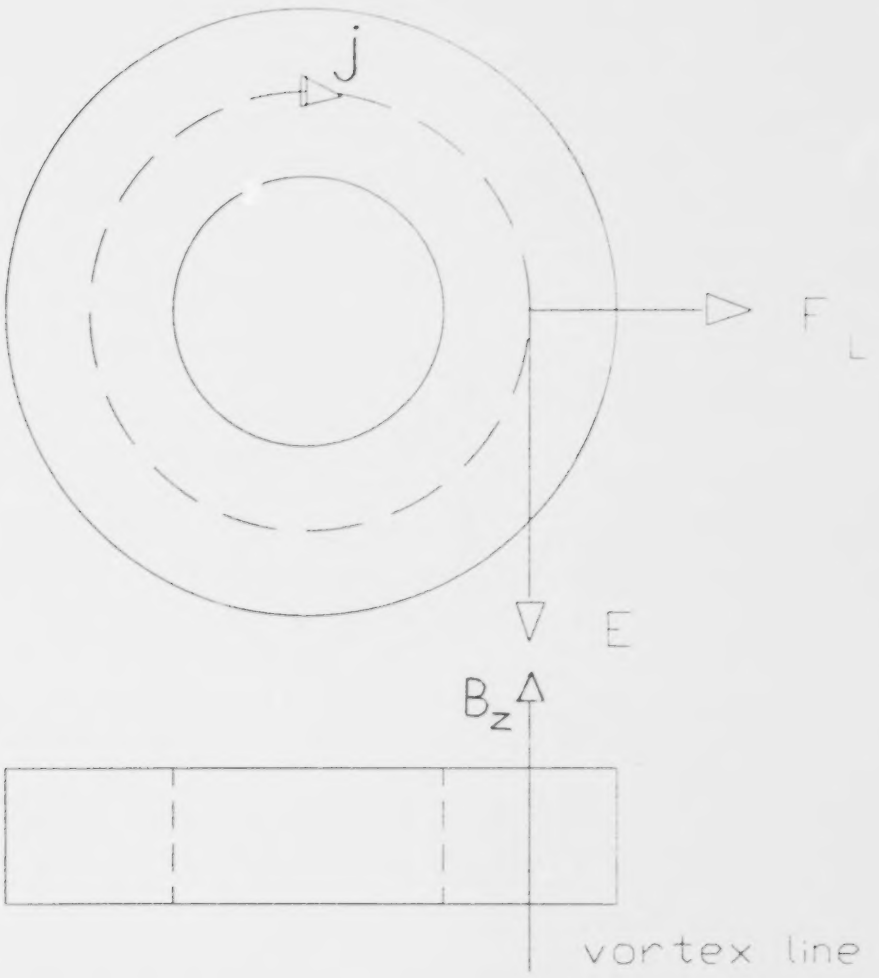

Fig. 52. Schematic diagram of the ring geometry showing a magnetic vortex trapped in the ring's bulk. The vortex line is parallel to the z axis. The dashed circle denotes a current loop with the electric field tangent to it. Lorentz force, F_L, on the vortex line is shown in the radial direction.

$$\begin{aligned}\frac{\partial B_z^1}{\partial t} &= -\frac{c}{r}\frac{\partial}{\partial r}(rE_\phi) \\ &= -\frac{1}{r}\frac{\partial}{\partial r}(rv_r B_z^1) \\ &= -v_r\frac{\partial B_z^1}{\partial r} - \frac{B_z^1}{r}\frac{\partial rv_r}{\partial r}\end{aligned} \tag{41}$$

For a narrow ring we assume that the term rv_r is a slowly varying function of distance r. Therefore the variation of this term across the ring's bulk can be neglected. Moreover, flux motion in the ring can also be treated as a one dimensional motion in the radial direction (because of the cylindrical symmetry of the ring). This approach is similar to that used in the Kim's tube experiment[43] and for slab geometry[42]. In this case curl **E** becomes dE/dr, $E=v_r B$. This leads to the equation

$$\frac{\partial B_z^1}{\partial t} = -v_r\frac{\partial B_z^1}{\partial r} \tag{42}$$

Using the explicit form of v_r[5]

$$v_r = \omega_0 a \exp\frac{-U_{eff}(J)}{kT} \tag{43}$$

where ω_0 is the characteristic attempt frequency, a is the hopping distance, and $U_{eff}(j)$ is the current dependent effective energy barrier, Equation 42 becomes

$$\frac{\partial B_z^1}{\partial t} = -\omega_0 a\frac{\partial B_z^1}{\partial r}\exp\left[\frac{-U_{eff}(j)}{kT}\right] \tag{44}$$

Equation 44 can be integrated over the ring's volume to obtain a differential equation for the time dependent magnetic

induction averaged over the ring's perimeter

$$\frac{d\langle B_z^1\rangle}{dt} = \frac{\omega_0 a}{d}\langle B_z^1\rangle|_{r=R_{id}} \exp\left[\frac{-U_{eff}(j)}{kT}\right] \qquad (45)$$

where $d = R_{od} - R_{id}$ is the ring's bulk width. Here R_{od} and R_{id} express the ring's outer and inner radii respectively. In integrating this equation,

$$\langle B_z^1\rangle|_{r=R_{od}} = 0 \qquad (46)$$

was taken as the boundary condition.

However, Figures 8 and 9 show an excess of magnetic induction at $r=R_{od}$. This is caused by the field of the magnetic vortices trapped in the ring's bulk. Since $\langle B_z^1 \rangle$ is the magnetic induction due to persistent current only, then setting the boundary condition in Equation (46) is justified. Equation (45) is essentially equivalent to those derived for a tube or slab geometry[42,43]. According to the Biot-Savart equation for a current loop[44], the magnetic induction is directly proportional to the magnitude of the current I. Therefore B_z^1 in this Equation 45 can be replaced by the magnitude of the persistent current circulating in the ring

$$\frac{dI}{dt} = \frac{\omega_0 a}{d}\, I \exp\left[\frac{-U_{eff}(j)}{kT}\right] \qquad (47)$$

or by the current density j

$$\frac{dj}{dt} = \frac{\omega_0 a}{d}\, j \exp\left[\frac{-U_{eff}(j)}{kT}\right] \qquad (48)$$

The activation energy $U_{eff}(j)$ can be extracted from the above

equation in the following form

$$U_{eff}(j) = -kT \ln\left(\frac{\frac{dI}{dt}}{I}\right) + kT \ln\left(\frac{\omega_0 a}{d}\right) \qquad (49)$$

or

$$U_{eff}(j) = -kT\left(\ln\frac{\frac{dI}{dt}}{I} - C\right) = -kT\left(\ln\frac{\frac{dj}{dt}}{j} - C\right) \qquad (50)$$

where $C=\ln(\omega_0 a/d)$ is a constant which is independent of the magnetic field and the current.

The constant $\omega_0 a$ is a prefactor in the equation for v_r. $v_0=\omega_0 a$ is the velocity of a vortex line when the probability of hopping in the direction of the Lorentz force is unity. An upper limit for v_0 = 10 m/sec for the thermally activated flux creep was calculated by Schnack *et al*[23] while Maley *et al*[8] estimated v_0 = 25 cm/sec from the measurement of magnetic relaxation performed for a grain-aligned sample of YBCO powder. Using these values and d = 0.2 cm, the constant C varies between 4.828 and 8.517. An average value of 6.672 was taken as an acceptable estimation for $C=\ln(\omega_0 a/d)$. This value corresponds to an average drift velocity v_0~160 cm/sec. An important feature of equation (50) is that it allows us to calculate $U_{eff}(I)$ directly, given that the decay curves I(t,T) are measured accurately. Using this equation and the measurements of the time decay of persistent current I(t,T) in grain-aligned YBCO rings presented in Chapter 3, one can find the current and time dependence of the effective energy barrier

$U_{eff}(j)$.

4.1.2 Current dependence of the effective energy barrier:

Figure 53 shows the dependence of the activation energy U_{eff} on the current, I, calculated from Equation (50) for a steady state logarithmic relaxation from an initial current I_0 close to $I_c(T)$; for $I_0 > 0.8I_0^{max}$, (see Figs. 14 and 15 for two grain-aligned YBCO rings: GAR1 and GAR3). In this regime, U_{eff} is proportional to the current I at each temperature over the applied temperature range of 78-88K,

$$U_{eff}(I) = U_0(T)\left[1 - \frac{I}{I_c(T)}\right] \qquad (51)$$

Equation (51) is useful in determining both $I_c(T)$ and $U_0(T)$. When the effective energy is zero, the current circulating in the ring is the critical current $I_c(T)$ whose magnitude is not accessible directly from the experiment. When the current is zero, the effective energy U_{eff} is equal to the unperturbed pinning potential U_0. Figure 54 shows the extrapolation of $U_{eff}(I)$, measured for different temperatures between 78 and 88 K, to zero current and zero energy. It is evident from Figure 54 that U_0 varies randomly between 0.35 eV and 0.5 eV with a tendency to acquire higher values at higher temperatures (86-88 K). The average value of U_0 is about 0.4 eV over the temperature range 78-88 K. The critical current $I_c(T)$, obtained from extrapolating $U_{eff}(I)$ to zero effective energy, ranges from 40 A at 88 K to 250 A at 78 K in ring GAR1 and from 185 A at 88 K to 650 A at 81 K in ring GAR3. Taking the

$U_{eff}(j)$.

4.1.2. Current dependence of the effective energy barrier:

Figure 53 shows the dependence of the activation energy U_{eff} on the current, I, calculated from Equation (50) for a steady state logarithmic relaxation from an initial current I_0 close to $I_c(T)$; for $I_0 > 0.8I_0^{max}$, (see Figs. 14 and 15 for two grain-aligned YBCO rings: GAR1 and GAR3). In this regime, U_{eff} is proportional to the current I at each temperature over the applied temperature range of 78-88K,

$$U_{eff}(I) = U_0(T)\left[1 - \frac{I}{I_c(T)}\right] \qquad (51)$$

Equation (51) is useful in determining both $I_c(T)$ and $U_0(T)$. When the effective energy is zero, the current circulating in the ring is the critical current $I_c(T)$ whose magnitude is not accessible directly from the experiment. When the current is zero, the effective energy U_{eff} is equal to the unperturbed pinning potential U_0. Figure 54 shows the extrapolation of $U_{eff}(I)$, measured for different temperatures between 78 and 88 K, to zero current and zero energy. It is evident from Figure 54 that U_0 varies randomly between 0.35 eV and 0.5 eV with a tendency to acquire higher values at higher temperatures (86-88 K). The average value of U_0 is about 0.4 eV over the temperature range 78-88 K. The critical current $I_c(T)$, obtained from extrapolating $U_{eff}(I)$ to zero effective energy, ranges from 40 A at 88 K to 250 A at 78 K in ring GAR1 and from 185 A at 88 K to 650 A at 81 K in ring GAR3. Taking the

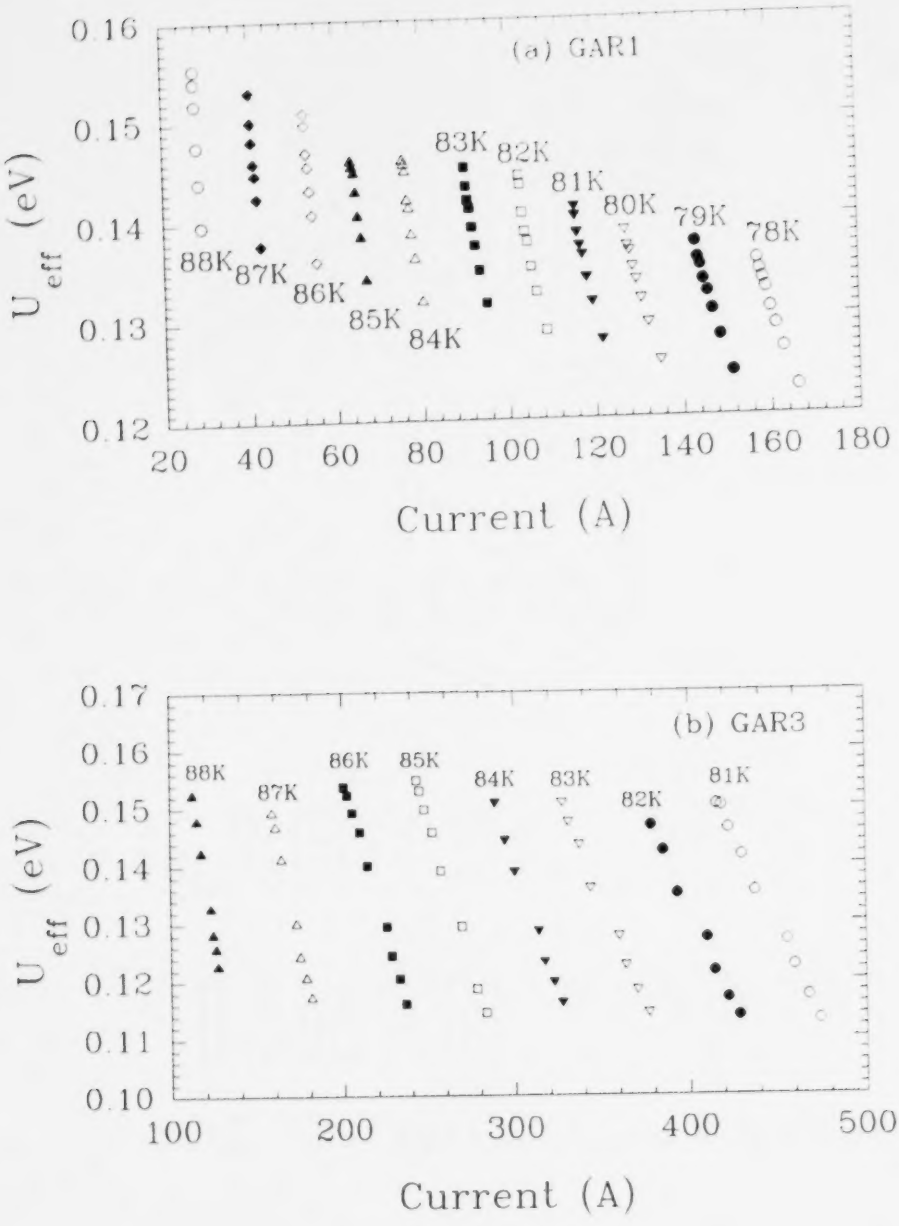

Fig. 53. The effective energy barrier U_{eff} calculated as a function of the magnitude of the persistent current from Equation (50) for a steady state logarithmic decay at various temperatures over a range 78 - 88 K for two grain-aligned rings: (a) GAR1, (b) GAR3. U_{eff} is proportional to the current for all temperatures in this range.

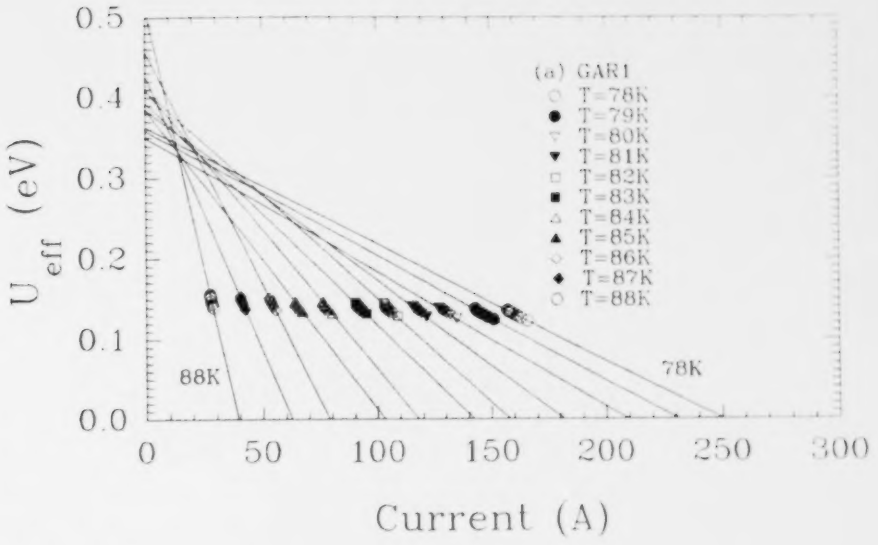

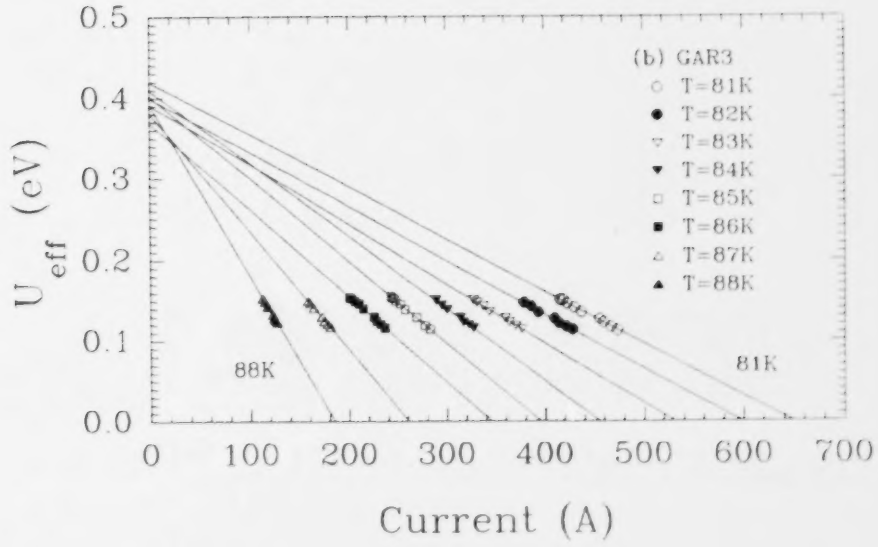

Fig. 54. The data of Fig. 53 plotted using an extended scale of U_{eff} and the current. Extrapolation of $U_{eff}(I)$ to zero current provides U_0 of average value of 0.4 eV. Extension of $U_{eff}(I)$ to zero effective energy gives values of the critical current $I_c(T)$.

ring's cross-sectional area of 2.0 mm^2, the apparent critical current density (j=I/A) varies between 2000 A/cm^2 at 88 K and 12,000 A/cm^2 at 78 K in ring GAR1 and between 9300 A/cm^2 at 88 K and $3.3x10^4$ A/cm^2 at 81 K in ring GAR3.

The magnitude of U_{eff}, for a wide range of magnitudes of the persistent current at constant temperatures, can be extracted from the decays of the persistent current (Figures 16 and 17) at a fixed value of time. $U_{eff}(I)$ calculated at a temperature of 81 K for different waiting times during the relaxation process in ring GAR1 and the corresponding one at 85 K in ring GAR3 are shown in Figure 55. For instance, for ring GAR1, at a fixed value of the waiting time, U_{eff} is current independent up to about $0.75I_0^{max}$ (I_0^{max} = 150 A, I_c = 180 A) and at higher currents it drops linearly with the current according to the formula $\{U_{eff}(I) = 0.4(eV) [1 - I/180(A)]\}$. This behavior is typical for a temperature range of 78 - 88 K for ring GAR1 and 81-88 K for ring GAR3.

Measurements of the magnetization relaxation M(t) in MPMG processed grain-aligned YBCO have been performed by Kung *et al*[20] using the Maley's method[8]. The studies was performed over a temperature range 5-80 K at a high magnetic field of 1-4 T. $U_{eff}(j)$ was calculated from M(t) data versus j close to j_c. $U_{eff}(j)$ curve consists of many segments, each of which representing data collected at a given temperature. The lowest temperature of 5 K corresponds to the high j_c side. With increasing temperature, j_c values decreases and U_{eff} gradually

increases. The constant $C=\ln(B\omega_0 a/\pi d)$ in Equation 16 was selected to achieve continuity of $U_{eff}(j)$. A smooth curve was obtained for temperatures below 30 K, however, close to T_c at temperatures between 50 and 80 K, a single value of C did not result in continuous $U_{eff}(j)$ segments (see Figure 7 in Ref. 20). Close to T_c, one obtains a collection of segments which do not lie on a continuous curve. The same behavior can be seen in Figures 53 and 54.

4.1.3. Time dependence of the energy barrier:

For currents close to the critical current, Equation (48) could be solved up to logarithmic accuracy in order to obtain the time dependence of U_{eff} in the following form

$$U_{eff} = kT \ln\left(\frac{-\gamma}{kT}\frac{dU_{eff}}{dj}t\right) \qquad (52)$$

where $\gamma \approx (-\omega_0 a/d) j_c$, a factor that depends on the sample geometry. Equation (52) could be also written as

$$U_{eff} = kT \ln\left(\frac{t}{t_{eff}}\right) \qquad (53)$$

where

$$t_{eff} = \frac{-kT}{\gamma \frac{dU_{eff}}{dj}} \qquad (54)$$

is a characteristic time. Two predictions can be drawn from Equation (53): (1) When critical current density j_c is reached at a specific temperature, the critical state is established

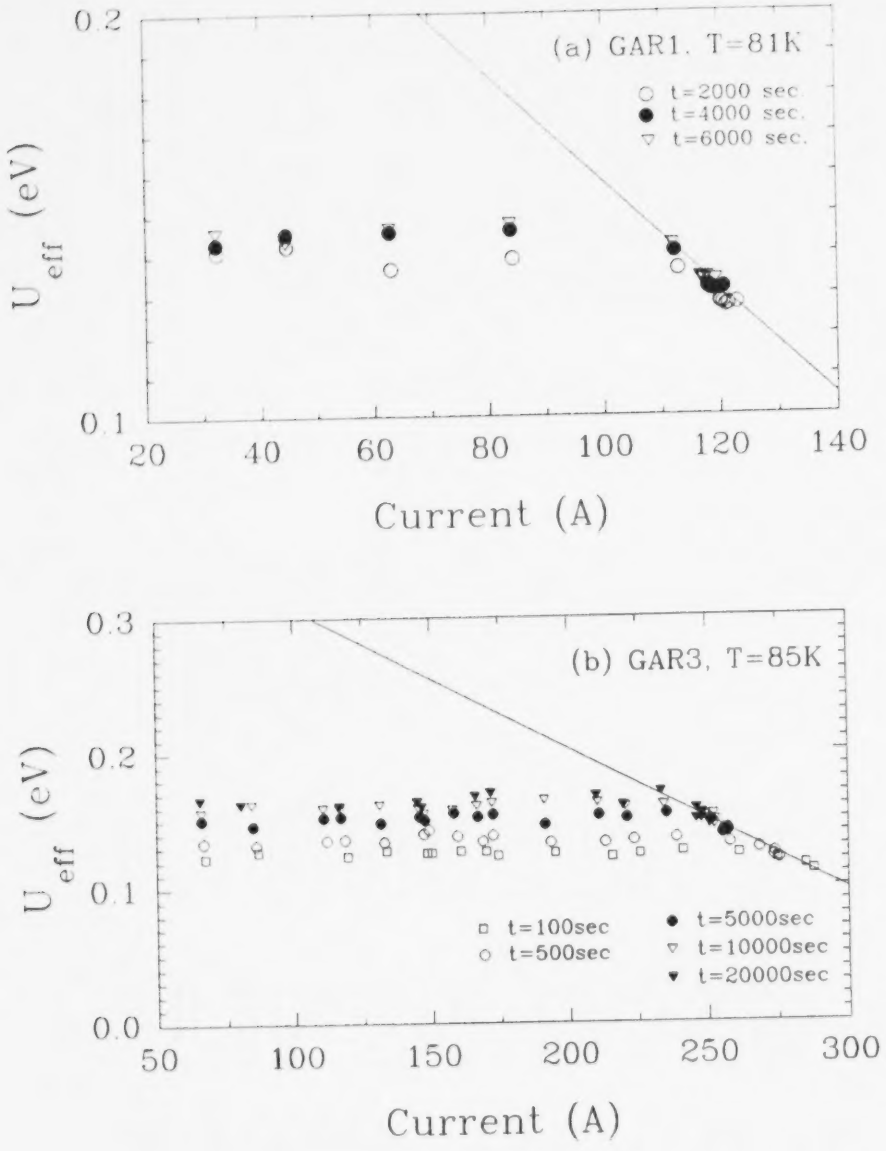

Fig. 55. Dependence of U_{eff} on the current (a) at 81 K in ring GAR1 and (b) at 85 K in ring GAR3. U_{eff} was calculated from Equation (50) for fixed values of waiting time. At a fixed time U_{eff} is current independent up to 75% of the initial current and at higher currents it drops linearly with the current. The straight line marks the linear dependence of U_{eff} on current for a steady state logarithmic relaxation.

over a short time period up to t_{eff}, after which the current density starts to decrease due to flux creep, (2) The magnitude of t_{eff} depends on the current dependence of U_{eff}. t_{eff} was estimated to be 10^{-5}-10^{-10} sec[9,45]. Taking the value quoted here for the average drift velocity v_0 and the linear dependence of $U_{eff}(I)$, t_{eff} can be estimated from Equation (54) to be 4.6×10^{-6} sec at 81 K. Figure 56 shows U_{eff} increasing linearly with ln(t) for different levels of the persistent current. The dependence of U_{eff} on time for a steady state logarithmic decay allows one to deduce t_{eff} using the condition $U_{eff}(t_{eff})=0$. The values of t_{eff} estimated from the graphs are 5×10^{-6} sec for GAR1 and 5×10^{-5} sec for GAR3 between 81 and 87 K. Extrapolation of the steady state logarithmic decays (Figure 14) back to I_c A gives times t_{eff} at which the relaxation of the persistent current has started, equal to 5×10^{-6} sec for GAR1 and 3×10^{-5} for GAR3. The agreement between these times and those obtained before suggests that the estimation of $I_c(T)$ from Figure 56 is correct.

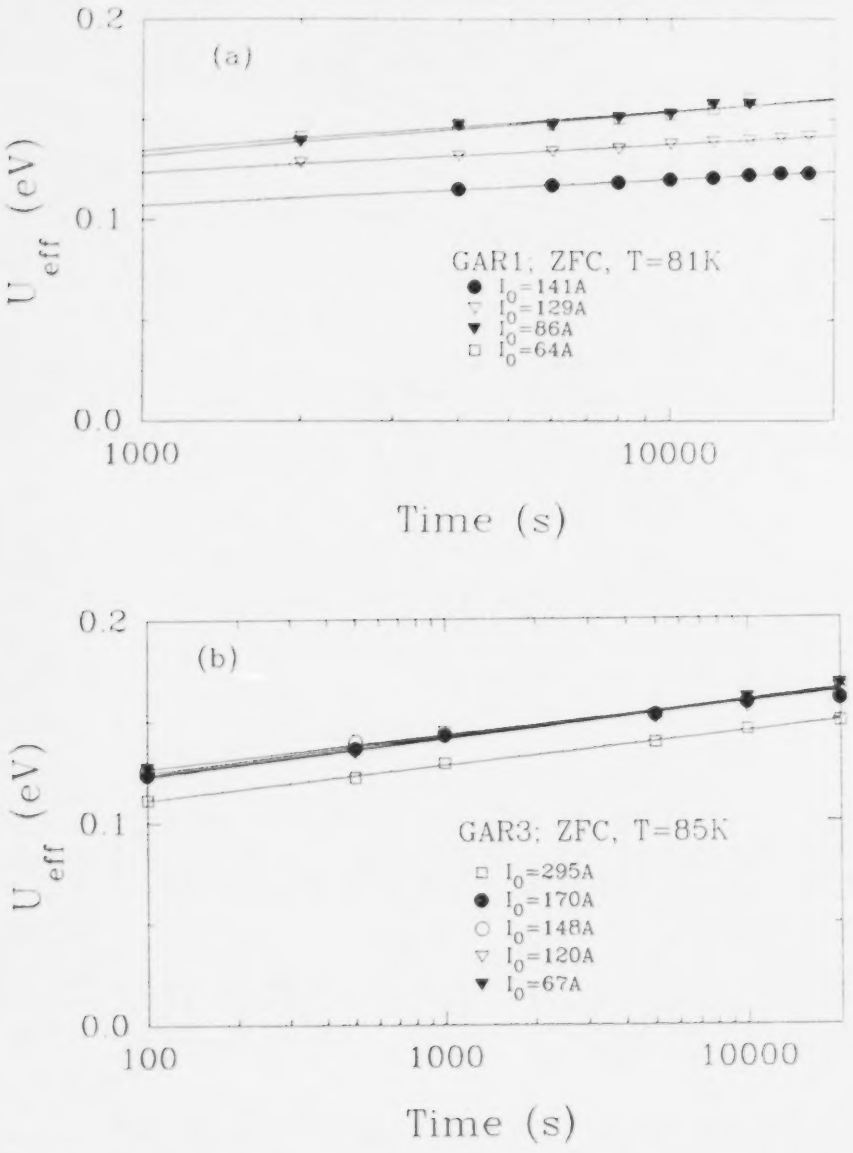

Fig. 56. Dependence of U_{eff} on time at (a) 81 K in ring GAR1 and (b) 85 K in ring GAR3, plotted for various values of an initial current I_0. U_{eff} is proportional to ln(t) for all levels of current. Extrapolation of $U_{eff}(t)$ to $U_{eff}=0$ for a steady state logarithmic decay from an initial current I_0 gives $t_{eff}=5x10^{-6}$ sec for GAR1 and $5x10^{-5}$ sec for GAR3.

4.1.4. Temperature dependence of the persistent current:

Dependence of the persistent current on temperature is plotted in Figure 57. The critical current values $I_c(T)$ are those obtained from the extrapolation of U_{eff} (I) down to $U_{eff}=0$ (Figure 54). $I_c(T)$ is linear over the applied temperature range. This linear dependence is not affected by the decay of the persistent current from its critical value I_c. During the first 30 sec, which is the time required to move the measuring Hall probe from the edge to the center of the sample, the current decays to about $0.75I_c$. This implies a very large decay rate at the beginning of the relaxation process. We made an attempt to evaluate the decay rate close to I_c using Equation (50) and the condition $U_{eff}(I_c)=0$. Under this condition the decay rate close to the critical current is given by

$$\frac{dI}{dt}\Big|_{I\sim I_c} = I_c\left(\frac{\omega_0 a}{d}\right) \qquad (55)$$

Using the average value of $v_0=\omega_0 a=160$ cm/sec and d=0.2 cm, dI/dt was found to be about 5×10^5 A/sec for ring GAR1 with I_c=180 A at 81 K and about 4×10^5 A/sec for ring GAR3 with I_c=400 A at 85 K (see Fig. 57). This means that an initial drop of 4-5 A could occur during the first 0.01 msec. This fast decay rate depends on the temperature implicitly through $I_c(T)$.

The relative change in the magnitude of the current density $(j_c-j)/j_c$, measured at various waiting times as a

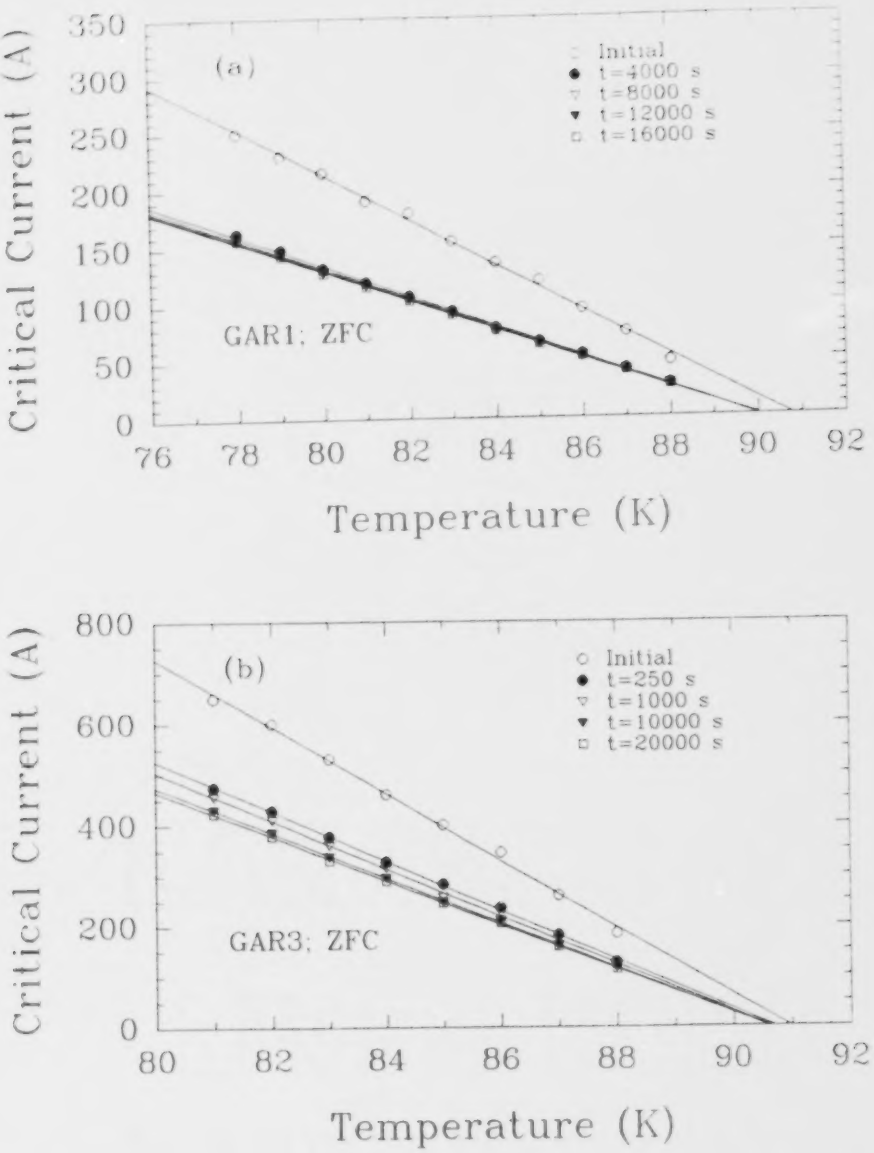

Fig. 57. Dependence of the magnitude of the persistent current on temperature over a range (a) 78-88 K in ring GAR1 and (b) 81-88 K in ring GAR3, plotted for various waiting times between 4000 and 16000 sec in ring GAR1 and between 250 and 20,000 sec in ring GAR3. The open circles mark the values of $I_c(T)$ obtained from the extrapolation of $U_{eff}(I)$ down to zero (Figure 54).

function of temperature for a steady state logarithmic decay, is shown in figure 58. The linear dependence of this factor on temperature suggests that the current relaxation in this case is described by the Anderson's formula

$$j(t)=j_c(T)\left[1-\frac{kT}{U_0}\ln\left(\frac{t}{t_{eff}}\right)\right] \qquad (56)$$

where $U_0\approx 0.4$ eV and $t_{eff}=5\times10^{-6}$ sec for a temperature range 78-88 K in ring GAR1 and $t_{eff}=5\times10^{-5}$ sec for a temperature range 81-88 K in ring GAR3.

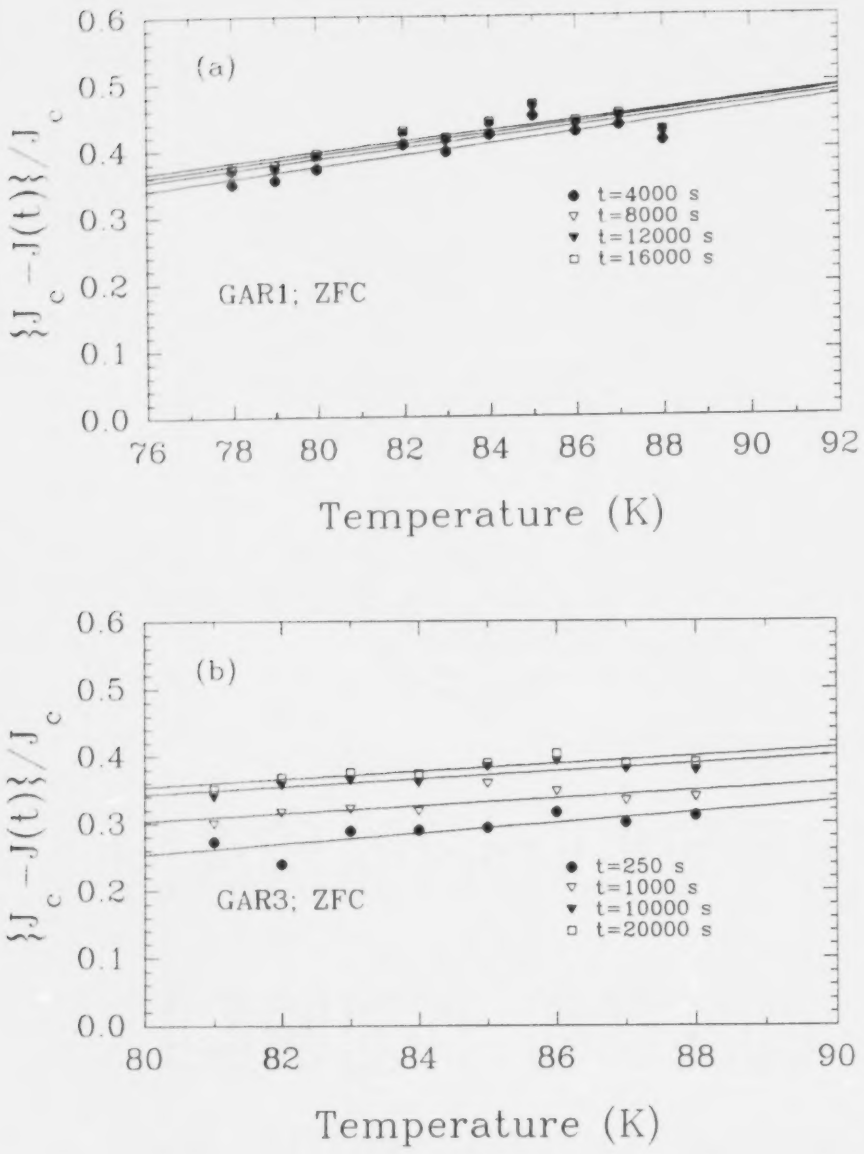

Fig. 58. The dependence of the factor $(j_c-j)/j_c$ on temperature, plotted for various waiting times during steady state logarithmic relaxation.

4.1.5. Temperature dependence of the normalized decay rates:

The normalized logarithmic decay rate $S=1/I_c^*(dI/dlnt)$ was found to be a temperature independent quantity (Figure 59). For $I_c^*=I_c$, which is the correct value of the critical current obtained from Figure 54, S varies between 0.014 and 0.017 in ring GAR1 and between 0.016 and 0.02 in ring GAR3. However, for $I_c^* = I_0^{max}$, S=0.017-0.024 in ring GAR1 and 0.022-0.027 in ring GAR3. These values lie within the range of values of S=0.020-0.035 reported by Malozemoff and Fisher for a variety of YBCO superconductors[46]. The data obtained here are especially in a very good agreement with those of Keller *et al.*[47] close to T_c on melt-processed crystals at remanence after application of saturating fields along the c-axis. S is an inverse measure of the barrier height, $U_0(T)=kT/S(T)$. $U_0(T)$ calculated from S varies between 0.3 and 0.5 eV for temperature range between 78 and 88 K in ring GAR1 and between 0.36-0.44 eV for a temperature range between 81 and 88 K in ring GAR3 (Figure 60), in agreement with the values of U_0 obtained from Figure 54 using the condition $U_0=U_{eff}(I=0)$. $U_0/kT\approx55$ over this temperature range for both two rings. The results from vibrating sample magnetometer of Keller[47] at a temperature of 85 K give a ratio of 56.

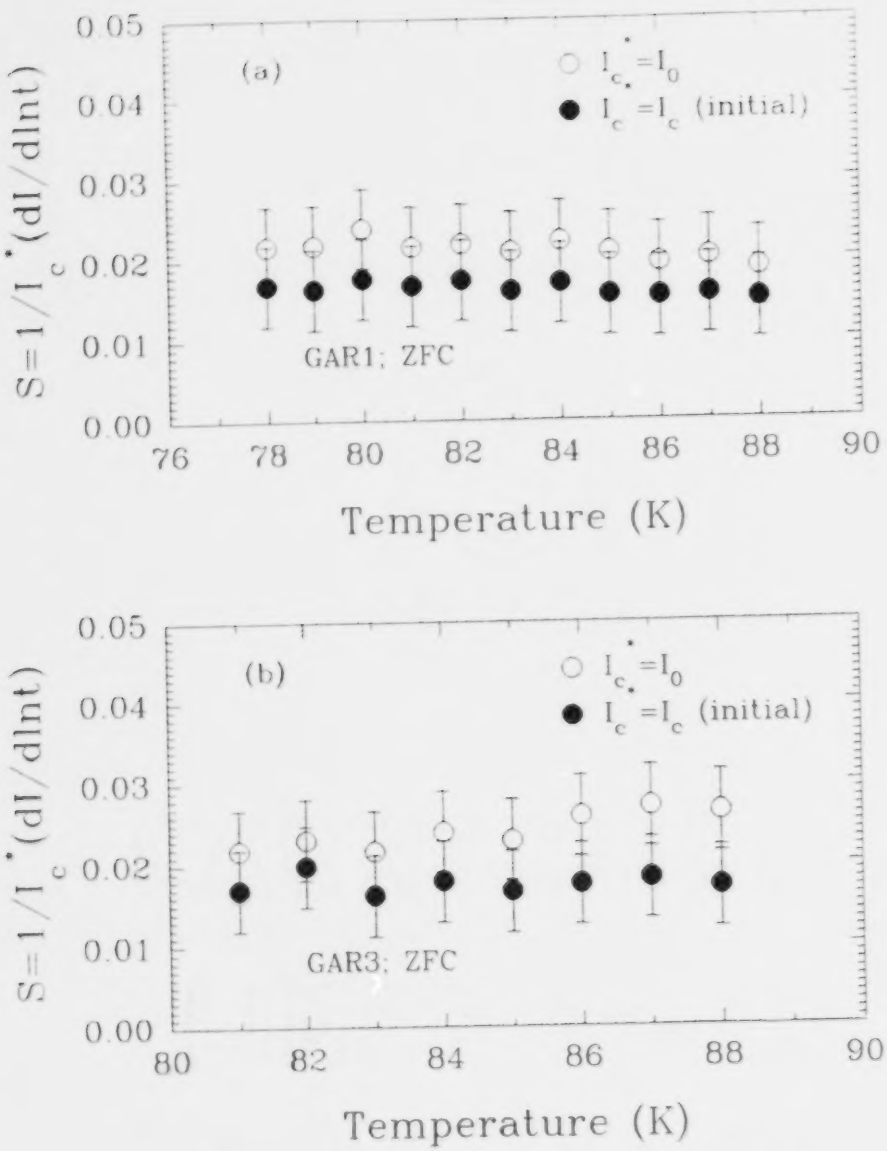

Fig. 59. Dependence of the normalized logarithmic decay rates on temperature. Open circles mark S calculated using $I_c^* = I_0^{max}$, the maximum persistent current generated in a ring. Solid circles mark S calculated using $I_c^* = I_c$, the magnitude of the critical current taken from Fig. 54.

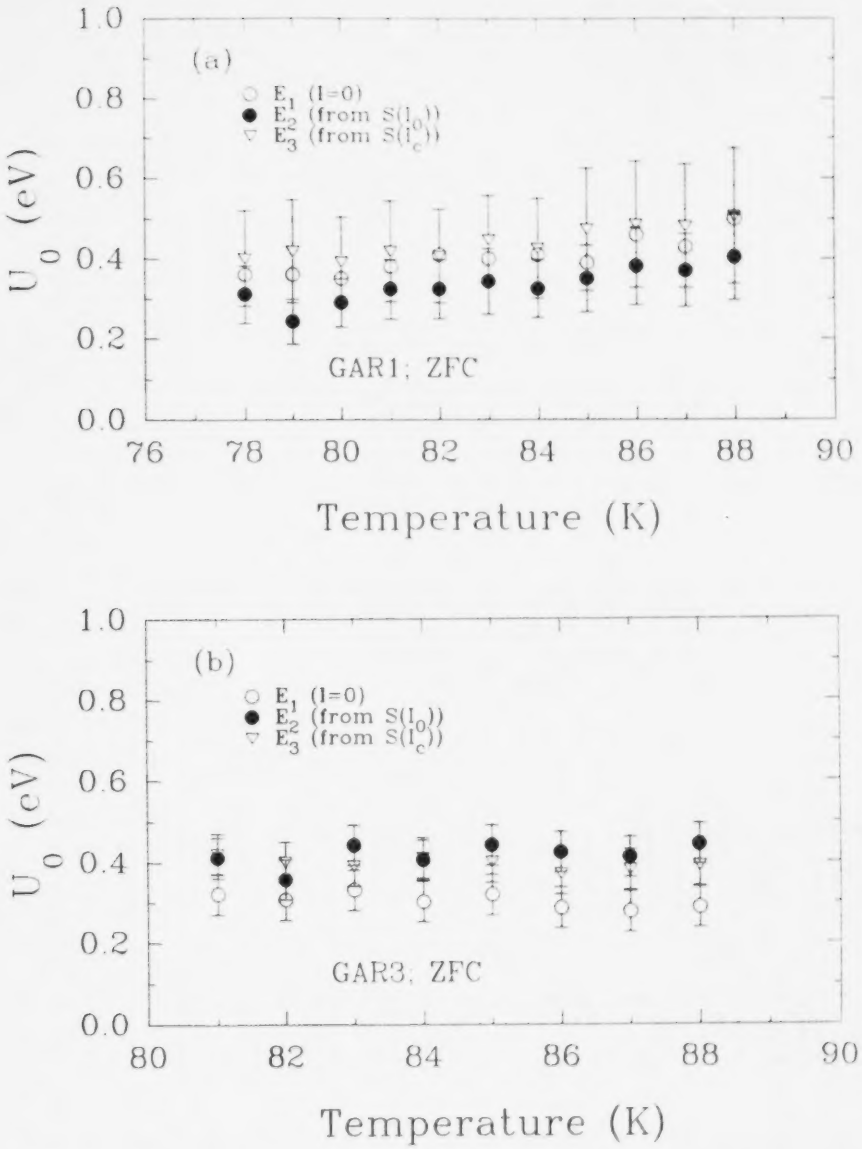

Fig. 60. Dependence of U_0 on temperature. E_1 denotes values of U_0 obtained from Fig. 54 using the condition $U_0=U_{eff}(I=0)$, E_2 denotes values of U_0 obtained from $S=kT/U_0$ with $I_c^*=I_0^{max}$ and E_3 denotes values of U_0 obtained from $S=kT/U_0$ with $I_c^*=I_c$.

4.1.6. Non-logarithmic initial decays:

Measurements of the persistent current relaxation (Figures 14 and 15) revealed a non-logarithmic initial decays which after a certain time converge into a steady state logarithmic decay. Gurevich[48] and Gurevich and Kupfer[49] reported observations of slow initial nonlogarithmic decays of magnetization in grain-aligned YBCO, when the sample was subjected to various sweep rates, dB_{ext}/dt, of the external magnetic field between 2 and 10 T. Low sweep rates led to both reduced magnetization and reduced initial decay rate. All the relaxation rates obtained for various dB_{ext}/dt at a constant temperature of 77 K converge into one steady state logarithmic relaxation curve after a time $t_p \propto 1/(dB_{ext}/dt)$. On the basis of our experiment, it seems that the duration of the initial non-logarithmic stage is determined by the ratio j_0/j_c, where j_0 is the initial current density. This view agrees with the results of the flux creep annealing experiment shown in Figure 19. Similar results were obtained by Maley[8] and Thompson *et al*[50]. In these studies progressively smaller current densities were established at high temperatures after which the sample was cooled to the lower operating temperature for measurement of M(t). For $j_0 < j_c$, the relaxation begins at smaller values of the initial magnetization decay. According to Figure 19, reduction of the magnitude of the persistent current is associated with a slow initial non-logarithmic decay.

The slow initial decay of magnetization M(t) reported by Gurevich *et al* was interpreted as due to the transient diffusion redistribution of magnetic flux over the sample volume. M(t) at short times was described by the formula

$$M(t)=M(0)-\left(\frac{kTM_c}{U_0}\right)\ln\left(1+\frac{t}{t_p}\right) \qquad (57)$$

where t_p is a time constant which determines the duration of the initial non-logarithmic relaxation. The value of t_p was estimated from the point of intersection of two straight lines, short and long term asymptotes of M(t). In the case of the persistent current relaxation, Equation 57 transforms to

$$I(t)=I_0-I_c\left(\frac{kT}{U_0}\right)\ln\left(1+\frac{t}{t_p}\right) \qquad (58)$$

Figure 61 shows the dependence of t_p, extracted from the relaxation curves I(t) at 85 K, on the initial current I_0 for two grain aligned rings No GAR1 and No. GAR3. A logarithm of t_p decreases linearly with increasing I_0. Extrapolation of $\log_{10}t_p$ to $I_0=I_c$ gives $t_{eff}\sim10^{-5}$ sec.

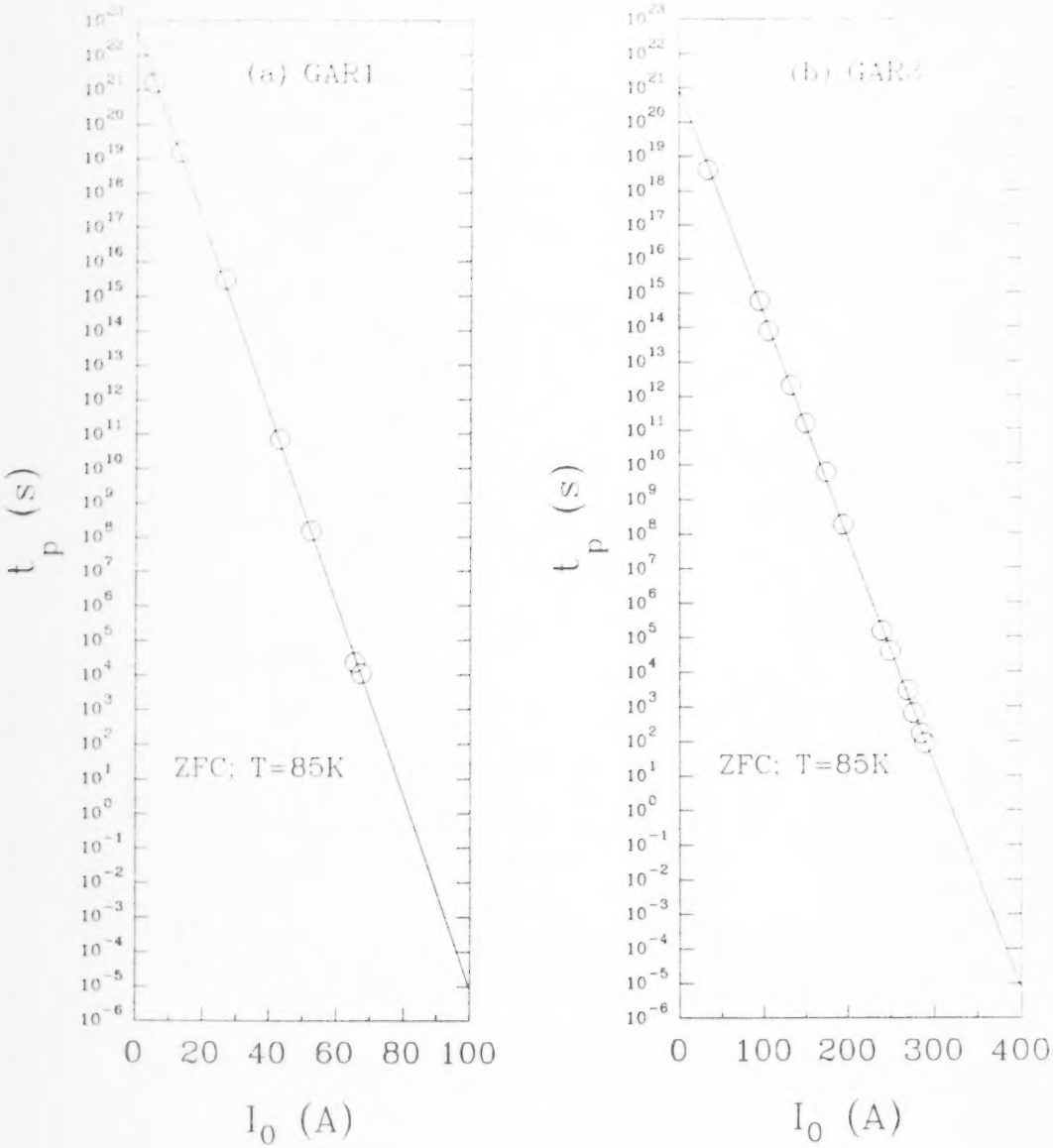

Fig. 61. Time constant t_p at T=85 K plotted for various values of the initial current I_0. $\log_{10} t_p$ decreases linearly with increasing I_0. Extrapolation of I_0 to I_c gives $t_{eff} \sim 10^{-5}$ sec.

4.2. Ceramic YBCO rings:

Measurements performed on YBCO ceramics provide important information on the intrinsic nature of the intergrain superconducting junctions in $Y_1Ba_2Cu_3O_{7-\delta}$ and on the intergrain flux creep controlled transport current in this material. Measurements of the intergrain current I_{cJ} on temperature and magnetic field revealed different character of the grain boundaries in YBCO ceramics in comparison to those in YBCO/Ag ceramic composites. Decays of the persistent current studied at various temperatures showed that the process of relaxation is thermally activated. The results obtained in our experiment, which were based on the measurement of a true supercurrent, have been used to address several problems related to the microstructure of the grain boundaries and their electrical and magnetic properties. The problems that have been considered are as follows:

(1) What model of the grain boundary should be used to describe the weak links in high-T_c ceramics?

(2) What does the temperature and magnetic field dependence of I_{cJ} imply about the grain boundary microstructure?

(3) How does the pinning and motion of magnetic flux lines at the grain boundaries affect the intergrain transport current?

In the following section, we discuss the temperature dependence of the critical current close to T_c^*, which was used to classify and characterize the intergrain junctions in the absence of magnetic field (the zero field cooling case) and in

the presence of magnetic field (the field cooling case). This is followed by a discussion of the origin of the unperturbed pinning potential U_0 which pins down magnetic vortices in the grain boundaries. Behaviour of U_0 was inferred from measurements of the relaxation of the depinning critical currents in ceramic rings.

4.2.1. Classification of the intergrain junctions:

According to Equations 21 and 23, close to T_c^*, $I_c(T)$ can be expressed always in the form

$$I_c(T) = constant(T_c^* - T_c)^{\alpha} \qquad (59)$$

where α is a constant determined by the type of the intergrain junction. For the weak coupling α has two values; 1 for SIS tunnel junctions or 2 for SNS proximity junctions. In the strong coupling limit $\alpha=3/2$.

Measurements of I_c as a function of temperature close to T_c^* (65-95 K) have been used to determine what type of intergrain junctions exists in high-T_c ceramic compounds. Figures 62 to 65 present the dependence of I_c on $1-T/T_c^*$ for four rings picked up from four different groups of ceramic samples; YBCO, YBCO/Ag(4%wt), YBCO/Ag(2%wt) with interfaces and $Pr_{0.2}Y_{0.8}Ba_2Cu_3O_{7-\delta}$. These results were plotted on a logarithmic scale in order to determine the value of α in Equation 59 for temperatures close to T_c^* of the intergrain junction. Tables 11 - 14 summarize the results for the ZFC and FC cases.

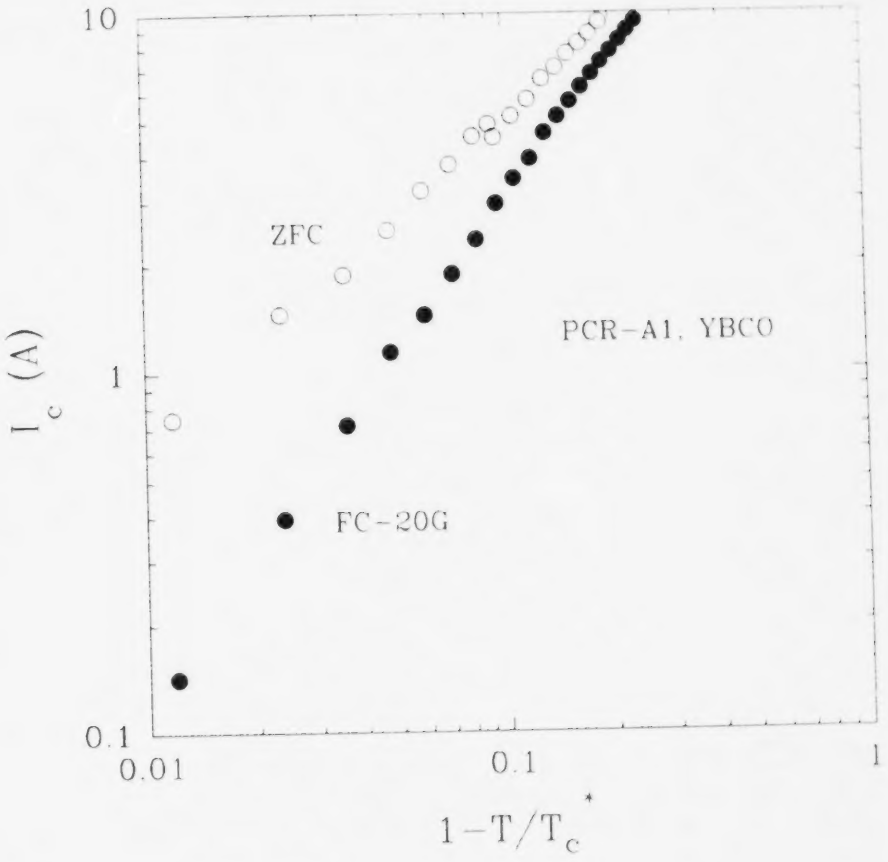

Fig. 62. The dependence of I_c in YBCO ring PCR-A1 on the reduced temperature $1-T/T_c^*$ plotted for the ZFC and FC(20G) cases.

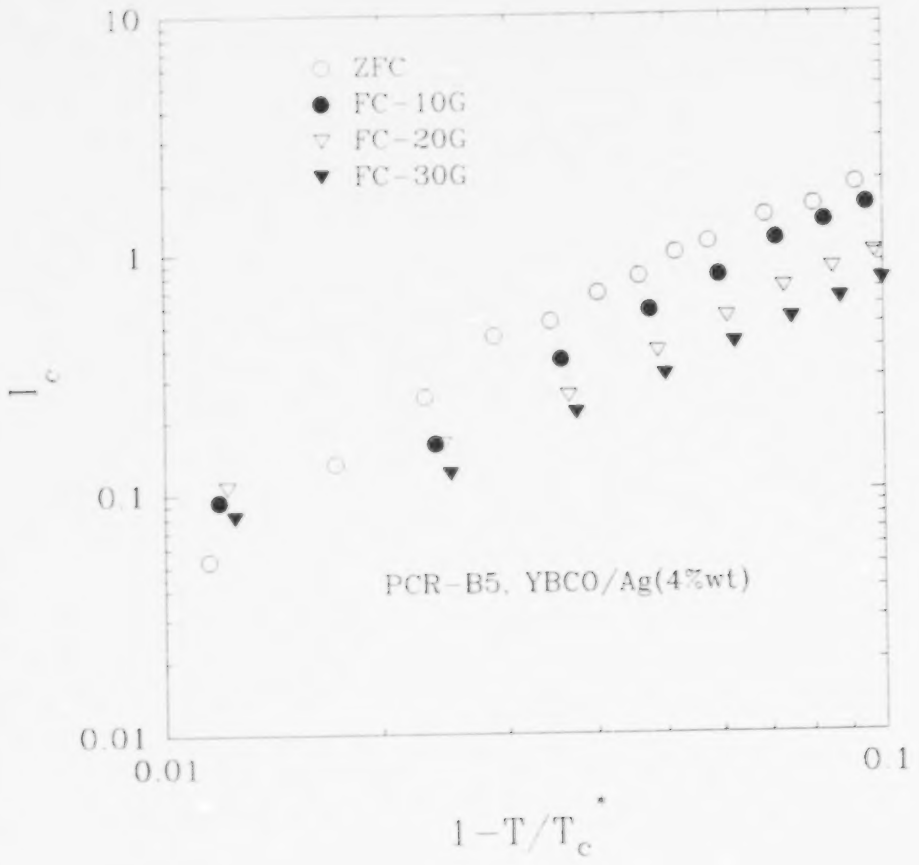

Fig. 63. The dependence of I_c in YBCO/Ag(4%wt) ring PCR-B5 on the reduced temperature $1-T/T_c^*$ plotted for the ZFC, FC(10G), FC(20G) and FC(30G) cases.

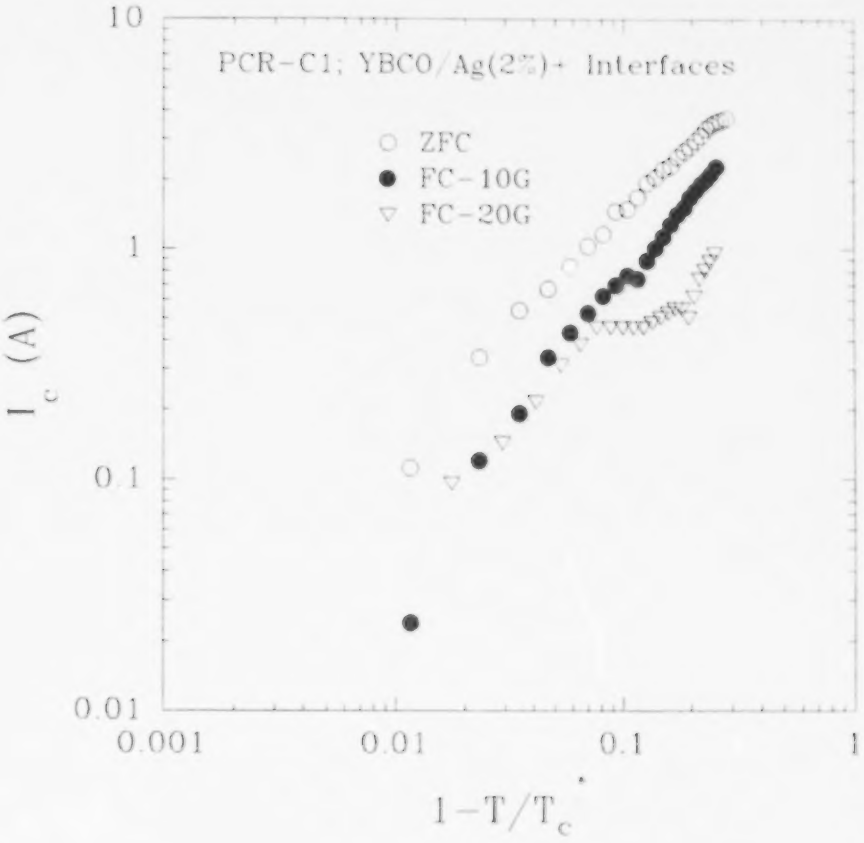

Fig. 64. The dependence of I_c in the YBCO/Ag(2%wt) ring PCR-C1 (containing interfaces) on the reduced temperature $1-T/T_c^*$ plotted for the ZFC and FC(10G) cases.

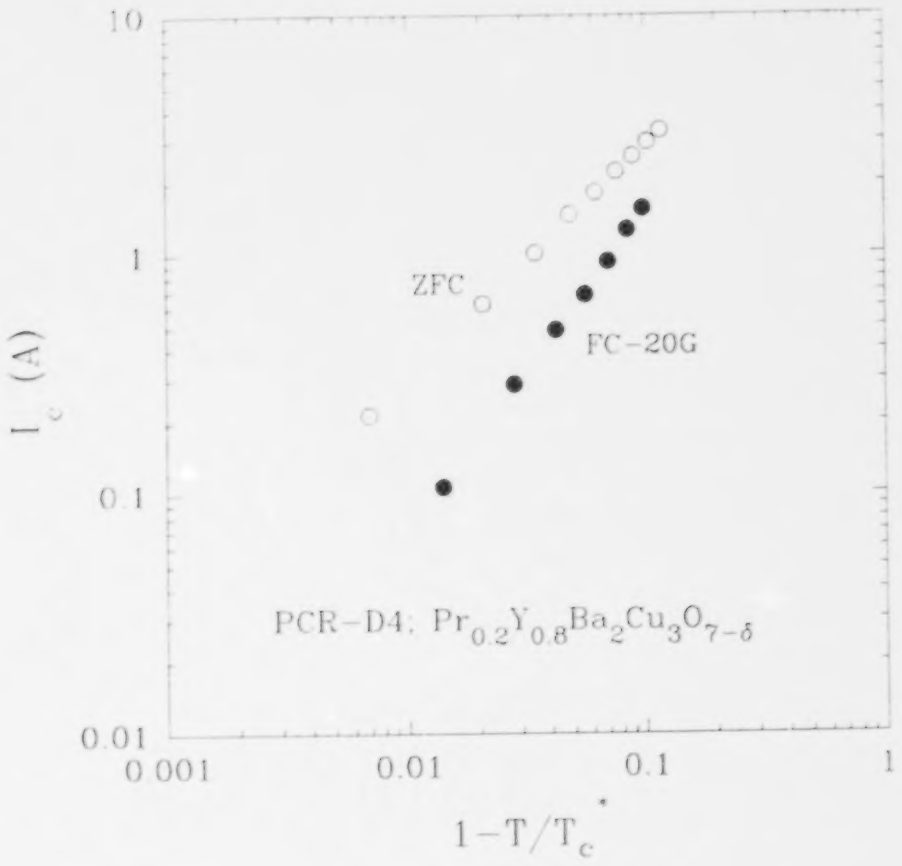

Fig. 65. The dependence of I_c in $Pr_{0.2}Y_{0.8}Ba_2Cu_3O_{7-\delta}$ ring PCR-D4 on the reduced temperature $1-T/T_c$ plotted for the ZFC and FC(10G) cases.

Ring YBCO	Dissipation	α (ZFC) ±10% (Temp. range)	α (FC) ±10% (Temp. range)
PCR-A1	Yes	0.94 (64-85 K)	1.51 (20G) (79-83 K)
PCR-A2	Yes	0.90 (81-86 K)	1.35 (20G) (77-82 K) 1.35 (40G) (67-77 K)
PCR-A3	No	1.18 (64-87 K)	1.19 (10G) (74-86 K) 1.15 (20G) (76-84 K) 1.15 (30G) (77-82 K)

Table 11: Exponent α values and their field dependence for group A of ceramic YBCO rings.

Ring YBCO/Ag(x%wt)	x	Dissipation	α (ZFC) ±10% (Temp. range)	α (FC) ±10% (Temp. range)
PCR-B1	2	Yes	2.16 (80-87 K)	1.50 (20G) (80-84 K) 1.44 (40G) (79-84 K) 1.44 (60G) (81-84 K)
PCR-B2	2	Yes	1.94 (81-86 K)	---
PCR-B3	2	Yes	1.97 (81-87 K)	1.41 (20G) (80-85 K)
PCR-B4	4	No	1.59 (82-87 K)	1.54 (10G) (77-85 K) 1.33 (20G) (77-81 K) 1.41 (30G) (73-78 K)
PCR-B5	4	No	2.22 (80-86 K)	1.42 (10G) (78-83 K) 1.44 (20G) (77-82 K) 1.43 (30G) (74-80 K)

Table 12: Exponent α values and their field dependence for group B of ceramic YBCO/Ag rings.

Ring YBCO/Ag(2%wt) + Interfaces	Dissipation	α (ZFC) ±10% (Temp. range)	α (FC) ±10% (Temp. range)
PCR-C1	No	1.11 (68-86 K)	1.43 (10G) (80-85 K) 1.43 (20G) (80-85 K)
PCR-C2	No	1.18 (65-86 K)	1.39 (70-82 K) 1.39 (66-75 K)

Table 13: Exponent α values and their field dependence for group C of ceramic YBCO/Ag rings containing interfaces.

Ring	Dissipation	α (ZFC) ±10% (Temp. range)	α (FC) ±10% (Temp. range)
PCR-D1 (GBCO)	Yes	0.95 (65-91 K)	1.53 (20G) (78-88 K) 1.60 (40G) (78-86 K)
PCR-D2 (EBCO)	No	0.92 (65-92 K)	1.51 (20G) (80-88 K) 1.53 (40G) (78-86 K)
PCR-D3 $Pr_{.15}Y_{.85}Ba_2Cu_3O_{7-\delta}$	Yes	1.15 (64-77 K)	1.45 (10G) (70-76 K)
PCR-D4 $Pr_{0.2}Y_{0.8}Ba_2Cu_3O_{7-\delta}$	Yes	1.01 (65-73 K)	1.49 (10G) (66-71 K)

Table 14: Exponent α values and their field dependence for group D of ceramic rings.

For the zero field cooled (ZFC) samples of groups A, C and D, (except YBCO/Ag group B), the value of α is always close to unity within an experimental error of 10%. The dependence of I_c on temperature agrees with that represented by Equation 21 for a Josephson tunnel (SIS) junction. Intergrain junctions in YBCO compounds were found to be oxygen depleted[51] using electron energy loss spectroscopy. The insulating layer between superconducting grains may therefore be formed by an oxygen deficient YBCO.

On the other hand, for the zero field cooled YBCO/Ag samples of group B, α was found to be 2 within an experimental error of 10%, except for ring No. PCR-B4 in which α=1.59. Close to T_c^*, the dependence of I_c on temperature follows that of Equation 23 for a proximity SNS junction. Figure 66 shows the values of α acquired by all zero field cooled samples. The horizontal lines represent two theoretical limits for α; 1 for the SIS tunnel junction and 2 for the SNS proximity junction.

Weak magnetic fields up to 60 G have unique effect on the dependence of I_c on temperature close to T_c^* and consequently on the value of α. In the case of SIS tunnel junctions, the applied magnetic field increases the value of α, while in the case of SNS proximity junctions, magnetic field reduces α. Figure 67 shows the values of α acquired by all field cooled samples based on the information collected in Tables 11-14.

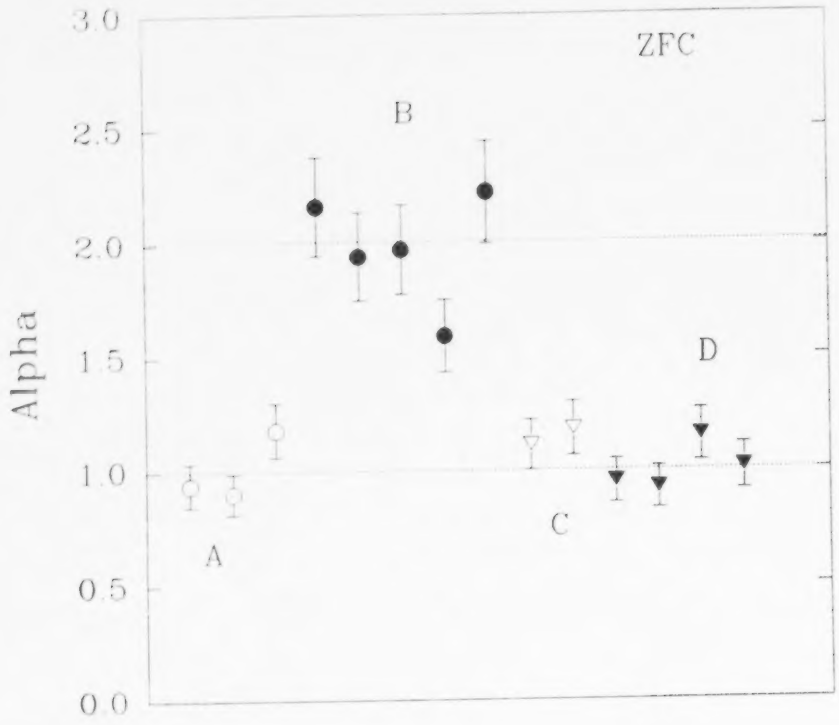

Fig. 66. The values of α acquired by all samples in the ZFC case. The horizontal axis represents different samples from group A (open circles), group B (solid circles), group C (open triangles) and group D (solid triangles).

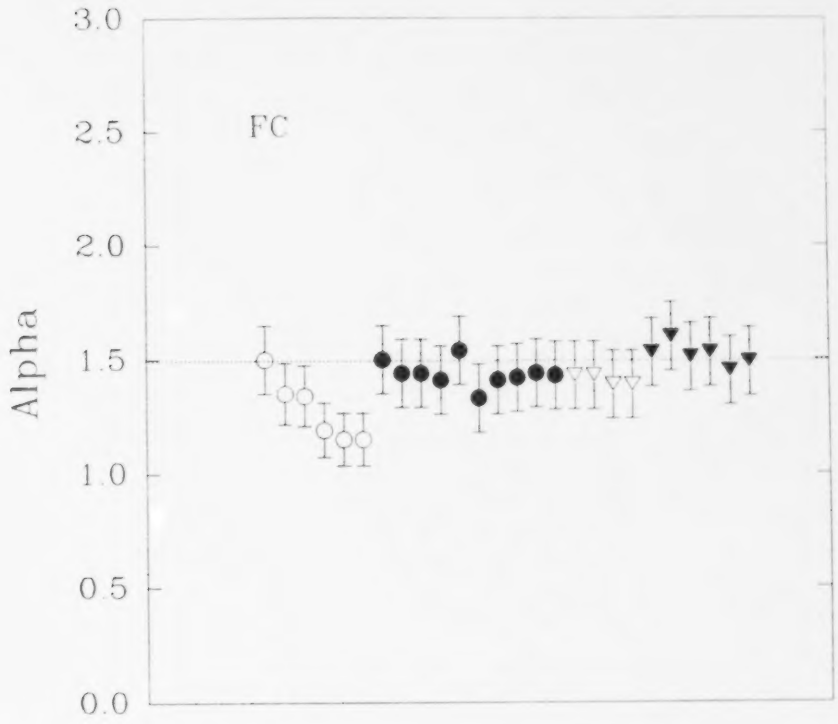

Fig. 67. The values of α acquired by all samples for different fields up to 60 G. Group A (open circles), group B (solid circles), group C (open triangles) and group D (solid triangles).

In weak applied magnetic fields the behavior of the critical current close to T_c^* in all samples exihibits a unique value of α=3/2, characteristic of the Ginzburg-Landau strong coupling regime. This phenomena does not depend on the specific mechanism which limits the critical current. As indicated in Table 10, all samples fall into two categories regarding the current relaxation process. In samples that did not show a current relaxation (decay), the critical current is limited by pair-breaking mechanism (depairing current). If decays are noticeable, depinning of flux lines is responsible for limiting the critical current (depinning current). The results show that both mechanisms, depinning and depairing, can exist in any junction configuration, SIS or SNS. A striking feature is that magnetic field does not distinguish between depinning and depairing currents in the sense that it converts any temperature dependence, $I_c(T)$, to that of Ginzburg-Landau close to transition temperature T_c^*. It should also be noticed that the effect of the applied field on the value of α is switched on at a certain crossover temperature which decreases with increasing the applied magnetic field. According to Clem's model discussed in Chapter 1, this temperature is the one at which Josephson coupling energy between the superconducting grains becomes equal to the condensation energy of the grains themselves, i.e. when the grain size is comparable to the Ginzburg-Landau (GL) coherence length. Applied magnetic field most likely introduces more granularity

in ceramic samples (through pair breaking interactions) and reduces the effective size of the superconducting grains (islands). This in turn reduces the crossover temperature at which the GL coherence length matches the effective grain size.

Similar behavior was obtained in experiments by other research groups for both intergrain and intragrain currents. Manhart *et. al.*[52] used YBCO films to measure the intragrain critical current using an I-V technique. Their results show that an external applied magnetic field of 0.5-1.1 T is able to transform the linear behavior of $I_c(T)$ into concave dependence given by the Ginzburg-Landau $(T-T_c)^{3/2}$ regime (Equation 18). Measurements done on YBCO thin films by Jones *et. al.*[53] revealed the transition from linear to concave $(T-T_c)^{3/2}$ behavior upon reduction of the oxygen content. Similar phenomena[54,55] were observed for the intergrain critical current in an external magnetic field. Darhmaoui and Jung[56] studied the influence of the applied magnetic field and oxygen deficiency on the temperature dependence of (a) intragrain critical current in YBCO thin films and (b) intergrain critical current in YBCO ceramics. They suggested that the superconducting grains may consist of small domains (10-40 Å in size) connected by Josephson tunnel junctions. Similarities of $I_c(T)$ for both YBCO ceramics and YBCO thin films imply that the intergrain connections (weak links) in ceramic YBCO have the form of narrow microbridges (a feature proposed earlier

by Larbalestier[57]) whose internal structure is similar to that of the grains themselves, i.e. consisting of superconducting domains separated by SIS junctions. For temperatures at which the size of these domains is less than the coherence length $\xi(T)$, Cooper pairs will not "see" the junctions and the temperature dependence of the intergrain critical current changes from Ambegaokar-Baratoff to Ginzburg-Landau type.

Temperature dependence of the intergrain critical current of zero-field-cooled YBCO/Ag composites in group B of ceramic samples (Figures 29-33) indicates that the intergrain current is controlled by SIS tunnel junctions (expressed by Ambegaokar-Baratoff form of $I_c(T)$) up to 80 K and by SNS proximity junctions above 80 K. This could happen if oxygen depleted superconducting layers (of T_c=80 K) cross the microbridges. Increasing applied magnetic field seems to introduce disorder and transform the intergrain $I_c(T)$ into Ginzburg-Landau form close to T_c. This suggests that in the case of superconducting domains coupled by SNS proximity junctions, the crossover from deGennes-like $(T-T_c)^2$ temperature dependence of I_c to Ginzburg-Landau may also be observed.

Reduction of the size of the microdomains was attributed to either oxygen depletion or penetration of external magnetic fields through Josephson junctions. Both mechanisms can suppress superconductivity through pair-breaking interaction. Pair breaking in conventional superconductors caused by

magnetic impurities or external magnetic field has been analyzed by Maki[58] and Skalski *et al.*[59] and was shown to induce gapless superconductivity. Kresin *et al.*[60] suggested a model in which the superconductivity in CuO chains of YBCO is induced by charge transfer from the planes via the proximity effect. Magnetic impurities such as Cu^{2+} have magnetic moments which act like pair breakers and suppress the induced gap on the chains. Gapless superconductivity can exist in YBCO without a noticeable shift in T_c.

The picture of microbridges connecting the grains of YBCO, where both the microbridges and the grains have the same domain composition is supported by the field dependence of the critical current. At low temperatures and low magnetic fields, the current depends on the field according to Fraunhofer pattern (sinH/H) for Josephson junctions. In an increasing field, $I_c(H)$ becomes Kim's like $(1/H+H_0)$ for a strong coupling regime in which the current does not "see" the Josephson junctions. If the temperature approaches T_c, very weak magnetic fields will be able to induce the $1/(H+H_0)$ behavior and hence the sin(H)/H behavior will disappear completely from the I(H) curves (see Figures 40 and 41).

4.2.2. Dissipation of the persistent current in high-T_c ceramics:

Measurements of the depinning persistent current dissipation were completed for eight samples which showed time decays

(Table 9) in the presence and absence of external magnetic fields (ZFC and FC cases). The time decays of the currents circulating around the rings were found to be logarithmic in time (Fig. 42)

The current dissipation process was described by Tinkham and Lobb[31] who considered a simple granular configuration of a closed current loop of inductance L containing a large number of weak links in series with total normal resistance R_n. In the superconducting state the resistance is reduced to a value R. Ambegaokar and Halperin[61] analyzed the theoretical I-V characteristics of a similar model and pointed out that R varies exponentially with the current I, roughly as exp(hI/4ekT) and takes on the value R_n, the normal state resistance, when $I=I_c$. Tinkham and Lobb[31] approximated this dependence by a simple analytic form

$$\frac{R}{R_n} = e^{-\gamma_0(1-i)} \qquad (60)$$

where

$$\gamma_0 = \frac{U_0}{kT}, \qquad i = \frac{I}{I_c} \qquad (61)$$

I_c is the critical current flowing in the circuit and U_0 is the unperturbed pinning potential. When the induced and resistive voltages are balanced, the decay of the current is governed by the equation

$$-L\frac{dI}{dt}=IR=IR_n e^{-\gamma_0(1-i)} \qquad (62)$$

which integrates to

$$i=\frac{I}{I_c}=1-\frac{1}{\gamma_0}\ln(1+\gamma_0\frac{t}{\tau}) \qquad (63)$$

where $\tau=L/R_n$ is the decay characteristic time constant and at $t=0$ $R=R_n$ and $I=I_c$. For $\gamma_0>1$ and long time decays Equation (63) reduces to

$$\frac{di}{d\ln t}=\frac{-1}{\gamma_0} \qquad (64)$$

or

$$S=\frac{-kT}{U_0} \qquad (65)$$

where $S=1/I_c(dI/d\ln t)$ is the normalized logarithmic decay rate. In ceramic rings $S\approx 1/I_0(dI/d\ln t)$ where I_0 is the maximum initial current flowing in the ring measured after reducing the external field to zero. The temperature and field dependence of S over a range of 64-90 K are plotted in Figures 43-50. At low temperatures S depends weakly on temperature but it exhibits a sudden increase very close to T_c^*. This behavior is observed for both the ZFC and FC cases. Note that in the FC case, T_c^* is suppressed by the field and therefore S(T) increases at lower temperatures.

Equation 65 can be used to calculate $U_0(T)$, the unperturbed potential, if the normalized logarithmic decay rate S is known. The values of S obtained from Figures 43-50 were

applied to calculate $U_0(T)$ in each case. The results are shown in Figures 68-75 for all eight samples characterized by depinning currents.

A major difference between granular (randomly oriented) ceramics and grain-aligned c-axis oriented YBCO is the behavior of $U_0(T)$. While it was found that for the grain-aligned compounds $U_C(T)$ is constant over a temperature range of 78-88 K (Figure 59), ceramics give a completely different picture: $U_0(T)$ decreases monotonically with increasing temperature and approaches zero at temperatures very close to T_c^*. Also $U_0(T)$ resembles $I_c(T)$ for all rings in the ZFC and FC cases. This similarity is a striking feature of granular superconductors and in the following section it will be used to analyse the origin of pinning in these compounds.

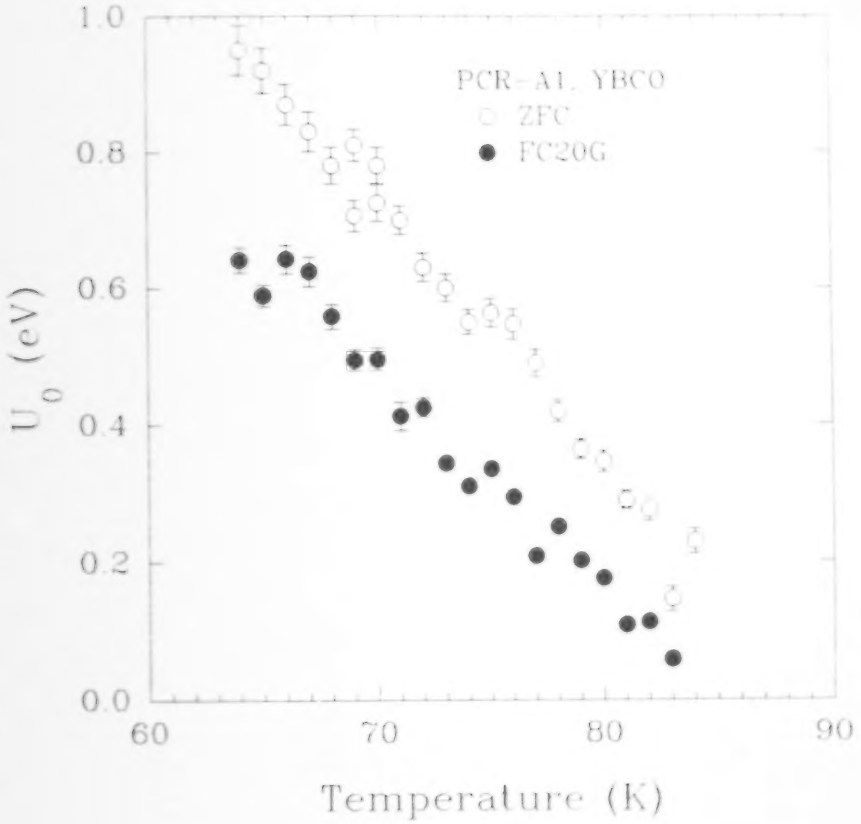

Fig. 68. Dependence of the intergrain flux creep pinning potential U_0 in YBCO ring PCR-A1 on temperature over a range between 64 and 90 K for the ZFC and FC(20G) cases.

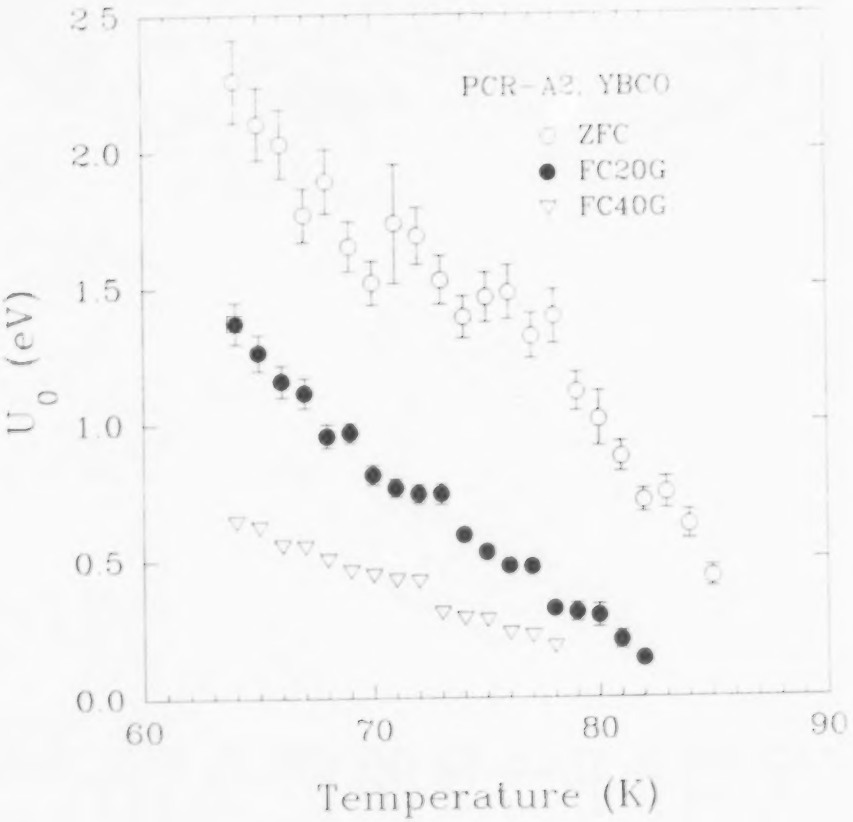

Fig. 69. Dependence of the intergrain flux creep pinning potential U_0 in YBCO ring PCR-A2 on temperature over a range between 64 and 90 K for the ZFC, FC(20G) and FC(40G) cases.

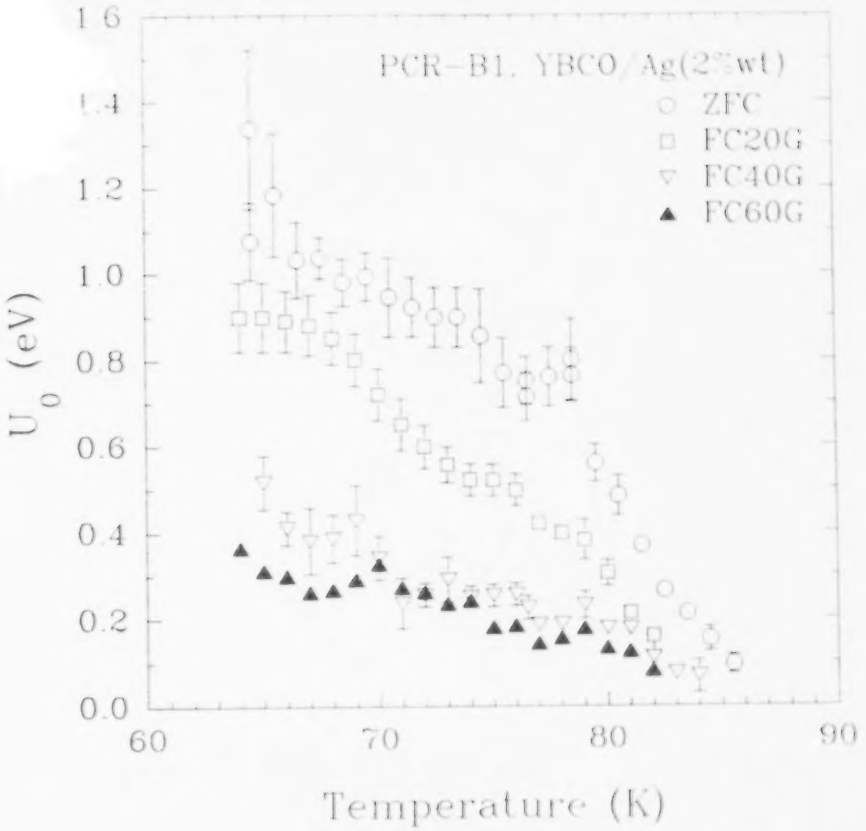

Fig. 70. Dependence of the intergrain flux creep pinning potential U_0 in YBCO/Ag (2%wt) ring PCR-B1 on temperature over a range between 64 and 90 K for the ZFC, FC(20G), FC(40G) and FC(60G) cases.

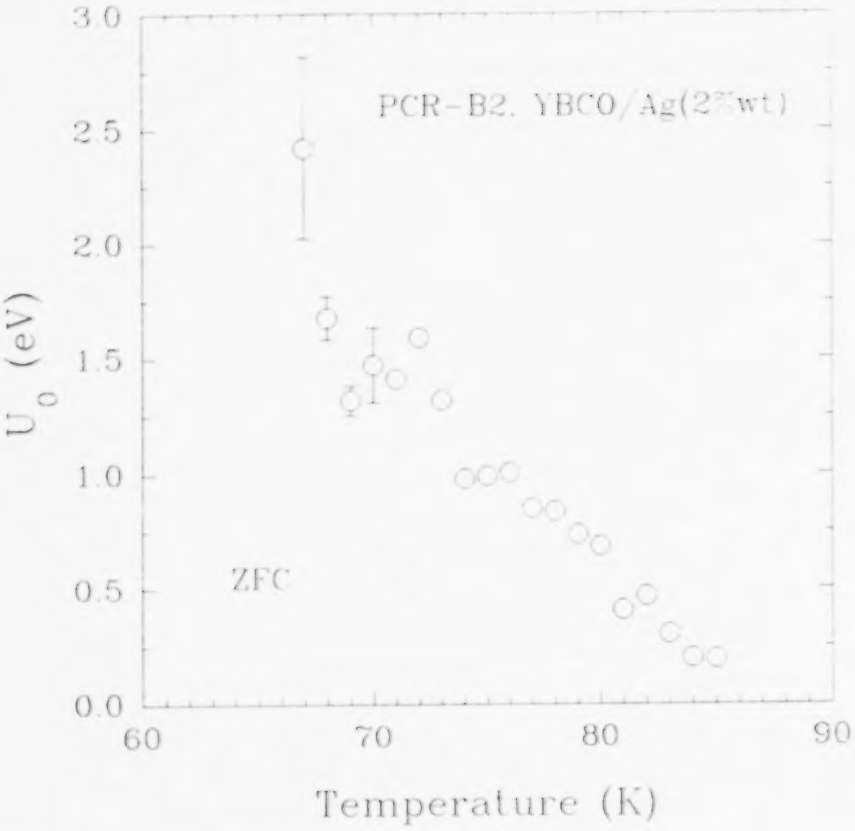

Fig. 71. Dependence of the intergrain flux creep pinning potential U_0 in YBCO/Ag (2%wt) ring PCR-B2 on temperature over a range between 64 and 90 K for the ZFC case.

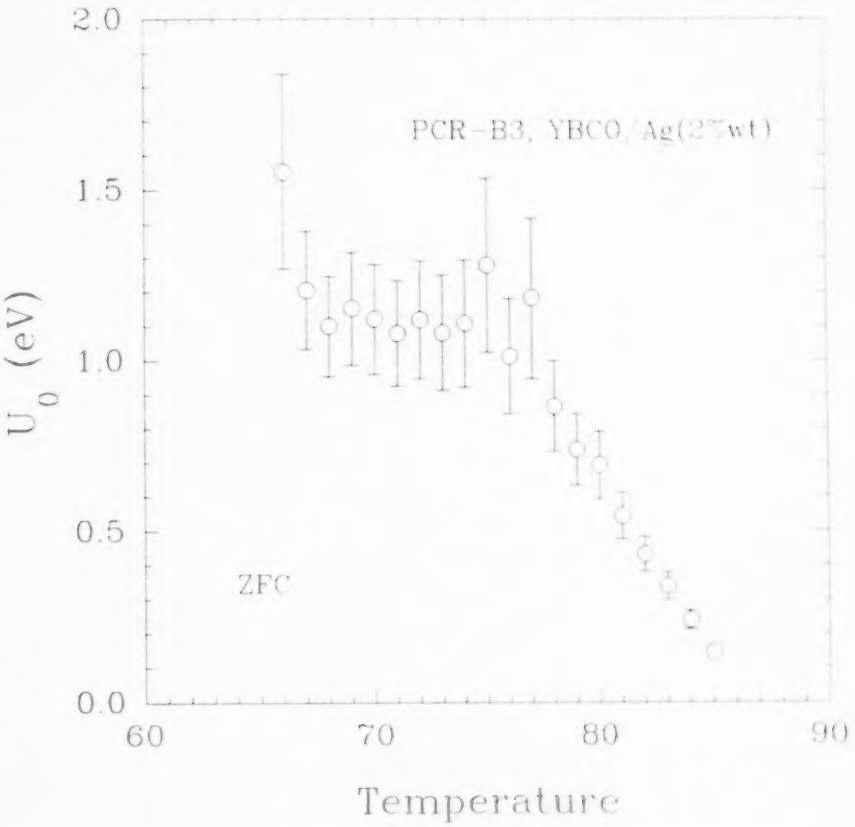

Fig. 72. Dependence of the intergrain flux creep pinning potential U_0 in YBCO/Ag (2%wt) ring PCR-B3 on temperature over a range between 64 and 90 K for the ZFC case.

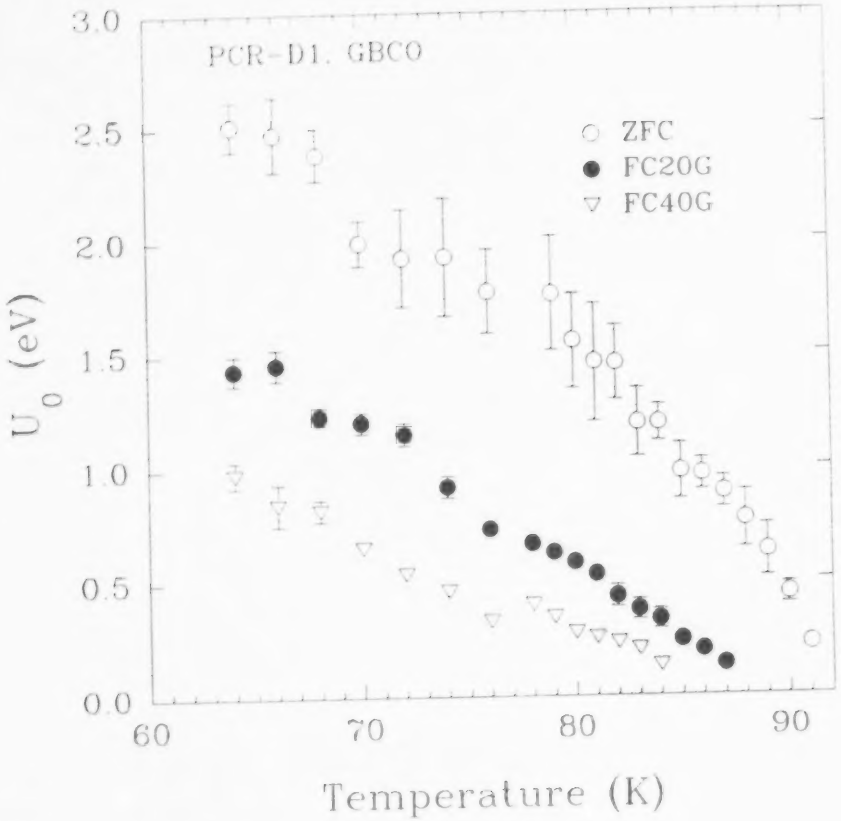

Fig. 73. Dependence of the intergrain flux creep pinning potential U_0 in GBCO ring PCR-D1 on temperature over a range between 64 and 92 K for the ZFC, FC(20G) and FC(40G) cases.

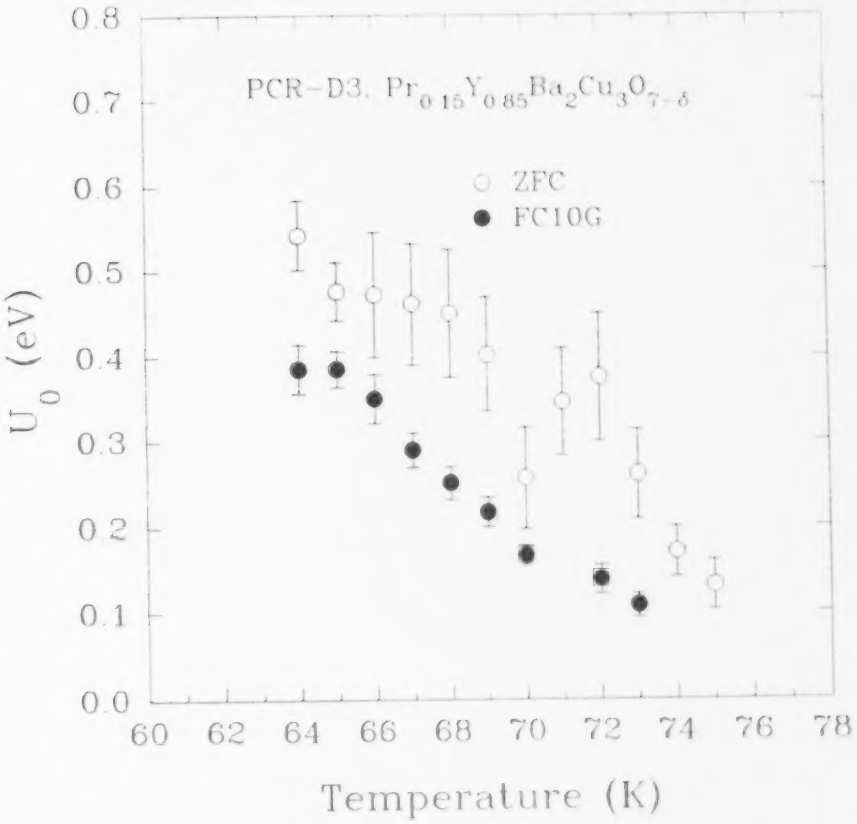

Fig. 74. Dependence of the intergrain flux creep pinning potential U_0 in $Pr_{0.15}Y_{0.85}Ba_2Cu_3O_{7-\delta}$ ring PCR-D3 on temperature over a range between 64 and 77 K for the ZFC and FC(10G) cases.

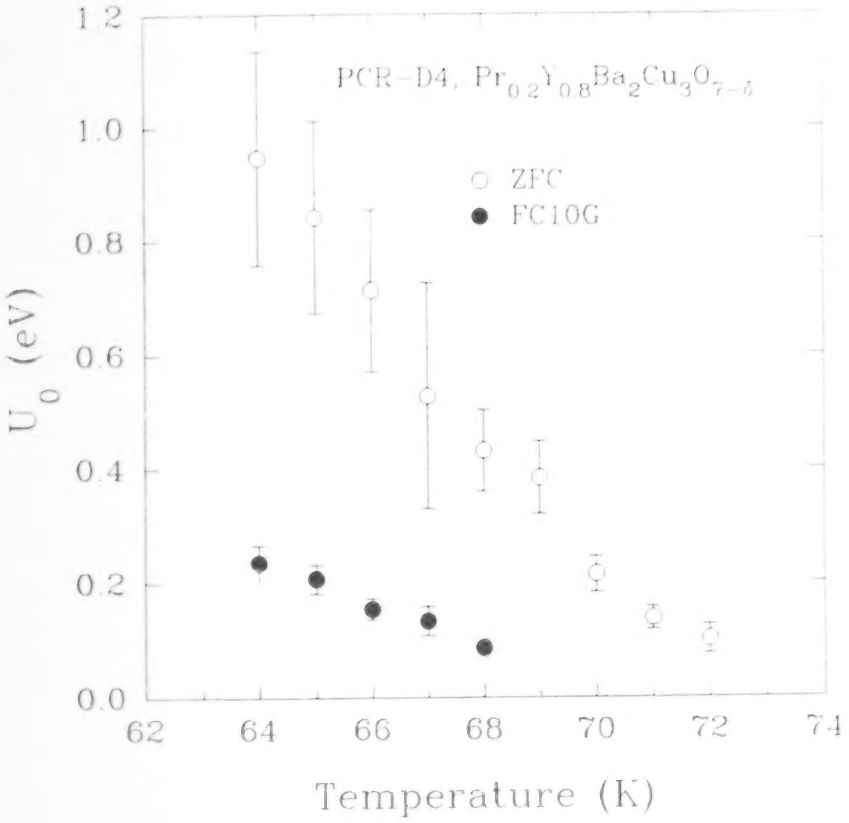

Fig. 75. Dependence of the intergrain flux creep pinning potential U_0 in $Pr_{0.20}Y_{0.80}Ba_2Cu_3O_{7-\delta}$ ring PCR-D4 on temperature over a range between 64 and 72 K for the ZFC and FC(10G) cases.

4.2.3. Origin of pinning in high-T_c ceramics:

Since the behavior of the critical current in granular superconductors is dominated by Josephson tunnel junctions, it is important to consider pinning in the long Josephson junctions (LJJ) in order to understand pinning in more complicated bulk YBCO. In LJJ, external applied magnetic fields are screened exponentially up to the Josephson penetration depth λ_J, which leads to occurrence of a weak Meissner effect. Furthermore, there exists a critical field, H_{c1J}, above which the magnetic field enters the junction in the form of Josephson vortices. These properties show certain similarities between type-II superconductors and LJJ. A key property is the ability of LJJ to carry a non-zero critical current in large magnetic fields. In the case of type-II superconductors, it is well known that the existence of a finite critical current in the mixed state is due to the pinning of the vortices at inhomogeneities of the sample. This prevents the dissipation caused by moving flux lines. One could expect that the disorder-induced pinning should lead to an increase of the critical current crossing the Josephson junction. Pinning of the vortex lattice is also possible at the sharp boundaries of the junction, where the Josephson coupling abruptly drops to zero. Hence, the boundaries can act as a defect, i. e., they can generate a pinning potential. However, since the pinning due to the boundaries is a surface effect, it was shown [62, 63] that such uniform long junctions can not carry a critical

current density. One could then expect that an inhomogeneous coupling along the junction can lead to flux pinning. Fehrenbacher *et al.*[63] suggested that this type of inhomogeneity will create a potential well in the Josephson coupling energy. Mee *et al.*[64] considered the possibility that the potential well arise from the difference between the maxima and minima of the Josephson junction energy E_J. Therefore, the Josephson coupling energy could be written as[63]

$$E_J=\bar{E}_J+V(x) \tag{66}$$

with

$$V(x)=\begin{matrix}0 & x<0\\ -q\bar{E}_J & 0\le x\le r_0\\ 0 & x>r_0\end{matrix} \tag{67}$$

where the average Josephson coupling energy is proportional to I_c, V(x) represents the variation in the coupling energy (Figure 76) and q gives the depth of the well. A normalized pinning potential was introduced in the form[63]

$$U_n=\frac{q\bar{E}_J}{U_0}=\frac{q\hbar I_c}{2eU_0} \tag{68}$$

which is the ratio of the variation in the coupling energy to the pinning potential.

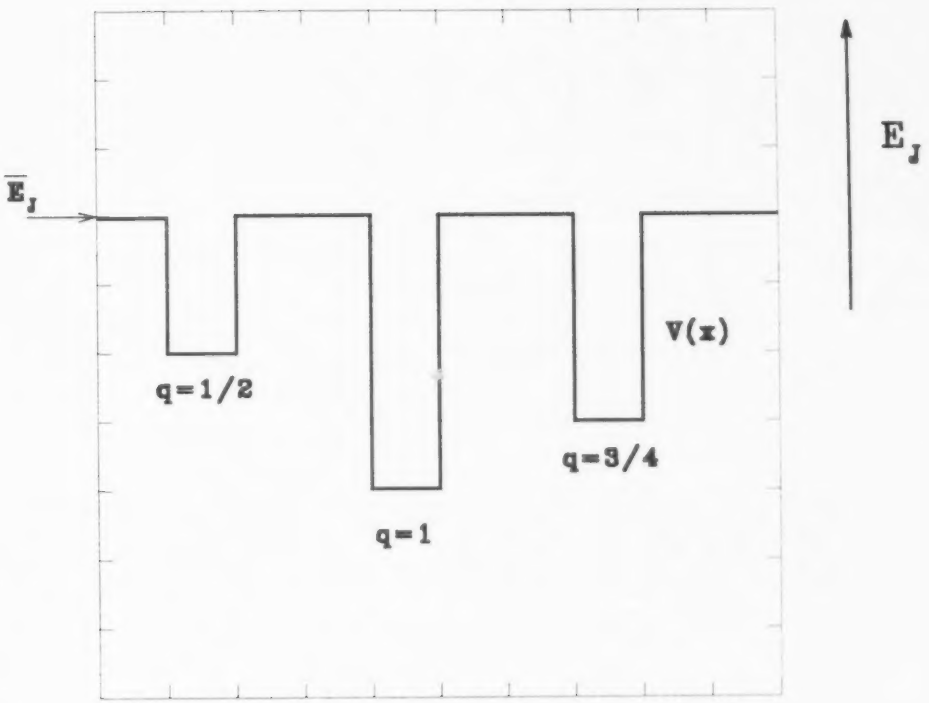

Fig. 76. Potential energy along a one dimensional array of Josephson junctions with different coupling strength.

The quantity U_n was calculated for different samples and is plotted as a function of temperature in the presence and absence of magnetic fields in Figures 77-84. In the ZFC case, the normalized pinning potential exhibits a weak temperature dependence at low temperatures and it decreases close to T_c^*. This dependence supports the picture suggested earlier by Mee *et al*[64] that the origin of pinning might be due to the variation of the coupling strength of adjacent junctions. Close to T_c^* the critical current undergoes a crossover from AB (Ambegaokar-Baratoff) to GL (Ginzburg-Landau) regime at a certain crossover temperature.The definition of Josephson coupling energy is therefore not valid for temperatures higher than the crossover temperature. Magnetic fields reduces the crossover temperature and consequently reduces the range over which the Josephson pinning potential introduced above has physical sense.

The unique behavior of S close to T_c provides an excellent measure of the influence of granularity on the physical properties of high-T_c superconductors and homogeneity of the grain boundaries. Grains which are well aligned and strongly coupled through non-weak links exhibit a behavior similar to that shown in Figure 59, i.e. they are characterized by a temperature independent S. The unperturbed pinning potential, U_0, for this type of compounds is almost temperature independent as well.

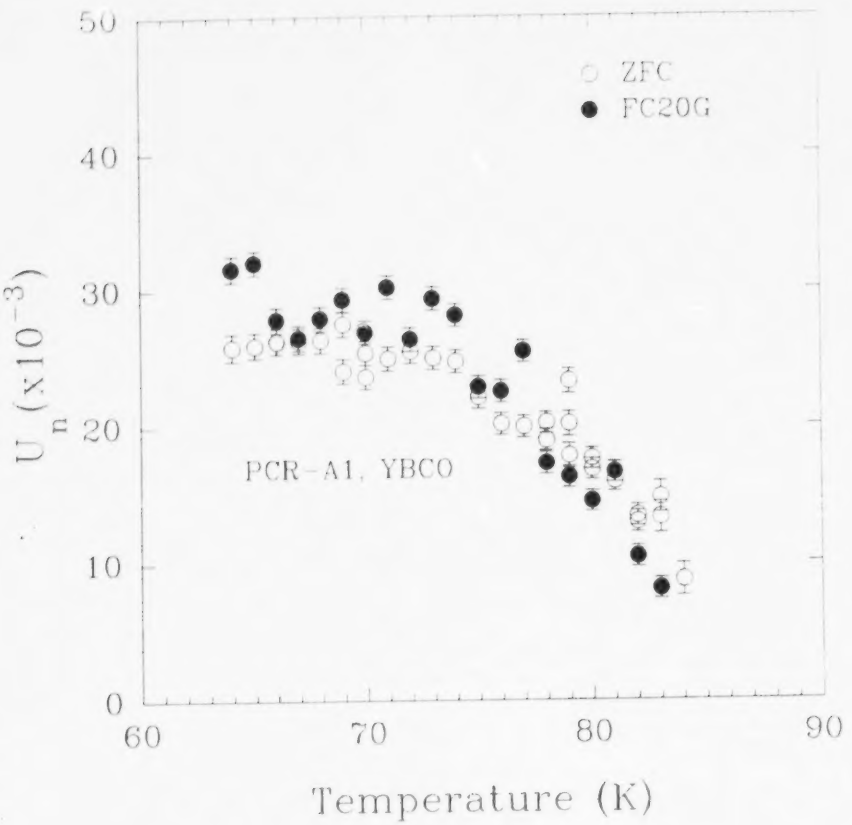

Fig. 77. Dependence of the normalized pinning potential U_n in YBCO ring PCR-A1 on temperature over a range between 64 and 90 K for the ZFC and FC(20G) cases.

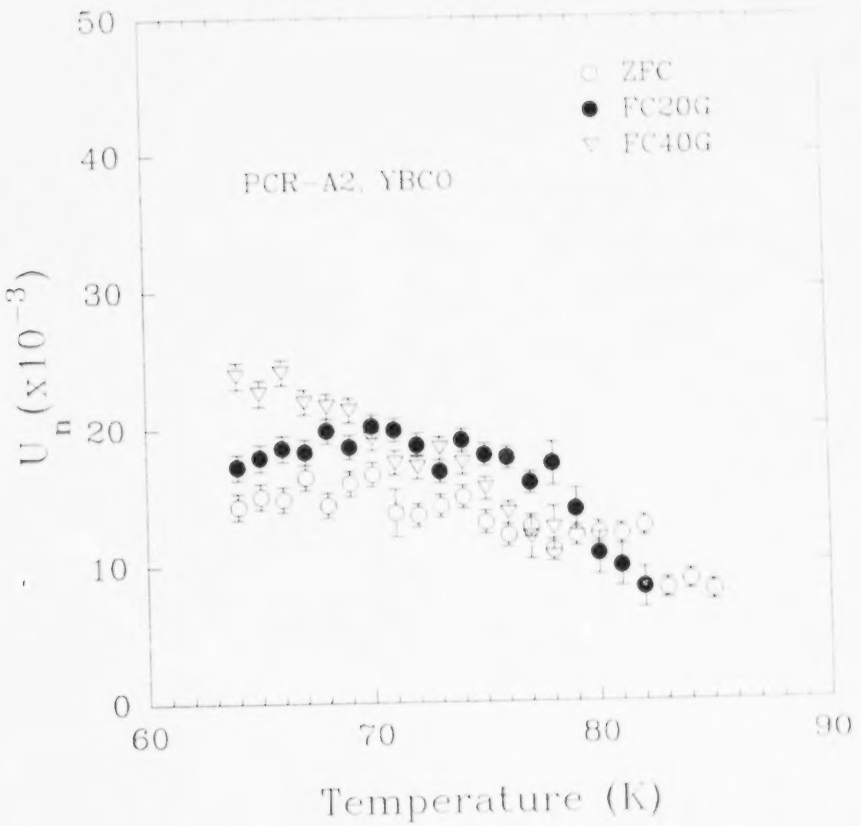

Fig. 78. Dependence of the normalized pinning potential U_n in YBCO ring PCR-A2 on temperature over a range between 64 and 90 K for the ZFC, FC(20G) and FC(40G) cases.

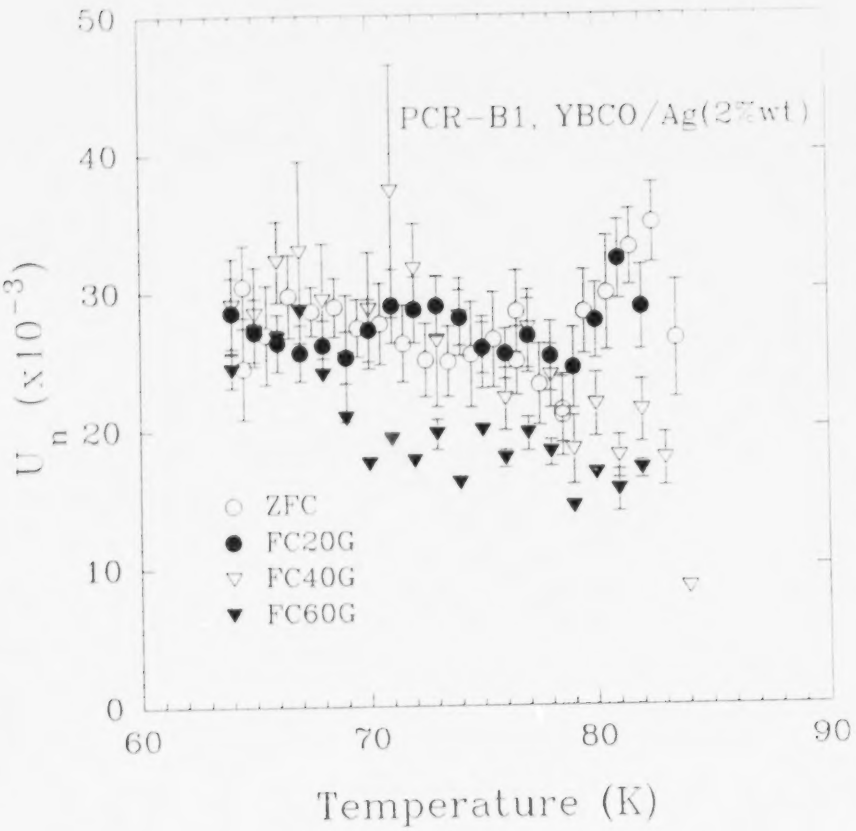

Fig. 79. Dependence of the normalized pinning potential U_n in YBCO/Ag (2%wt) ring PCR-B1 on temperature over a range between 64 and 90 K for the ZFC, FC(20G), FC(40G) and FC(60G) cases.

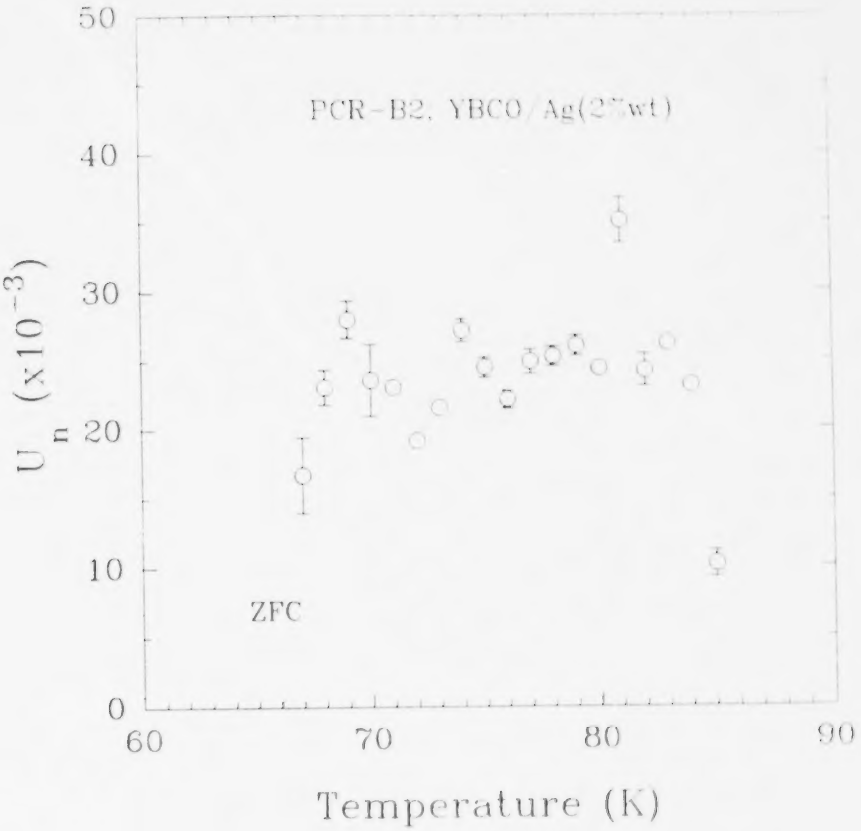

Fig. 80. Dependence of the normalized pinning potential U_n in YBCO/Ag (2%wt) ring PCR-B2 on temperature over a range between 64 and 90 K for the ZFC case.

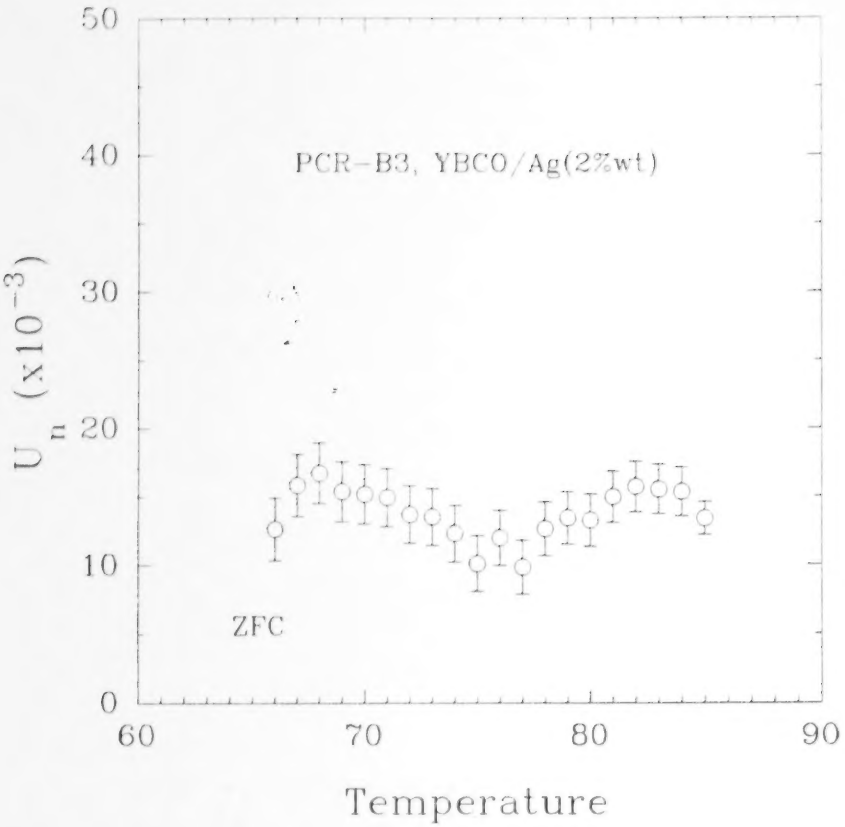

Fig. 81. Dependence of the normalized pinning potential U_n in YBCO/Ag (2%wt) ring PCR-B3 on temperature over a range between 64 and 90 K for the ZFC case.

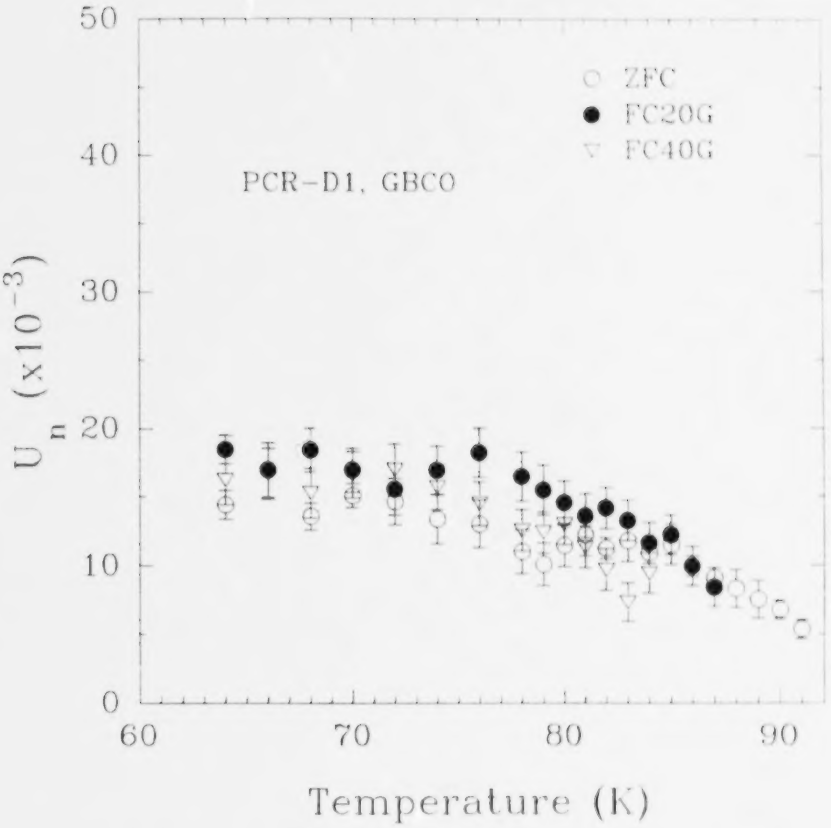

Fig. 82. Dependence of the normalized pinning potential U_n in GBCO ring PCR-D1 on temperature over a range between 64 and 92 K for the ZFC, FC(20G) and FC(40G) cases.

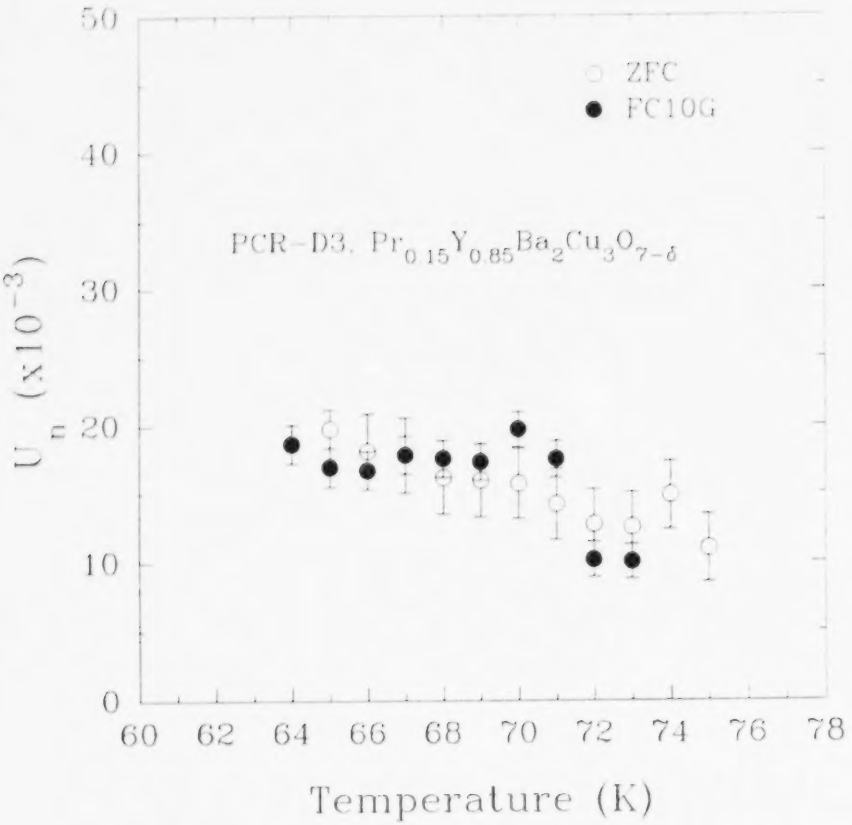

Fig. 83. Dependence of the normalized pinning potential U_n in $Pr_{0.15}Y_{0.85}Ba_2Cu_3O_{7-\delta}$ ring PCR-D3 on temperature over a range between 64 and 77 K for the ZFC and FC(10G) cases.

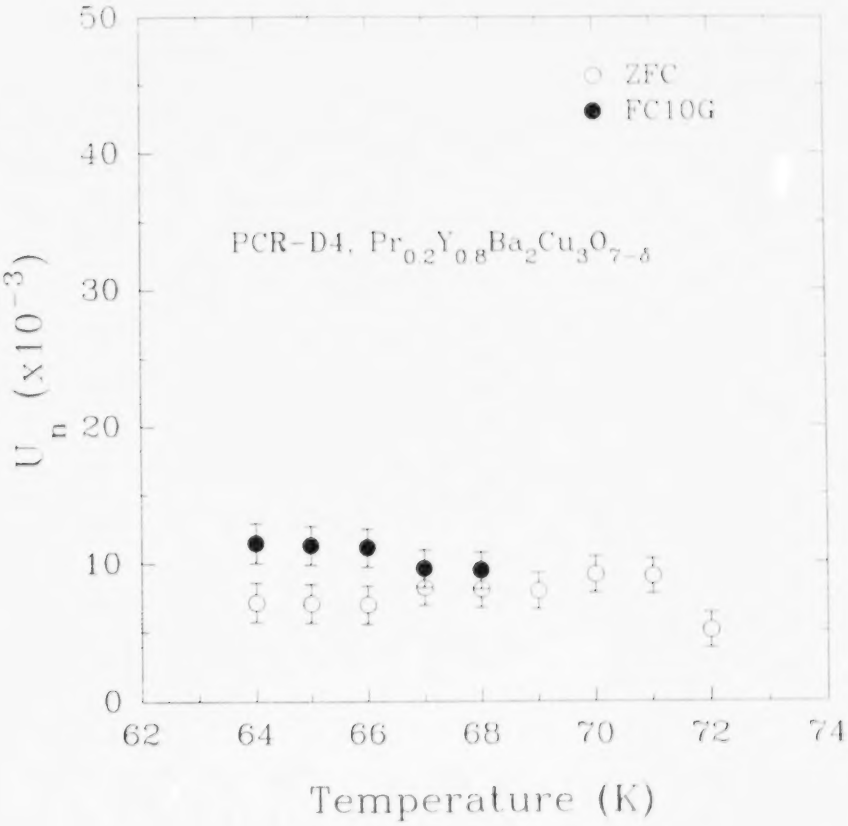

Fig. 84. Dependence of the normalized pinning potential U_n in $Pr_{0.20}Y_{0.80}Ba_2Cu_3O_{7-\delta}$ ring PCR-D4 on temperature over a range between 64 and 72 K for the ZFC and FC(10G) cases.

On the other hand if the grains of the bulk are randomly oriented and the grain boundaries are not homogeneous, S increases close to T_c and U_0 drops to lower values.

It was claimed before that for single crystals and oriented thin films of YBCO, the temperature independent behavior of S is universal[46] leading to a weakly temperature dependent $U_0(T)$ over the whole temperature range up to T_c. An increasing S(T) or decreasing $U_0(T)$ was usually attributed to a limited ability of SQUID magnetometers to measure magnetic moment fast enough for large decays close to T_c^*. However, many other research groups obtained data similar to those presented in Figures 43-50 and 68-75 from measurements performed on different YBCO compounds such as single crystals[21, 65, 66, 67], thin films[68, 69], melt processed grains[70], oriented grains[47] and ceramics[64]. These data are presented in Figure 85. Possibility of unreliable measurements using SQUID magnetometers should be ruled out since in the references quoted above a variety of measuring techniques has been employed, e. g., DC magnetization[21, 64, 65, 67, 70], AC induction[47], Hall probes[66, 68] and I-V characteristics[69]. The results show that close to T_c there is either an increase in S(T) (Figure 85) or equivalently a decrease in $U_0(T)$. Similarities between the temperature dependence of S(T) (and $U_0(T)$) in YBCO ceramics, single crystals and epitaxial thin films suggest that granularity seems unavoidable even in single crystals and thin films.

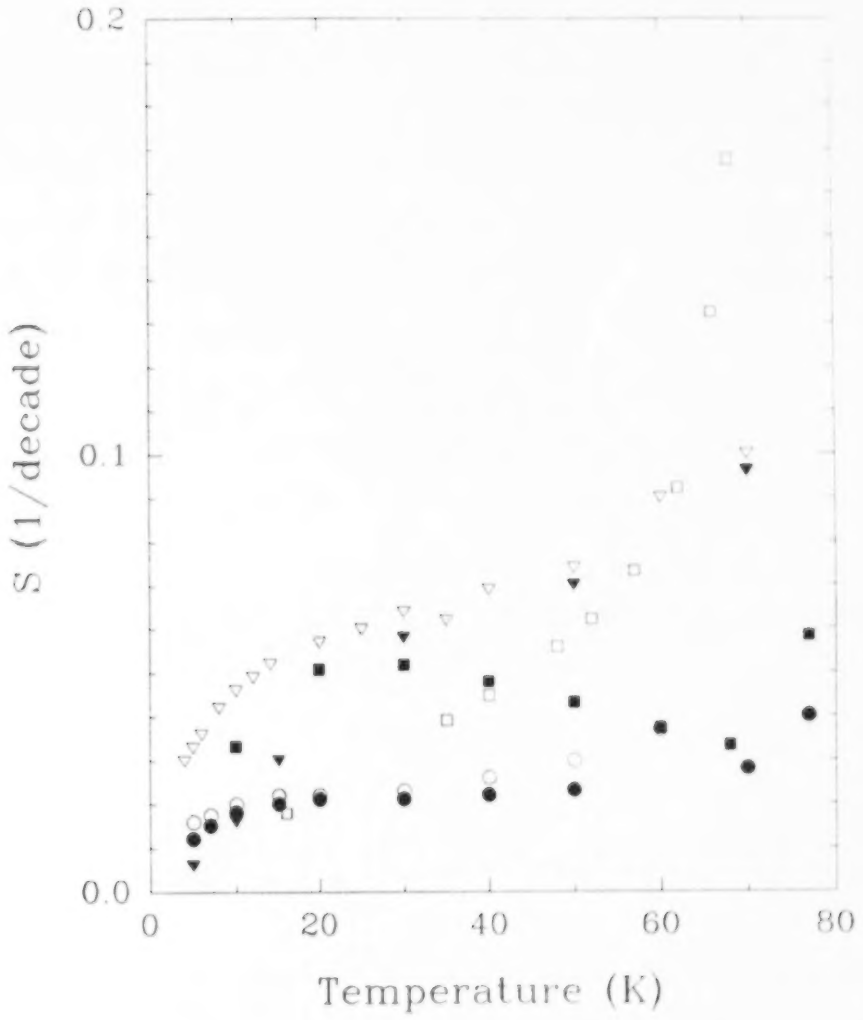

Fig. 85. Dependence of the normalized decay rate S on temperature obtained from the measurements on YBCO compounds. Open circles and solid circles: irradiated YBCO single crystals (Refs. 21 and 65). Open triangles and solid triangles: YBCO single crystal (Refs. 66 and 67). Open squares: YBCO thin films (Ref. 69) and solid squares: YBCO melt-processed samples (Ref. 70).

Chapter V

Conclusions

In order to study the pinning and granularity effects in high-T_c superconductors an important experimental condition must be satisfied: the supercurrent, which is used to probe the pinning potential and the grain boundaries, must be self-sustaining (so it is sensitive to any resistive dissipation), and its properties must be measured using a contactless method. The experimental setup, which was built to fulfill these requirements, uses persistent supercurrents induced in superconduntinq YBCO rings and a Hall probe to detect the magnitude of these currents and their dissipation rates. Measurements were performed on two types of YBCO: (a) c-axis oriented grain aligned YBCO prepared using MPMG method (four rings), and (b) ceramic YBCO, RBCO (where R= Gd, Eu, $Pr_{0.15}Y_{0.85}$, $Pr_{0.2}Y_{0.8}$) and YBCO/Ag prepared using standard solid state reaction method (fourteen rings). We measured: (i) dependence of the persistent current on temperature at various applied magnetic fields, (ii) dependence of the persistent current on magnetic field at various temperatures and (iii) dependence of persistent current on time (dissipation).

Measurements of the Abrikosov flux induced relaxation of the persistent current circulating in rings of c-axis oriented grain aligned YBCO have been performed close to T_c over a temperature range of 79-90 K and a time range of 30-20,000 sec for a wide range of current I_0 between 0 and I_c. The results

revealed two distinct relaxation regimes for the persistent current: (i) a steady state logarithmic decay which is visible over the applied time scale for initial current I_0 close to I_c, and (ii) a slow non-logarithmic, non-steady-state initial decay characteristic of initial current I_0 much smaller than I_c. This initial non-logarithmic decay eventually converges after a time t_p into a steady-state logarithmic decay. It was shown that the Anderson[3] flux creep model describes well the logarithmic decay of the current. The logarithmic relaxation exhibits the following features of the model:

(a) The time and temperature dependence of j according to the formula

$$j(t)=j_c(T)\left(1-\frac{kT}{U_0}\ln\frac{t}{t_{eff}}\right)$$

where $U_0\approx 0.4$ eV and $t_{eff}\approx 10^{-5}$ sec.

(b) The proportionality of the effective energy barrier for flux creep to the current (current density)

$$U_{eff}(j)=U_0\left(1-\frac{j}{j_c(T)}\right)$$

Non-logarithmic initial decays of the currents for $I_0 \ll I_c$ are characterized by (a) the independence of the normalized decay rate $(1/I_0)dI/dt$ on the initial current I_0; (b) the independence of the effective energy U_{eff} on the current I(t) at fixed time and (c) a reduction of the initial decay rate dI/dt with the decreasing magnitude of the initial current I_0.

The initial slow non-logarithmic decay of the persistent

current could be caused by a transient redistribution of the Abrikosov flux in the sample; this process being similar to that suggested by Gurevich and Kupfer[48, 49] for the initial decay of magnetization in grain aligned YBCO. Theoretical analysis of non-linear flux diffusion (Ref. 49) provided an explicit analytical formula for the initial decay of j(t)

$$j(t)=j_0-j_c(T)\frac{kT}{U_0}\ln\left(1-\frac{t}{t_p(j_0)}\right)$$

The dependence of t_p on j_0 was determined by our experiments. It can be written in the form $\ln(t_p+t_{eff})=a-bj_0$ where a and b are constants ($t_p=0$ at $j_0=j_c$).

Taking into account the results for the magnetization relaxation obtained by Maley's group[8, 16, 20] on grain aligned YBCO close to j_c, we postulate that the steady-state long-time logarithmic relaxation close to T_c is governed by a thermally activated uncorrelated hopping of pointlike vortex bundles according to the Anderson model[3]. However, upon reduction of temperature, this mechanism gradually changes into a thermally activated hopping of strongly interacting vortex lines in a random pinning potential as described by vortex-glass[15, 16] and collective-flux-creep[17, 18] models. Very close to T_c at temperatures above 88.5 K, the slow initial non-logarithmic decays prevail even for currents I_0 close to I_c. Such behavior could be possible if another mechanism of creep, e.g. the plastic hopping of the extended defects of flux line lattice such as dislocations became essential[17].

Measurements of the dependence of the critical current on temperature and magnetic field in ceramic YBCO rings provide the following information about the influence of grain boundaries and 2granularity on the critical currents. The dependence of I_c on temperature close to T_c^* confirms that the intergrain junctions in RBCO (where R= Y, Gd, Eu, $Pr_{0.15}Y_{0.85}$, $Pr_{0.2}Y_{0.8}$) behave like SIS-type tunnel junctions with $I_c \propto (1-T/T_c^*)$ and that the grain boundaries in YBCO/Ag composites have characteristics of SNS-type proximity junctions with $I_c \propto (1-T/T_c^*)^2$. When two half-rings of YBCO/Ag are joined, the resulting interfaces have grain boundaries which are dominated by SIS-type junctions.

The critical temperature T_c^* of the intergrain junctions was found to be about 5 K lower than the intragrain T_c and about 4 K lower than the zero resistance T_c determined from four probe I-V measurements. This means that the I-V method generally overestimates I_c and may affect the temperature dependence of I_c close to T_c. The dependence of I_c on applied magnetic field H showed a sinH/H behavior at low magnetic fields. I_c approached a constant value at higher fields which may be an indication of the presence of microbridges of intrinsic material across the grain boundaries.

Studies of the decay (relaxation) of the persistent current flowing in the superconducting rings allowed us to distinguish between two different mechanisms by which supercurrent is destroyed: (a) depinning of magnetic vortices

(depinning current) and (b) depairing of Cooper pairs (depairing current). Both SIS and SNS intergrain junction can transport either depinning of depairing currents. The decay rates obtained for persistent currents in the absence and in the presence of applied magnetic field provided strong evidence for intergrain flux creep controlled transport current. The calculated activation energy for intergrain flux creep is roughly proportional to the initial value of the intergrain critical current I_c except at temperatures very close to T_c^*. It was shown that at temperatures 3-7 K below T_c^*, the normalized decay rates S(T) acquire higher values. This unique behavior provides a good measure of the influence of granularity on the physical properties of high-T_c superconductors and homogeneity of the grain boundaries.

The temperature dependence of the critical current close to T_c^* in the absence and presence of magnetic field in the ceramic rings revealed a crossover from linear (AB) or quadratic (deGennes) form of I_c to GL dependence in agreement with the Clem's model[26] of $I_c(T)$ in strongly coupled granular superconductors. The crossover was observed for depinning and depairing currents upon applying small magnetic fields up to 60 G. According to the Clem's model, the crossover implies the presence of superconducting microdomains coupled by Josephson junctions. The size of these microdomains decreases with increasing the applied magnetic field. Studies of $I_c(T)$ in YBCO thin films and ceramics over a temperature range of 10-95

K (Ref. 56) suggest that the external magnetic field could break up the domains through pair breaking interaction. The temperature dependence of I_c also suggests[56] that the intergrain connections in ceramic YBCO have a form of clean microbridges with microdomain structure, similar to that of the grains. These microbridges can be easily penetrated by external magnetic fields which can induce the AB to GL crossover in $I_c(T)$. For the ZFC case, the low temperature part of $I_c(T)$ in all samples is governed by the Ambegaokar-Baratoff regime, characteristic of SIS tunnel junctions. The SNS normal metallic junctions appear only in YBCO/Ag composites. Therefore this implies that superconducting microdomain in RBCO are coupled by tunnel junctions and not by proximity junctions.

Measurements of the persistent current, its temperature and field dependence and its relaxation revealed many differences and similarities between grain aligned c-axis oriented and ceramic YBCO compounds. These are summarized in Table 15.

	Grain aligned YBCO	Ceramic YBCO
Intergrain junctions	SIS	SIS SNS in YBCO/Ag only
Type of the critical current	depinning	depinning or depairing
$I_c(H)$	$1/(H+H_0)$ except far away from T_c at low fields where the dependence is $\sin(H)/H$	$\sin(H)/H$ at low fields and $1/(H+H_0)$ at high fields
Vortices involved in dissipation	probably Abrikosov	Josephson
Steady state decay	logarithmic	logarithmic
Duration of the non-steady-state decay	up to 1000 sec	up to 10 sec
$S(T)$ close to T_c	constant	diverges
$U_0(T)$ close to T_c	almost temperature independent	decreases to zero
Origin of pinning	unknown	spatial variation of the Josephson coupling energy

Table 15. Comparison between grain aligned and ceramic YBCO.

Bibliography

1. P. G. deGennes, Superconductivity of Metals and Alloys, (W. A. Benjamin Inc. New York, 1966).

2. C. P. Bean and J. D. Livingston, Phys. Rev. Lett. **12**, 14 (1964).

3. P. W. Anderson, Phys. Rev. Lett. **9**, 309 (1962), P. W. Anderson and Y. B. Kim, Rev. Mod. Phys. **36**, 39 (1964).

4. C. J. van der Beek, G. J. Nieuwenhuys, P. H. Kes, H. G. Schnack, and R. Griessen, Physica C **197**, 320 (1992).

5. M. R. Beasley, R. Labusch, and W. W. Webb, Phys. Rev. **181**, 682 (1969).

6. E. Zeldov, N. M. Amer, G. Koren, A. Gupta, M. W. McElfresh, and R. J. Gambino, Appl. Phys. Lett. **56**, 680 (1990).

7. J. R. Thompson, Y. R. Sun, and F. Holtzberg, Phys. Rev. B **44**, 458 (1991).

8. M. P. Maley, J. O. Willis, H. Lessure, and M. E. McHenry, Phys. Rev. B, **42**, 2639 (1990).

9. Y. Xu, M. Suenaga, A. R. Moodenbaugh, and D. O. Welch, Phys. Rev. B, **40**, 10882 (1989).

10. D. O. Welch, IEEE Trans. Mag. **27**, 1133 (1991).

11. R. Griessen, Physica C **172**, 441 (1991).

12. L. Niel and J. E. Evetts, Europhys. Lett. **15**, 453 (1991).

13. L Neil and J. Evetts, Supercond. Tech. **5**, S347 (1992).

14. C. W. Hagen and R. Griessen, Phys. Rev. Lett. **62**, 2857 (1989).

15. M. P. A. Fisher, Phys. Rev. Lett. **62**, 1415 (1989).

16. D. S. Fisher, M. P. A. Fisher and D. A. Huse, Phys. Rev. B **43**, 130 (1991).

17. M. V. Feigelman, V. B. Geshkenbein, A. I. Larkin, and V. M. Vinokur, Phys. Rev. Lett. **63**, 2303 (1989); M. V. Feigelman, V. B. Geshkenbein, and V. M. Vinokur, Phys. Rev. B, **43**, 6263 (1991).

18. A. I. Larkin, Sov. Phys. JETP **31**, 784 (1970).

19. P. J. Kung, M. P. Maley, M. E. McHenry, J. O. Willis, J. Y. Coulter, M. Murakami, and S. Tanaka, Phys. Rev. B **46**, 6427 (1992).

20. P. J. Kung, M. P. Maley, M. E. McHenry, J. O. Willis, M. Murakami, and S. Tanaka, Phys. Rev. B **48**, 13922 (1993).

21. J. R. Thompson, Y. R. Sun, L. Civale, A. P. Malozemoff, M. W. McElfresh, A. D. Marwick, and F. Holtzberg, Phys. Rev. B **47**, 14 440 (1993).

22. C. P. Bean, Phys. Rev. Lett. **8**, 250 (1962); Rev. Mod. Phys. **36**, 31 (1964).

23. H. G. Schnack, R. Griessen, J. G. Lensink, C. J. van der Beek, and P. H. Kes, Physica C **197**, 337 (1992).

24. S. Martin, A. T. Fiory, R. M. Fleming, G. P. Espinosa, and A. S. Cooper, Phys. Rev. Lett. **62**, 677 (1989).

25. J. Bardeen, L. N. Cooper and J. R. Schriffer, Phys. Rev. **108**, 1175 (1957).

26. J. R. Clem, B. Bumble, S. I. Raider, W. J. Gallagher and Y. C. Shih, Phys. Rev B **35**, 6637 (1987).

27. R. T. Kampwirth and K. E. Gray, IEEE Trans. Magn. MAG **17**, 565 (1981).

28. M. Tikham, Introduction to Superconductivity (McGraw Hill, NY, 1975), p.104.

29. V. Ambegaokar and A. Baratoff, Phys. Rev. Lett. **10**, 486 (1963); and **11** 104(E) (1963).

30. M. Tikham, Introduction to Superconductivity, (McGraw Hill, NY; 1975) p.117.

31. M. Tinkham and C. J. Lobb, Solid State Physics **42**, 91(1989).

32. M. Tinkham, David W. Abraham and C. J. Lobb, Phys. Rev. B **28**, 6578 (1983).

33. C. J. Lobb, David W. Abraham and M. Tinkham, Phys. Rev. B **27**, 150 (1983).

34. B. D. Josephson, Phys. Lett. **1**, 251 (1962).

35. P. G. deGennes, Rev. Mod. Phys. **36**, 225 (1964).

36. J. F. Kwak, E. L. Venturini, P. J. Nigrey and D. S. Ginley, Phys. Rev. B **37**, 9749 (1988).

37. H. Dersch and G. Blatter, Phys. Rev. B **38**, 11 391, (1988).

38. J. W. Ekin, H. R. Hart, and A. R. Gaddipati, J. Appl. Phys. **68**, 2285 (1990).

39. M. Murakami, M. Morita, and N. Koyama, Jpn. J. Appl. Phys. **28**, L1125 (1989).

40. M. Murakami, Mod. Phys. Lett. **4**, 163 (1990).

41. M. Turchinskaya, D. L. Kaiser, F. W. Gayle, A. J. Shapiro, A. Roytburd, L. A. Dorosinskii, V. I. Nikitenko, A. A. Polyanskii and V. K. Vlasko-Vlason. Physica C, **221**, pp62-70 (1994).

42. M. E. McHenry, S. Simizu, H. Lessure, M. P. Maley, J. Y. Coulter, I. Tanaka and H. Kojima, Phys. Rev. B **44**, 7614 (1991).

43. Y. B. Kim, C. F. Hempstead, and A. R. Strand, Phys. Rev. **131**, 2486 (1963).

44. W. R. Smythe, Static and Dynamic Electricity (McGraw-Hill, New York, 1939).

45. V. B. Geshkenbein and A. I. Larkin, Sov. Phys. **JETP 68**, 639 (1989).

46. A. P. Malozemoff and M. P. Fisher, Phys. Rev. B **42**, 6784 (1990).

47. C. Keller, H. Kupfer, R. Meier-Hirmer, U. Weich, V. Selvamanickam, and K. Salama, Cryogenics **30**, 410 (1990).

48. A. Gurevich, H. Kupfer, B. Runtsch, R. Meier-Hirmer, D. Lee, and K. Salama, Phys. Rev. B **44**, 12 090 (1991).

49. A. Gurevich and H. Kupfer, Phys. Rev. B **48**, 6477 (1993).

50. J. R. Thompson, Y. R. Sun, A. P. Malozemoff, D. K. Christen, H. R. Kerchner, J. G. Ossandon, A. D. Marwick and F. Holtsberg, Appl. Phys. Lett. **59**, 2612 (1991).

51. S. E. Babcock (unpublished).

52. J. Mannhart, P. Chaudhari, D. Dimos, C. C. Tsuei and T. R. McGuire, Phys. Rev. Lett. **61**, 2476 (1988).

53. E. C. Jones, D. K. Christen, J. R. Thompson, R. Feenstra, S. Zhu, D. H. Lowndes, J. M. Phillips, M. P. Seigal and J. D. Budai, Phys. Rev. B **47**, 8986 (1993).

54. L. Antognazza, S. J. berkowitz, T. H. Geballe and K. Char, Phys. Rev. B **51**, 8560 (1995).

55. X. Yu and M. Sayer, Phys. Rev. B **44**, 2348 (1991).

56. H. Darhmaoui and J. Jung. (to be published in Phys. Rev. B, June 1, 1996).

57. D. C. Larbalestier, S. E. Babcock, X. Cai, L. Cooley, M. Daeumling and D. H. Hampshire in Progress in High Temperature Superconductivity, Vol. 18; Ed. S. Nakajima (World Scientific, New Jersey, 1989), p 128.

58. K. Maki in Superconductivity; Ed. R. Parks (Marcel Dekker, New York, 1969), p. 1035.

59. S. Skalski, O. Betbeder-Matibet and P. R. Weiss, Phys. Rev. **136**, A 1500 (1964).

60. V. Z. Kresin and S. A. Wolf, Phys. Rev. B **51**, 1229 (1995).

61. V. Ambegaokar and B. Halperin, Phys. Rev. Lett. **22**, 1364 (1969).

62. C. S. Owen and D. J. Scalapino, Phys. Rev. **164**, 538 (1967).

63. R. Fehrenbacher, V. B. Geshkenbein and G. Blatter, Phys. Rev. B **45**, 5450 (1992).

64. C. Mee, A. I. M. Rae, W. F. Vinen, and C. E. Gough, Phys. Rev. B **43**, 2946 (1991).

65. L. Civale, A. D. Marwick, M. W. McElfresh, T. K. Worthington, A. P. Malozemoff, F. H. Holtzberg, J. R. Thompson and M. A. Kirk, Phys. Rev. Lett. **65**, 1164 (1990).

66. D. A. Brawner, N. P. Ong and Z. Z. Wang, Phys. Rev. B **47**, 1156 (1993).

67. C. W. Hagen and R. Griessen, Phys. Rev. Lett. **62**, 2857 (1989).

68. S. W. Goodyear, J. S. Satchell, R. G. Humphreys, N. G. Chew and J. A. Edwards, Physica C, **192**, 85-94 (1992).

69. K. Enpuku, T. Kisu, R. Sako, K. Yoshida, M. Takeo and K. Yamafuji, Japanese Journal of Applied Physics, **28**, L991 (1989).

70. T. Matsushita, Physica C **217**, 461 (1993).

Appendix A

In the absence of any flux gradient, bundles of vortices will be thermally activated to jump over the pinning energy barriers of height U_0. The jump rate is given by

$$R=\omega_0 \exp\left(-\frac{U_0}{kT}\right) \tag{72}$$

where ω_0 is a characteristic frequency of flux line vibrations. If a flux gradient or a current is introduced, the spatial energy dependence will be tilted making the jumps easier in the direction of decreasing the flux density (See Figure 86). The shift in the barrier height is equal to the work done by the driving force in going over the barrier. If α is the force density due to the flux gradient (or the current) which is defined as

$$\alpha = \frac{\partial}{\partial x}\frac{B^2}{8\pi} \tag{73}$$

and L is the characteristic length that determine the size of the bundle, the force on the flux bundle is αL^3 and the work done in moving it a distance L is $\Delta U = \alpha L^4$. If only the forward jumps are considered, the net jump velocity will be given by

$$v=v_0 \exp\left(-\frac{U_0}{kT}\right) \exp\left(\frac{\Delta U}{kT}\right) \tag{74}$$

substituting for $\Delta U = \alpha L^4$ we get

$$v=v_0 \exp\left(-\frac{U_0}{kT}\right) \exp\left(\frac{\alpha L^4}{kT}\right) \tag{75}$$

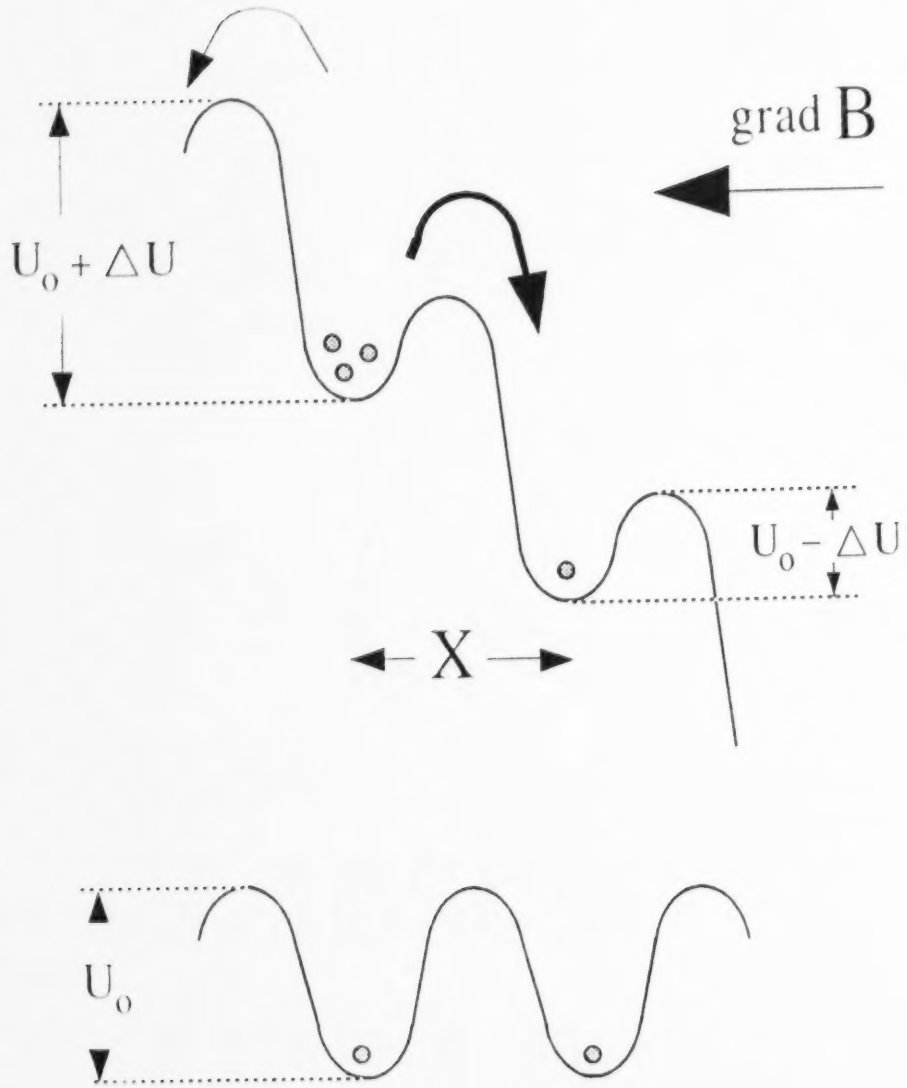

Fig. 86. A schematic model of the pinning potential in the presence (upper) and absence (lower) of field gradient (or current). Flux jumps with jump width X occur in direction of -gradB, where the equilibrium barrier U_0 is lowered by ΔU.

To eliminate L one can define the critical force density at T=0 as

$$\alpha_c(0) = \frac{U_0(0)}{L^4} \tag{76}$$

and hence the velocity could be written as

$$v = V_0 e^{\frac{\alpha}{\alpha_1}} \tag{77}$$

where

$$V_0 = v_0 e^{-\frac{U_0}{kT}} \tag{78}$$

and

$$\alpha_1 = \frac{kT\alpha_c(0)}{U_0(0)} \approx \frac{kT\alpha_c(T)}{U_0(T)} \tag{79}$$

If α (Equation 73) is differentiated with respect to time and using the condition for the conservation of flux lines

$$\frac{\partial B}{\partial t} = -\frac{\partial}{\partial x} Bv \tag{80}$$

we get a differential equation for α in the form

$$\frac{\partial \alpha}{\partial t} = \frac{-B^2}{4\pi} \frac{\partial^2 v}{\partial x^2} + \frac{3B_0}{4\pi d} B \frac{\partial v}{\partial x} - \frac{v}{4\pi} \frac{B_0^2}{d^2} \tag{81}$$

In obtaining this equation we have used the condition $dB/dx = B_0/d$ where B_0 is the magnetic induction at the edge of the bulk of the sample and d is the sample width. However from the definition of α (Equation 73) one can find B in terms of α in the form

$$B=-\frac{4\pi d}{B_0}\alpha \qquad (82)$$

Substituting this into the differential equation (Equation 81) we get

$$\frac{\partial\alpha}{\partial t}=-\left(\frac{4\pi d}{B_0}\right)^2\alpha^2\frac{\partial^2 v}{\partial x^2}-3\alpha\frac{\partial v}{\partial x}-\frac{v}{4\pi}\frac{B_0^2}{d^2} \qquad (83)$$

If v is expressed in terms of α and α_1 (from Eq. 77), Equation (83) becomes

$$\frac{\partial\alpha}{\partial t}=\frac{V_0B_0^2}{d^2}e^{\frac{\alpha}{\alpha_1}}\left(\frac{\alpha}{\alpha_1}\right)^2-\frac{3V_0B_0^2}{4\pi d^2}e^{\frac{\alpha}{\alpha_1}}\left(\frac{\alpha}{\alpha_1}\right)-\frac{V_0B_0^2}{4\pi d^2}e^{\frac{\alpha}{\alpha_1}} \qquad (84)$$

To solve this partial differential equation, one can substitute $z=\alpha/\alpha_1$ and try the solution

$$z=\ln\frac{g(t)}{C} \qquad (85)$$

in order to obtain an expression for g(t) subjected to the boundary condition $g(0)=\infty$. This solution takes the form

$$g(t)=Ce^{\frac{\alpha}{\alpha_1}}=\frac{4\pi\alpha_1 d^2C}{V_0B_0^2t} \qquad (86)$$

which could be rearranged to obtain α as follows

$$\alpha=K-\alpha_1\ln(t), \quad K=\ln\frac{4\pi\alpha_1 d^2}{V_0B_0^2} \qquad (87)$$

Since in relaxation measurements it is always assumed that the decay starts at some effective time, t_{eff} at which $j=j_c$ and $\alpha=\alpha_c$, the constant K could be written as

$$K=\alpha_c+\alpha_1 \ln(t_{eff}) \tag{88}$$

and Equation 87 transforms to

$$\frac{\alpha}{\alpha_c}=1-\frac{\alpha_1}{\alpha_c}\ln\left(\frac{t}{t_{eff}}\right) \tag{89}$$

Substituting for α_1 and α_c in the right hand side of Equation 89, one gets

$$\frac{\alpha}{\alpha_c}=1-\frac{kT}{U_0}\ln\left(\frac{t}{t_{eff}}\right) \tag{90}$$

To avoid the diverging behavior of the logarithmic function at t=o, its argument is increased by one such that

$$\frac{\alpha}{\alpha_c}=1-\frac{kT}{U_0}\ln\left(1+\frac{t}{t_{eff}}\right) \tag{91}$$

Appendix B

The components of the experimental apparatus used in our measurements are illustrated schematically in Figure 87. The numbers used in the figure denote different components and instruments according to the following legend:

1- Liquid nitrogen glass dewar.

2- Liquid nitrogen bath.

3- Solenoid.

4- Hall probe.

5- Sample holder, heater and thermometer.

6- Sample.

7- Gaussmeter.

8- Power supply and potentiometer (driving mechanism).

9- Scanning mechanism.

10- Temperature controller.

11- Constant current power supply.

12- Computer.

13- Liquid nitrogen inlet.

14- Helium gas feed.

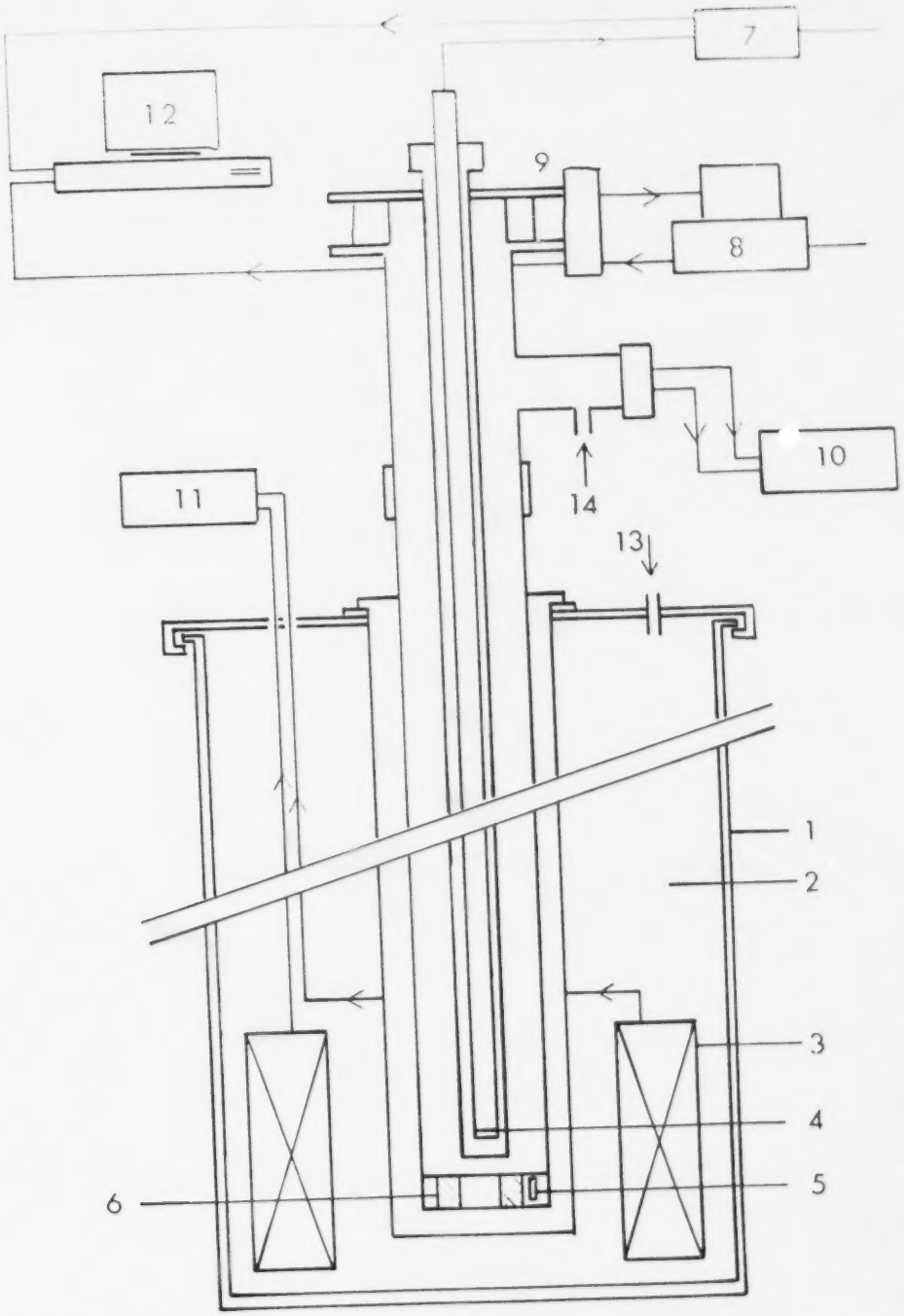

Fig. 87. Schematic representation of the different components of the experimental set-up.